DISSERTATIONES
CHIMICAE
UNIVERSITATIS
TARTUENSIS
187

SAJID HUSSAIN

Electrochemical reduction of oxygen on supported Pt catalysts

DISSERTATIONES CHIMICAE UNIVERSITATIS TARTUENSIS
187

DISSERTATIONES CHIMICAE UNIVERSITATIS TARTUENSIS
187

SAJID HUSSAIN

Electrochemical reduction of oxygen on supported Pt catalysts

UNIVERSITY OF TARTU
Press

Institute of Chemistry, Faculty of Science and Technology, University of Tartu, Estonia

Dissertation is accepted for commencement of the degree of Doctor of Philosophy in Chemistry on June 20, 2019 by the Council of Institute of Chemistry, University of Tartu.

Supervisors: Assoc. Prof. Kaido Tammeveski
Institute of Chemistry, University of Tartu, Estonia

Dr. Nadezda Kongi
Institute of Chemistry, University of Tartu, Estonia

Dr. Heiki Erikson
Institute of Chemistry, University of Tartu, Estonia

Opponent: Assistant Professor, Annukka Santasalo-Aarnio
Department of Chemical and Metallurgical Engineering,
Aalto University, Finland

Commencement: August 27, 2019 at 13:15 in Tartu, Ravila 14a, room 1021

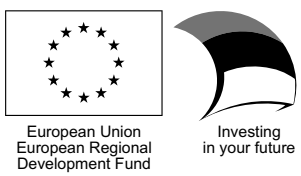

ISSN 1406-0299
ISBN 978-9949-03-108-5 (print)
ISBN 978-9949-03-109-2 (pdf)

University of Tartu Press
www.tyk.ee

To all those who made me the person that I am today.

TABLE OF CONTENTS

1. LIST OF ORIGINAL PUBLICATIONS

This dissertation is based on the following original publications, which will be referred to by the corresponding Roman numerals (I–VII) in the text.

I. **S. Hussain**, H. Erikson, N. Kongi, M. Merisalu, M. Rähn, V. Sammelselg, G. Maia, K. Tammeveski, Platinum particles electrochemically deposited on multi-walled carbon nanotubes for oxygen reduction reaction, *Journal of The Electrochemical Society* 164 (2017) F1014–F1021.

II. **S. Hussain**, N. Kongi, L. Matisen, J. Kozlova, V. Sammelselg, K. Tammeveski, Platinum nanoparticles supported on nitrobenzene-functionalised graphene nanosheets as electrocatalysts for oxygen reduction reaction in alkaline media, *Electrochemistry Communications* 81 (2017) 79–83.

III. **S. Hussain**, H. Erikson, N. Kongi, A. Treshchalov, M. Rähn, M. Kook, M. Merisalu, L. Matisen, V. Sammelselg, K. Tammeveski. Oxygen electroreduction on Pt nanoparticles deposited on reduced graphene oxide and N-doped reduced graphene oxide prepared by plasma-assisted synthesis in aqueous solution, *ChemElectroChem* 5 (19) (2018) 2902–2911.

IV. **S. Hussain**, H. Erikson, N. Kongi, M. Merisalu, P. Ritslaid, V. Sammelselg, K. Tammeveski, Heat-treatment effects on the ORR activity of Pt nanoparticles deposited on multi-walled carbon nanotubes using magnetron sputtering technique, *International Journal of Hydrogen Energy* 42 (9) (2017) 5958–5970.

V. **S. Hussain**, H. Erikson, N. Kongi, A. Tarre, P. Ritslaid, M. Rähn, L. Matisen, M. Merisalu, V. Sammelselg, K. Tammeveski. Pt nanoparticles sputter-deposited on TiO_2/MWCNT composites prepared by atomic layer deposition: Improved electrocatalytic activity towards the oxygen reduction reaction and durability in acid media, *International Journal of Hydrogen Energy* 43 (2018) 4967–4977.

VI. **S. Hussain**, H. Erikson, N. Kongi, A. Tarre, P. Ritslaid, M. Rähn, M. Merisalu, V. Sammelselg, K. Tammeveski. Improved ORR activity and long-term durability of Pt nanoparticles sputter-deposited on TiO_2/MWCNT composite prepared by atomic layer deposition (manuscript submitted).

VII. **S. Hussain**, H. Erikson, N. Kongi, M. Rähn, L. Matisen, M. Merisalu,P. Paiste, J. Aruväli, V. Sammelselg, L.A. Estudillo-Wong, K. Tammeveski, N. Alonso-Vante, Platinum nanoparticles photo-deposited on SnO_2-C composites; an active and durable electrocatalyst for the oxygen reduction reaction, *Electrochimica Acta* 316 (2019) 162–172.

Author's contribution

Paper I: The author has performed synthesis of the electrocatalysts, carried out all electrochemical measurements, analysed the data and is mainly responsible for writing the paper.

Paper II: The author has contributed to the synthesis of the electrocatalysts, electrochemical measurements, data analysis and writing the paper.

Paper III: The author has performed all electrochemical measurements, analysed the data and is mainly responsible for writing the paper.

Paper IV: The author has contributed to the preparation of electrocatalysts, performed all electrochemical measurements, analysed the data and is mainly responsible for writing the paper.

Paper V: The author has contributed to the preparation of electrocatalysts, performed all electrochemical measurements, analysed the data and is mainly responsible for writing the paper.

Paper VI: The author has contributed to the preparation of electrocatalysts, performed all electrochemical measurements, analysed the data and is mainly responsible for writing the paper.

Paper VII: The author has performed synthesis of electrocatalysts, carried out all electrochemical measurements, analysed the data and is mainly responsible for writing the paper.

2. ABBREVIATIONS AND SYMBOLS

AC	activated carbon
ADT	accelerated durability test
ALD	atomic layer deposition
A_r	real electroactive surface area
BE	binding energy
CCR	carbonyl chemical route
CNF	carbon nanofiber
CNT	carbon nanotube
$C_{O_2}^b$	concentration of oxygen in the bulk solution
CV	cyclic voltammetry
CVD	chemical vapour deposition
DFT	density functional theory
D_{O_2}	diffusion coefficient of oxygen
E	potential
E_{onset}	onset potential
$E_{1/2}$	half-wave potential
$E°$	standard potential
ECSA	electrochemically accessible surface area
EDX or EDS	energy dispersive X-ray spectroscopy
F	Faraday constant
GC	glassy carbon
HAADF	high-angle annular dark field
hcd	high current density
HR-SEM	high resolution scanning electron microscopy
HR-TEM	high resolution transmission electron microscopy
ICP-MS	Inductively coupled plasma mass spectrometry
j	measured current density
j_{d}	diffusion-limited current density
j_{lim}	limited current density
j_{k}	kinetic current density
k_{i}	heterogeneous electron transfer rate constant
K-L	Koutecky-Levich
lcd	low current density
MA	mass activity
MWCNT	multi-walled carbon nanotube
n	number of electrons transferred per O_2 molecule
NB	nitrobenzene
NG	nitrogen-doped graphene
ORR	oxygen reduction reaction
PD	photo-deposition
PEMFC	proton exchange membrane fuel cell
Pt/C	carbon-supported platinum catalyst

NP	nanoparticle
R	universal gas constant
RDE	rotating disk electrode
RRDE	rotating ring-disk electrode
rGO	reduced graphene oxide
rGO-N	nitrogen-doped reduced graphene oxide
RHE	reversible hydrogen electrode
SA	specific activity
sccm	standard cubic centimetres per minute
SCE	saturated calomel electrode
SEM	scanning electron microscopy
SMSI	strong metal-support interaction
SWCNT	single-walled carbon nanotube
T	temperature
TEM	transmission electron microscopy
TGA	thermogravimetric analysis
TOF	turnover frequency
UPD	under-potential deposition
v	potential scan rate
XPS	X-ray photoelectron spectroscopy
XRD	X-ray diffraction
v	kinematic viscosity of the solution
ω	electrode rotation rate

3. INTRODUCTION

The rapid increase in the consumption of conventional energy around the globe and its detrimental environmental impacts pose serious threats to human health and environmental protection. Finding sustainable and eco-friendly energy resources has become one of the main challenges for the 21st century scientists. Several technologies have been introduced in the past years for the production of energy from renewable and sustainable resources in order to minimise the consumption of hydrocarbon fuels. Low-temperature fuel cell such as proton exchange membrane fuel cell (PEMFC) is considered as one of the most promising, 21st century renewable energy conversion devices for future vehicles and portable power sources. Fuel cells directly convert the chemical energy of fuel and oxidant into electricity with high efficiency through complex electrochemical processes.

The slow kinetics of oxygen reduction reaction (ORR) at the fuel cell cathode, rare availability and high cost of platinum, and durability of the Pt nanoparticles (NPs) in the fuel cell operating conditions are the main obstacles in the industrial development of PEMFC. Owing to their remarkable activity towards the sluggish ORR, platinum is used as preferred and effective cathode catalyst. However, due to the high cost of the Pt metal, the cost of the fuel cell is decidedly dependent on the price of platinum in the stock market. In order to minimise the loading and increase the efficiency of the Pt catalysts, carbon-based support materials are preferably used due to their remarkable structural properties and electrical conductivity. Degradation of the deposited Pt NPs and/or the carbon support in the fuel cell operation condition is another serious issue. Owing to the high cost and rare availability of the Pt metal, considerable efforts are made to substitute or to increase lifetime of the Pt electrocatalysts. Engineering advanced carbon-based support materials, core-shell structures, Pt-transition metal alloys, and Pt bimetallic surfaces are some of the well-known strategies developed recently to improve the activity and long-term durability of the electrocatalyst. One of the most effective approaches is to incorporate corrosion resistant metal oxides such as TiO_2, SnO_2 and WO_3 into the carbon support. Introducing metal oxides at the interface increases lifetime of the Pt catalyst because of their capability to inhibit degradation. Such oxide-carbon nanocomposites also enhance electrocatalytic activity of the Pt catalysts by increasing the electronic density over the catalytic centres because of the strong metal-support interaction (SMSI).

The main objectives of this research were to investigate the surface morphology and electronic modification of the catalytic centres at the interface of various Pt-based catalysts and their effect on the electrocatalytic activity and durability of the catalysts. In the first part of this work Pt particles of various sizes and shapes were generated electrochemically on the surface of acid-treated multi-walled carbon nanotubes (MWCNT). The ORR activity of the prepared catalysts was investigated in acid media [I]. In the second part, Pt deposited on

nitrobenzene-functionalised graphene nanosheets, reduced graphene oxide and nitrogen-doped reduced graphene oxide were synthesised and investigated for ORR activity and durability [II, III]. As a continuation, ORR activity of the Pt NPs sputter-deposited on MWCNT was investigated after heat-treatment at various temperatures [IV]. In the next part, ORR activity and long-term durability of the Pt nanoparticles deposited on TiO_2 coated MWCNT catalysts were investigated in acid and alkaline media [V, VI]. The final work was devoted to investigating ORR activity and long-term durability of Pt NPs photo-deposited on Vulcan carbon, SnO_2 nanopowder and SnO_2-C nanocomposites in acid media [VII].

4. LITERATURE OVERVIEW

4.1 The oxygen reduction reaction

Oxygen electroreduction is one of the most important and extensively studied electrocatalytic reactions [1]. In general, the efficiency of a PEMFC is defined by the rate of the oxygen reduction reaction (ORR) in comparison to that of hydrogen oxidation. The electrochemical reduction of oxygen includes a complex multielectron process with many elementary steps proceeding through different reaction intermediates. The sustainable development and commercialisation of fuel cell technology mainly depends on the fabrication of more efficient and durable electrocatalysts for oxygen reduction at cathode [1, 2]. Therefore, it is essential to identify and understand the fundamental aspects governing the ORR mechanism in fuel cell operating conditions. Ideally, the O_2 reduction reaction proceeds either via a direct four-electron pathway (from O_2 to H_2O) or via two-electron pathway (from O_2 to H_2O_2) in both acid and alkaline media.

The four-electron pathway is more efficient producing water in acid media, as given below:

$$O_2 + 4H^+ + 4e^- \rightarrow 2H_2O \qquad E° = 1.229\ \text{V} \qquad (1)$$

The two-electron pathway (also called partial reduction) produce hydrogen peroxide in acid media (2) that can further reduce to water (3) and/or catalytically decompose (4):

$$O_2 + 2H^+ + 2e^- \rightarrow H_2O_2 \qquad E° = 0.67\ \text{V} \qquad (2)$$

$$H_2O_2 + 2H^+ + 2e^- \rightarrow 2H_2O \qquad E° = 1.77\ \text{V} \qquad (3)$$

$$2H_2O_2 \rightarrow 2H_2O + O_2 \qquad (4)$$

The four-electron pathway in alkaline media is given below:

$$O_2 + 2H_2O + 4e^- \rightarrow 4OH^- \qquad E° = 0.401\ \text{V} \qquad (5)$$

The two-electron pathway in alkaline media yields HO_2^- intermediate (6) that is further reduced to OH^- (7) or can catalytically decompose (8):

$$O_2 + H_2O + 2e^- \rightarrow HO_2^- + OH^- \qquad E° = 0.065\ \text{V} \qquad (6)$$

$$HO_2^- + H_2O + 2e^- \rightarrow 3OH^- \qquad E° = 0.876\ \text{V} \qquad (7)$$

$$2HO_2^- \rightarrow 2OH^- + O_2 \qquad (8)$$

[3–7].

Electrochemical O_2 reduction is a surface sensitive reaction and is influenced by various parameters such as pH of the electrolyte solution, size and shape of the catalysts nanoparticles and the chemical nature of the support.

The overall reaction pathways in acid media is presented in scheme 1 [7].

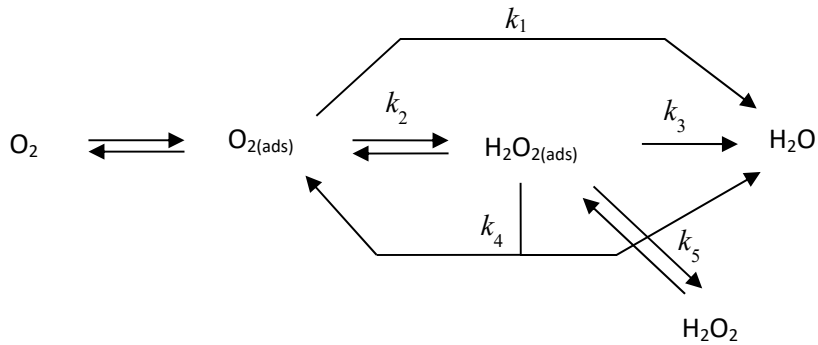

Scheme 1. Schematic representation of O_2 reduction in acidic media. The rate constant for each individual reaction pathway is denoted by (k_i) while the adsorbed species are represented by (ads).

The standard potential for the O_2/H_2O couple is 1.23 V but the working potential of oxygen cathode in the fuel cell is below 0.8 V, which means that there is a potential loss of 400 mV [8]. This potential loss is about 10 times higher in comparison to H_2 oxidation on anode and is attributed to the sluggish kinetics of the ORR.

4.2 Oxygen reduction on platinum electrodes

According to the classical Sabatier principle, the activity of a catalyst for a particular reaction is defined by the optimum "bond strength" between the catalyst and the reacting species [9]. Density functional theory (DFT) calculations revealed that the ORR activity of a catalyst largely depends on the binding energy between the oxygen intermediate and the adsorption sites at catalyst surface [10, 11]. It has been demonstrated earlier that Pt occupy the most optimum position on the volcano plot constructed for the ORR activity on various electrocatalysts, confirming Pt as the most active catalyst for the electrochemical reduction of oxygen [12]. The ORR activity and stability of Pt-based electrocatalysts has been comprehensively investigated and reported by various research groups in the past few decades [13–19]. The research is mostly focused on investigating the surface morphology of the catalyst, reaction mechanism at the interface and physical parameters such as particle-size/shape effect and support effect. The objectives include minimising Pt loading with maximum

possible efficiency and increasing lifetime of the catalyst for practical fuel cell applications. Investigating O_2 reduction on single-crystal Pt electrocatalysts provides insight into the effects of the Pt structure on the reaction kinetics [20–25]. Therefore, the oxygen reduction behaviour on single-crystal Pt surfaces such as Pt(111), Pt(100), and Pt(110) have been extensively studied by many research groups. For instance, Shao et al. reported that the ORR activity on single-crystal Pt surface is defined by the orientation of the steps and terrace on the catalyst surface [26]. The ORR activity of single-crystal Pt catalysts in a weakly adsorbed electrolyte such as $HClO_4$ solution, follows the order of Pt(100) $\ll$ Pt(111) $\approx$ Pt(110). These results are in good agreement to the ones reported previously [27]. The decrease in the ORR activity of Pt(100) facets is due to the relatively strong adsorption of Cl^- ions on this surface as compared to Pt(111) and Pt(110). However, in case of strongly adsorbed electrolyte such as H_2SO_4 solution, the ORR activity on Pt(111) is considerably lower as compared to Pt(100) and Pt(110) because of the relatively stronger adsorption of tetrahedrally bonded (bi)sulphate anions on the (111) facets [20].

Feliu's group has concluded that O_2 reduction is a structure-sensitive reaction in both perchloric and sulphuric acid media [23]. The results showed that the adsorption of anions and formation of oxides on the electrode surface contribute to the structure sensitivity of the ORR, while the adsorption energy of O_2 on the different adsorption sites plays a secondary role in the ORR activity of the catalysts. The ORR process is also structure sensitive in the H_{UPD} region [20]. For instance, the ORR activity on the H_{ads}-modified Pt electrodes follows the order of Pt(111) <Pt(100) <Pt(110) indicating that the adsorbed hydrogen decreases the number of sites available for the O-O bond breaking that leads to the formation of peroxide. Markovic et al. summarised that the ORR kinetics on Pt(*hkl*) surfaces depends on the structure sensitive adsorption of spectator species such as OH_{ads}, $HSO_{4(ads)}$, Cl_{ads}, etc. [17]. Following significant research on single-crystal Pt surfaces for ORR activity, considerable efforts have been devoted to investigate the structural effects of shape-controlled Pt nanostructures on the ORR activity [26]. It was observed that octahedral platinum nanoparticles (NPs) bound by (111) facets are more active towards O_2 reduction than cubic Pt NPs bound by (100) facets [28]. The main problem regarding such shape-controlled Pt NPs is their stability in the O_2 reduction conditions since they have a tendency to evolve to the most stable, thermodynamically equilibrated shape [29]. In general, reducing particle size leads to the exposure of more Pt atoms on surface that improves utilisation efficiency of the catalyst by increasing the active surface area. However, it has been revealed that the intrinsic properties of the catalyst changes dramatically with particle size [30]. For example, if the Pt particle size is reduced from 5 to 1 nm, the distributions of Pt(111) and Pt(100) terrace sites decrease considerably and the low coordination number edges and kinks become more predominant [26]. The ORR activity is lower in the latter case because of the relatively stronger O_2 bonding energies. According to Markovic et al., decreasing the particle size of cubo-octahedral Pt particles below 6 nm leads to a decrease in

the relative fraction of particle surface terminated by (100) faces and becomes zero when the Pt particle size is 1.8 nm [8]. It has been observed that an increase in the Pt particle size decreases the onset potential that in turn, increases the specific current density [31]. The maximum mass activity is observed for the nanoparticles in the range of 3.5 to 4 nm diameter. The O_2 reduction activity of thin-film Pt electrodes (0.25–20 nm) prepared by vacuum evaporation, has been investigated earlier [32]. It was found that the specific activity of the catalyst was higher in 0.1 M $HClO_4$ solution and increased with the increasing thickness of the Pt film while in 0.05 M H_2SO_4 solution, the specific activity was independent of the Pt film thickness.

Several remarkable investigations have been reported regarding the kinetics of the ORR on Pt-based electrocatalysts [33–39]. In general, it is desirable to have O_2 reduction reaction occurring at potentials as close as possible to the reversible electrode potential with a satisfactory reaction rate. Studies have shown that the electrode surface is a mixture of Pt and PtO at higher potentials (> 0.8 V), while at lower potentials, the surface is pure Pt, indicating that the ORR kinetics on Pt electrode is not the same in different potential ranges. For example, at high potential, the Tafel slope value of -60 mV is obtained, while at low potential, a value of -120 mV is observed [40–42]. This indicates that the ORR kinetics depends on the coverage of surface oxides. On a Pt/PtO surface the ORR mechanism is different from that on a pure Pt surface. Briefly, on a Pt/PtO surface, pseudo 2-electron reaction is the rate-determining step, resulting in a Tafel slope value of -60 mV [40]. However, on a pure Pt surface, the first electron transfer to the adsorbed O_2 molecule is the rate-determining step, which gives the Tafel slope value of -120 mV. Damjanovic's group has demonstrated that the enthalpy of activation in the low current density with a Tafel slope value of -60 mV is the same as that in the high current density with the Tafel slope value of -120 mV revealing that the first charge-transfer is the rate-determining step in both regions [43, 44]. Moreover, change in the Tafel slope values is due to the change in the adsorption conditions associated with reaction intermediates and adsorbed oxygen species at the critical coverage.

4.3 Oxygen reduction on carbon-supported Pt electrocatalysts

To enhance the utilisation efficiency of Pt electrocatalyst, it is important to disperse Pt nanoparticles uniformly on a suitable support material [45]. Carbon-based materials (e.g. carbon black, graphene, carbide-derived carbons, carbon nanotubes and carbon nanofibers) offer a variety of properties such as high chemical stability and mechanical strength, high surface area and excellent electronic conductivity, making them promising support for Pt NPs [46–52]. Before the use of carbon as a support material, it was not very practical to use metal nanoparticles as electrocatalysts because of their tendency to aggregate in the absence of a suitable support. Hence, fabrication of the uniformly dispersed Pt

NPs on carbon-based support in the past few decades brought significant progress in the fuel cell technology [18, 53–55]. Carbon black is one of the most widely used support materials, because of its high surface area and electronic conductivity [52, 56, 57]. Pt nanoparticles can interact and get attached to various functional groups such as –CO, -COOH and –CN, present at the surface of carbon black [16, 58–60]. Therefore, it is possible to obtain highly dispersed Pt NPs on the porous carbon surface which can be used as fuel cell cathode catalyst with reduced Pt loading and increased power density.

Watanabe and co-workers have investigated dependence of the ORR activity on the loading of highly dispersed Pt NPs on carbon black [56]. They demonstrated that the area-specific ORR activity of the Pt/C catalyst in 0.1 M $HClO_4$ solution does not depend on the Pt-loading in the range of 19.2 to 63.2%. Jiang and Yi investigated the thickness effect on the ORR activity of Pt deposited on carbon [61]. They reported significant influence of the catalyst layer thickness on the ORR activity and Pt utilisation efficiency. It was concluded that the optimum thickness of the catalyst layer should be around 2–4 μm for reasonable ORR activity. Leontyev et al. investigated the particle size effect on the ORR activity of Pt nanoparticles (1.8–5.4 nm) supported on carbon [62]. They concluded that the overall shape of the nanoparticles changes with decreasing particle size and the fraction of Pt(111) facets increases.

Loading effect of the high surface area carbon-supported platinum nanocubes synthesised by oleylamine/oleic acid method has been investigated for the ORR activity in acidic and alkaline media [63]. Cyclic voltammetry measurements revealed hydrogen adsorption/desorption peaks in the H_{UPD} region, attributed to the Pt(100) facets. The specific and mass activities of the catalysts were found independent of the Pt loadings in both acidic and alkaline media. However, the half-wave potential increased consistently with increasing Pt loading. The electrocatalytic activity of thin film electrodes based on novel high surface area carbon from Johson Mattey (56 wt% Pt/AC01 Hispec 9100) was compared to that of the conventional 40 wt% Pt/Vulcan XC-72 catalyst [64]. Due to the smaller particle size and better Pt utilisation, the novel catalyst material showed much higher electrochemically active surface area and mass activity than the conventional Pt/C. However, Tasaka and co-workers reported the effect of agglomeration on the ORR activity of 20 wt.% Pt/C catalysts, using the rotating ring-disk electrode (RRDE) technique [65]. They revealed two-electron reduction pathway on Pt/C catalysts by the formation of H_2O_2, which is negligible on bulk Pt electrode.

In addition to carbon black/Vulcan carbon, graphene has also shown significant properties as a catalyst support for PEMFC. It has been demonstrated that Pt nanoparticles supported on functionalised graphene are more active towards O_2 reduction and more durable than Pt/C [66]. The functional groups present at the graphene surface interact strongly with the catalyst nanoparticles and therefore inhibit agglomeration and degradation. In order to prevent stacking, ultrafine carbon black is usually added to graphene sheets [67]. Adding carbon black to the graphene sheets also enhances the ORR activity of the catalyst by

facilitating diffusion of the O_2 molecules through the sheets [68]. Durability measurement revealed that Pt deposited on rGO/C composite are more durable than commercial Pt/C retaining 95% electrochemical surface area after 20,000 ADT cycles. Mechanism of the ORR on Pt NPs deposited on defective graphene has been investigated by Wilcox and Lim [69]. They reported that graphene support promote charge transfer from platinum to oxygen and limit the degree of relaxation of Pt NPs by lowering the oxygen dissociation activation energy from 0.37 to 0.16 eV. It also reduces stability of the HO* intermediate species that in turn, decreases the energy barrier of the rate-determining step.

It has been demonstrated that doping graphene sheets with heteroatom also prevents aggregation of the supported nanoparticles and greatly improves their distribution on the support surface [70, 71]. Zhou et al. concluded that incorporating heteroatoms in the sp^2 lattice of graphitic carbon can modify the electronic structure of the support and improve the ORR activity of the catalyst by offering favourable sites for O_2 adsorption or splitting [72]. Various heteroatom-doped graphene materials have been used as support for Pt-based ORR electrocatalysts [73–75]. The electronic interaction between the heteroatom-doped nanocarbon materials and Pt clusters appears to be the main factor for improved electrocatalytic activity towards the ORR [75–77]. Nitrogen-doped graphene supported Pt nanoparticles were employed as a cathode catalyst in polymer electrolyte fuel cells [78].

Multi-walled carbon nanotubes (MWCNT) have some outstanding properties such as high surface area, remarkable electrical conductivity, high chemical stability, corrosion resistance and mechanical strength, which make them a promising support material for fuel cell electrocatalysts [79–82]. However, it is more challenging to get high Pt loading on nanotubes because of their high crystalline structure and presence of fewer functional groups on the surface [59]. Pt/MWCNT has recently been prepared through chemical procedure using a mixture of chloroplatinic acid, polyvinylpyrrolidone and ethylene glycol [46]. Electrochemical measurements showed improved ORR activity of the Pt/MWCNT catalyst, which was attributed to the dispersion of Pt NPs on the pyrenecarboxylic acid functionalised MWCNTs. Rahsepar et al. synthesised Pt/MWCNT electrocatalysts for ORR by impregnation method using microwave heating [79]. Electrochemical measurements of the prepared catalysts showed high ORR activity with typical four-electron O_2 reduction pathway. Another approach for the dispersion of Pt NPs on MWCNTs is the in situ decomposition of platinum acetylacetonate in liquid polyols [83]. Pt NPs sputter-deposited on MWCNT have been investigated for O_2 reduction and durability [82]. It was demonstrated that magnetron sputtering technique can be utilised for the preparation of efficient fuel cell catalysts. The prepared Pt/MWCNT electrodes showed higher ORR activity than that of bulk Pt electrode. Sahoo et al. prepared a hybrid carbon structure of partially reduced-exfoliated MWCNTs as a support material for Pt NPs [84]. The specific and mass activities of the prepared catalyst were compared and found to be higher

than those of commercial Pt/C. Recently, the electrochemical stability of Pt NPs deposited on the surface modified MWCNTs has been studied [46]. A uniform dispersion of Pt NPs was observed by modifying the surface of MWCNTs, which also improved the ORR activity of the Pt/MWCNT electrocatalyst. Various chemical and physical methods have been used for the synthesis of Pt/MWCNT electrocatalysts to improve its ORR activity and long-time durability.

Electrochemical deposition is one of the most efficient and versatile methods used for the direct growth of Pt NPs in a controlled manner [85–90]. Chen et al. deposited porous Pt NPs on a carbon nanotube (CNT) film in 0.5 M H_2SO_4 solution using the electrodeposition technique [91]. They succeeded to prepare Pt aggregates of different shapes and morphology by tailoring the deposition parameters. The prepared electrocatalysts showed higher ORR activity and durability than commercial Pt/C in acidic medium. Pt NPs have been electrodeposited on MWCNT/carbon paper using H_2PtCl_6 (10 g L^{-1}) and HCl (60 g L^{-1}) bath [92]. It was found that the particle size distribution mainly depends on the electrodeposition potential, uniform distribution of Pt NPs was observed at -0.6 V vs saturated calomel electrode (SCE). Magnetron sputtering is a contemporary physical vapour deposition technique used to achieve highly dispersed and rather uniformly distributed nanoparticles on carbon supports [93–96].

4.4 Oxygen reduction on Pt/MO_x-C electrocatalysts

Despite their unique properties and successful applications, carbon-based materials have some serious drawbacks as catalyst support for the electrochemical reduction of oxygen. One of the main problems regarding carbon-based support material is their degradation in the PEMFC operating environment [72, 97]. Several research groups have reported important investigations on the degradation of various carbon supports in fuel cell conditions [98–101]. It has been concluded that degradation of the high surface area carbon support is basically triggered by the corrosion of the disordered carbon sites present in the core of the support particles [102].

In order to inhibit degradation of the catalysts nanoparticles and carbon-based support, several important strategies such as engineering advanced carbon-based support materials, Pt-transition metal alloys, core-shell structures, and Pt bimetallic surfaces have been developed by many research groups [17, 18, 26, 54, 103, 104]. According to Lewera et al., the thermodynamic degradation of carbon support that takes place at $E > 0.9$ V, can be (partially) inhibited by incorporating metal oxide at the interface [105]. Based on their chemical stability, metal oxides can be used as promising alternative support materials for the Pt catalysts in PEMFC [106].

Several metal oxides such as MoO_x, NbO_x, W_xO_y, Ti_xO_y, CeO_x and SnO_x have been introduced by many research groups as supplementary coating to inhibit catalyst degradation [106–109]. Metal-oxide support is known for its

higher stability in the oxidative electrochemical environment [107]. However, one critical issue regarding metal oxide-based supports is that the electrical conductivity of most metal oxides is not comparable to that of the carbon supports [26]. One possible approach is to incorporate metal oxides into the carbon-based support [108]. The influence of the support and the interaction between the Pt nanoparticles and the metal oxide in the oxide-carbon nanocomposites has been investigated [109–111]. Particularly, semiconducting metal oxides with large band-gap such as TiO_2, SnO_2 and WO_3, are investigated by many research groups as catalyst support because of their remarkable corrosion resistance properties [112–118]. Oxide-carbon composites improve the ORR activity and durability of the catalyst by electronic modification of the catalytic centre induced by the strong metal-support interaction at the interface [119, 120]. Shul and co-workers have recently reported a more active and durable cathode catalyst by depositing Pt on CNF/TiO_2 composite using the microwave polyol method [121]. Moreover, Pt NPs sputter-deposited on TiO_2-coated MWCNT have shown improved ORR activity in acid media [81]. Durability measurement confirmed that Pt-TiO_2/MWCNT catalyst is more durable than commercial Pt/C.

It has been demonstrated by many groups that TiO_2-based support material enhances the ORR activity and durability of the Pt catalysts mainly because of the metal-support interaction [122–129]. For example, Ji et al. have recently reported better durability of the Pt/TiO_2 catalyst supported on CNTs as compared to that of the commercial Pt/C, which can be attributed to the strong metal-support interaction [130]. Matsumoto and co-workers have recently reported Pt NPs anchored on TiO_2/cup-stacked CNTs with enhanced ORR activity and durability [126]. The catalyst nanoparticles were anchored to TiO_2 matrix by photo-deposition (PD). It was found that the induced electronic interaction between the TiO_2 and Pt NPs resulted into increased ORR activity. Moreover, the durability of the electrocatalyst was attributed to the inhibition of agglomeration of the nanoparticles due to TiO_2 support. Another group used different TiO_2 phase composition as support by applying heat-treatment at different temperatures followed by deposition of Pt NPs through colloidal method [122]. They reported higher ORR activity of Pt deposited on TiO_2 annealed at 800 °C than that of the Pt supported on anatase TiO_2. Moreover, long-term stability test was performed by potential cycling between 0 and 1.0 V vs reversible hydrogen electrode (RHE) at a scan rate of 20 mV s^{-1}. It was confirmed that more than 60% of the electrochemically accessible surface area (ECSA) was retained by Pt/TiO_2-800 even after 20,000 potential cycles. Zhao et al. reported Pt supported on TiO_2 modified graphitised nanodiamond as a more durable catalyst than Pt/C [131]. Additive-treated TiO_2 has been studied as an alternative to carbon-based support [123]. Briefly, three types of additives namely urea, thiourea and hydrofluoric acid were added through hydrothermal process and the results were compared to those of non-additive-treated TiO_2. It was observed through transmission electron microscopy (TEM), X-ray diffraction (XRD) and cyclic voltammetry that the TiO_2 support treated with

additives affects the Pt particle size distribution and thus changes the surface area of the catalyst. Furthermore, the ORR activity of the Pt supported on HF-treated TiO_2 was higher as compared to the others because of the formation of highly reduced electronic state. Deposition of thin films of TiO_2 and Pt on Nafion membrane has been carried out by thermal evaporation [124]. The prepared electrode was examined in PEM fuel cell. The ORR measurements showed that the activity of the catalyst increases by incorporating TiO_2 between Pt and Nafion membrane. Rajalakshmi and co-workers also studied durability of TiO_2 as a support for Pt catalyst [125]. The catalyst showed higher electrochemical activity and thermal stability as compared to Pt/C, which was attributed to the highly dispersed Pt atoms and controlled nanostructure of the catalyst on the TiO_2 layer.

Atomic layer deposition (ALD) is one of the most promising techniques used by many groups for the deposition of TiO_2 [81, 132–135]. For instance, Fisher et al. grew vertically-aligned carbon nanotubes by the chemical vapour deposition (CVD) method followed by TiO_2 deposition using the ALD technique and annealing in a tube-furnace at 600 °C for 4 h [136]. The effect of various defect sites on the vertically aligned CNTs on the formation of TiO_2 nanoparticles has recently been studied [135]. Various mass fractions of TiO_2 were grown on the pristine CNTs, plasma-treated CNTs and N-doped CNTs using the ALD technique and the surface morphology, compositions and structure was studied by TEM, X-ray photoelectron spectroscopy (XPS), thermogravametric analysis (TGA) and Raman spectroscopy. It was observed that the nucleation of the TiO_2 is affected by the distribution of the carbon-heteroatoms defect sites rather than structural defects. Utke and co-workers reported that the surface morphology of the anatase layer can be controlled by tailoring the deposition temperature during the ALD process. Moreover, complete coverage of the MWCNTs with continuous TiO_2 layer was achieved by applying a temperature of 60 °C during nucleation and 220 °C in the growth phase [137].

Several groups have recently investigated the electrocatalytic activity and durability of Pt nanoparticles deposited on SnO_2-based support materials [138–141]. Mohamed et al. studied metal-support interactions for Pt NPs deposited on Sb-doped SnO_2 using modified organometallic chemical deposition method [142]. XPS analysis showed that the fraction of oxidised Pt species in the Pt 4f doublet is dependent on the Pt loading in the catalyst, which can be attributed to the electronic modification of the catalytic centres. Investigation of the physicochemical properties of the support for Pt sputter-deposited on SnO_2 has shown a direct influence on the electrochemical properties for the CO oxidation and the ORR [143]. In general, SnO_2 support was found to facilitate adsorption of OH species on Pt that has a positive support influence on the CO oxidation activity, but a negative effect on the ORR activity. Sasaki et al. prepared carbon-free electrocatalysts by depositing Pt NPs on SnO_2 and Nb-doped SnO_2 [144]. They demonstrated that Nb doping increased the electronic conductivity of the catalyst's support that enhanced its ORR activity. According to Labbé et al. the low electrocatalytic activity of Pt/SnO_x/C catalyst, after durability test, can be

either related to the degradation of the uncovered carbon or to the formation of amorphous layer of tin oxide on the surface with poor electrical conductivity [145]. Yin et al. reported that $Pt/SnO_2/C$ catalyst prepared by chemical route is twice more durable than commercial Pt/C [146]. According to them, the high durability of the catalysts is attributed to the SMSI induced by the triple junction nanostructure that inhibits migration and agglomeration of the nanoparticles at the electrode surface.

Among the various possible chemical and physical deposition techniques developed so far, photo-deposition is one of the most efficient and cost-effective approaches for the deposition of Pt NPs, preferably on the metal oxides-carbon support [119]. Maicu et al. reported photo-deposition as an efficient method for Pt, Au and Pd on the surface of TiO_2-based support materials with the maximum yield of ~100% for Pt [147]. The mechanism of Pt photo-deposition via UV irradiation has been reported by some groups [148, 149]. According to Timperman et al. photo-deposition of the Pt nanoparticles on the oxide-carbon composites results in alloy formation at the interface that in turn, modifies electronic properties of the catalytic centre [150]. XPS analysis of $Pt/TiO_2/C$ and $Pt/WO_3/C$ electrocatalysts prepared by photo-deposition have shown increased electronic density on the catalytic centre that improved the ORR activity of the two catalysts [105].

5. EXPERIMENTAL

5.1 Preparation of GC electrodes

Glassy carbon (GC) electrodes were cut from rods (GC20-SS, Tokai Carbon, Japan), pressed in Teflon holders and polished with 1.0 and 0.3 μm alumina slurries (Buehler) in Milli-Q water (Millipore Inc.). After polishing the electrodes to mirror finish, they were sonicated twice for 5 min in isopropanol and Milli-Q water to remove polishing residues. Afterwards, the polished GC electrodes were dried in the oven for 5 min.

5.2 Modification of GC electrodes with acid-treated MWCNT

Multi-walled carbon nanotubes (MWCNT) (purity >95%, diameter 30±10 nm, Nanolab, Inc., Brighton, MA, USA) were purified by acid-treatment [151]. Briefly, MWCNTs were refluxed in a mixture of concentrated H_2SO_4 and HNO_3 (1:1, v/v) at 55 °C for 2 h and then at 80 °C for 3 h. The refluxed MWCNTs were then washed thoroughly with Milli-Q water by centrifugation (3000 rpm, 10 min) followed by vacuum filtration until the filtrate became neutral. Finally, the MWCNTs were dried in vacuum for 15 h. A known amount of acid-treated MWCNTs was then dispersed in 2-propanol (1 mg mL^{-1}). The MWCNT dispersion was then put into the ultrasonic bath for 30 min to get a homogenous suspension. Calculated volume of the suspension was transferred onto the polished GC electrode with a pipette. The loading of MWCNTs on the GC was 0.1 mg cm^{-2}.

5.3 Electrodeposition of Pt NPs on MWCNT/GC electrode

The electrodeposition experiments were carried out in Ar-saturated 0.05 M H_2SO_4 solution containing 1 mM of H_2PtCl_6 (Sigma-Aldrich), using conventional 3-electrode cell configuration. MWCNT-modified GC electrode was connected as working electrode. The deposition potential were applied with respect to SCE, while Pt wire separated by a glass frit from the working solution was used as counter electrode. A series of experiments were performed using two different deposition potentials namely at 0 and -0.35 V vs SCE, which were denoted as procedure A and B, respectively. In each procedure, different number of pulses from 100 to 1500 was applied to observe change in the surface morphology and ORR electrocatalytic activity of the Pt/MWCNT catalysts. However, the pulse time for deposition was kept constant at 250 ms during the whole range of experiments, while the interval at 1.0 V between two consecutive pulses was 3 s. For adequate mass transfer, the electrode was rotated at

1000 rpm in all deposition experiments. The prepared electrodes were then designated as Pt/MWCNT-X_y where "X" denotes the deposition procedure and the subscript "y" is the number of pulses.

5.4 Synthesis of Pt-NB/G catalysts

Graphene nanoplatelets (S_{BET}= 750 m^2 g^{-1}, oxygen content of < 2 wt.% and carbon content of > 98 wt.%) purchased from Strem Chemicals were stirred in 10 mM 4-nitrobenzenediazonium tetrafluoroborate (Sigma-Aldrich) aqueous solution for 30 min, filtered and dried in air. Further decoration of nitrobenzene (NB)-modified graphene nanosheets by Pt nanoparticles was performed using a simple ethylene glycol method described elsewhere [128], yielding a 20 wt.% Pt catalyst supported on NB-graphene (Pt-NB/G). For comparison, Pt electrocatalyst on NB-modified Vulcan carbon XC-72R (Cabot Corp.) was also prepared (Pt-NB/C). Polished GC electrodes were modified with the catalyst ink using the procedure mentioned in sub-section 5.2. Pt loading was calculated to be 32 μg cm^{-2}.

5.5 Preparation of Pt/rGO and Pt/rGO-N modified electrodes

Stock 1 mM solution of Pt(IV) complexes was prepared by dissolving chloroplatinic acid (H_2PtCl_6, 99.95 %, Alfa Aesar) in water. Aqueous solutions of NaOH (0.1 M) and HCl (0.1 M) were prepared with analytical-grade reagents. Graphene oxide (GO) was prepared by chemical oxidation of natural graphite powder by the modified Hummer's method [152, 153]. The powder of as-prepared GO was dispersed in water by sonication for 30 min, then centrifuged (2500 g, 15 min) to precipitate the non-exfoliated large GO flakes. The supernatant of this solution was a stable yellow colloidal suspension of predominantly single-layer graphene oxide flakes with the concentration of 2 mg mL^{-1}. For comparison a powder of nitrogen-doped reduced graphene oxide (rGO-N) (Graphitene Ltd., UK) was used. The rGO-N material was poorly dispersible in water and therefore the suspension of rGO-N was used immediately after the sonication procedure. He and H_2 gases with a purity of 6.0 and 5.0, respectively, were used in experiments with plasma-assisted processing. rGO and rGO-N supported Pt NPs were synthesised by a method similar to that reported earlier [154]. An atmospheric pressure bipolar pulsed discharge in He/H_2 (95/5) gas jet with a continuous gas flow of 100 sccm was used for the net transfer of the plasma active species into the aqueous solution of 0.1 mM of H_2PtCl_6 with small additives of rGO or rGO-N. The current flow (peak value of about 2 mA) was arranged from a thin metal capillary through a plasma jet and over the electrolyte to a grounded Pt wire counter electrode immersed in the liquid. Pt nanocomposites were produced in plasma-liquid interface layer due to reduction

of $PtCl_6^{2-}$ anions by solvated electrons e_{aq} and $H^{\bullet}$ radicals, which are the strongest and cleanest chemical reducing agents known. The volume of the processing solution in a sealed silica cell was 4 mL. The overall temperature of the liquid did not exceed 40 °C during the plasma treatment. In order to decrease the concentration of N_2 and O_2, the solution was deaerated by bubbling helium gas with a flow of 100 sccm during 10 min before plasma ignition. To minimise agglomeration and precipitation of nanocomposites during the plasma processing, vigorous stirring of the solution was arranged by a low-power (~1 W) ultrasonic (113 kHz) transducer contacted the bottom of the silica cell. Before the deposition of graphene-supported Pt catalysts onto the polished GC electrode, the concentration of the as-prepared colloidal solution was increased by about 20 times by simple centrifugal enrichment (10000 g, 10 min) and washing several times with water. Polished GC electrodes were then modified with the prepared catalysts using the procedure mentioned in 5.2. The upper limit of Pt loading on the GC electrode is about 45 μg cm^{-2}, based on the assumption of 100% efficiency of the plasma-assisted reduction of $PtCl_6^{2-}$ anions and centrifugation enrichment.

5.6 Preparation and heat-treatment of Pt/MWCNT catalysts

Pt nanoparticles were sputter-deposited onto MWCNT-modified GC electrodes [82, 93, 155]. Briefly, Pt deposition was performed at room temperature by DC-magnetron sputtering technique using 99.99% pure planar round platinum target of 25 mm in diameter and pure argon (99.999%, AGA). The pressure during the sputtering process was 3×10^{-3} mbar, the DC-power was 2 W, and the distance between target and substrate was 6 cm. Nominal thickness of the Pt layer (calculated from the mass deposited per geometric area of GC) for all the experiments was 15 nm. The GC disk loaded with Pt/MWCNT catalysts were annealed at different temperatures ranging from 300 to 700 ºC in a tube furnace (Carbolite, MTF 12/38/400, UK) for 30 min under constant N_2 (99.999%, AGA) flow. For comparison, some electrodes were studied without annealing. In what follows the modified electrodes are designated as Pt/MWCNT-x, where x marks the annealing temperature while Pt/MWCNT-RT corresponds to the catalyst without annealing.

5.7 Preparation of Pt-TiO_2/MWCNT catalysts

5.7.1 Preparation TiO_2/MWCNT composite by ALD

Polished GC plates were modified with acid-treated MWCNTs following the protocol described in sub-section 5.2 and then subjected to ALD for deposition of TiO_2. Briefly, the process was carried out in a PICOSUNTM R-200 Advanced

Advanced ALD reactor (Picosun Oy, Finland) at the substrate temperature of 250 °C. The precursors, $TiCl_4$ and deionised water were vaporised from cylinders held close to the room temperature (19±1 °C). The precursor vapours were subjected into the reactor chamber alternatively by computer-controlled pneumatic valves while dry N_2 (100 to 110 Pa) was used as a carrier and purging gas. Two different thicknesses of TiO_2 (35 and 50 ALD cycles) were deposited onto MWCNTs modified GC plates for measurements.

5.7.2 Sputter-deposition of Pt NPs on TiO_2/MWCNT

TiO_2/MWCNT modified GC electrodes were subjected to magnetron sputtering for the deposition of Pt NPs. The loading of Pt and TiO_2 is varied to observe change in the ORR activity and durability of the catalysts. The nominal thicknesses of the Pt coatings were 2, 4, 8 and 12 nm, which corresponds to the Pt loading of 4.3, 8.6, 17.2 and 25.8 μg cm^{-2} on the electrode surface, respectively, while that in the case of commercial 20 wt.% Pt/C is 19.5 μg cm^{-2}. Based on the compositions of the electrodes, they are labelled as xPt-yTiO_2/MWCNT where "x" represents the nominal thickness of Pt in nm, while "y" shows the number of ALD cycles.

5.8 Synthesis of Pt/C, Pt/SnO_2 and Pt/SnO_2-C catalysts

5.8.1 Synthesis of SnO_2 nanopowder

SnO_2 nanopowder was synthesised by sol-gel route as described elsewhere [156]. Briefly, 25 mL of tin(IV) isopropoxide (98% metals basis), 10% w/v in isopropanol (Alfa Aesar) was diluted in 24.5 mL isopropanol. 0.5 mL Milli-Q water was added for hydrolysis during vigorous stirring (pH = 5.5). The precipitate formed was then washed with Milli-Q water and dried in oven at 60 °C for 24 h.

5.8.2 Synthesis of SnO_2-C nanocomposites

SnO_2-C nanocomposites with different SnO_2 content (from 20 to 60 wt.%) were prepared by modified sol-gel method [120]. For example, for the synthesis of 20 wt.% SnO_2-C nanocomposites, 200 mg of Vulcan carbon XC-72 (Cabot Corp.) was dispersed in 20 mL of isopropanol and sonicated for 30 min to get a uniform suspension. 1.56 mL of tin(IV) isopropoxide (98% metals basis), 10% w/v in isopropanol (Alfa Aesar™) diluted in 12 mL of isopropanol was added to the suspension at 0 °C with vigorous stirring. Four millilitres Milli-Q water was added at room temperature and allowed to stir for 24 h. Afterwards, the suspension was washed with Milli-Q water, filtered and dried in oven overnight at 60 °C. The dried powder was then heat-treated in air at 350 °C for 3 h.

Following the above procedure, 20, 40 and 60 wt.% SnO_2-C composites were prepared.

5.8.3 Photo-deposition (PD)

Chloroplatinic acid (H_2PtCl_6, Alfa Aesar™) dissolved in isopropanol was added into a photoreactor containing support material dispersed in N_2-saturated Milli-Q water. UV-light from a Xe-lamp (159 W), after passing a water filter (long-pass filter GG40), was allowed to enter the photoreactor through a quartz window for 3 h [157]. Afterwards, the suspension was filtered. The resulting material was washed thoroughly with Milli-Q water and dried overnight in oven at 60 °C. The catalysts prepared by photo-deposition of Pt on Vulcan carbon XC-72, SnO_2 nanopowder and SnO_2-C nanocomposites are designated as Pt/C (PD), Pt/SnO_2 (PD) and Pt/x-SnO_2-C (PD), respectively where "x" represents the nominal mass loading of SnO_2 in the oxide-carbon support. Catalysts prepared by PD of Pt NPs were termed as Pt_{Ph}/MWCNT.

5.9 Synthesis of Pt/C catalysts by carbonyl chemical route

Platinum salt (Na_2PtCl_6, Alfa Aesar™) was dissolved in methanol under CO atmosphere with constant stirring at 55 °C for 12 h. Afterwards, the support material, Vulcan carbon XC-72, was added to the carbonyl complex at room temperature under N_2 flow, followed by continuous stirring for 12 h [157]. The solvent was then evaporated and the resulting powder was washed with Milli-Q water, filtered and dried overnight in oven at 60 °C. The Pt/C catalyst prepared by carbonyl chemical route (CCR) was then heat-treated at 200 °C in H_2 atmosphere for 2 h followed by cooling to room temperature in inert atmosphere.

5.10 Physicochemical characterisation of the catalysts

Surface morphology of the prepared Pt/C and Pt/x-SnO_2-C catalysts was investigated by a scanning electron microscope (SEM) Helios NanoLab™ 600 (FEI) and transmission electron microscope (TEM) (Titan 200, FEI), supplied with energy dispersive X-ray spectrometer (EDS) Super-XTM system. Further characterisation of the catalyst structure was carried out by powder X-ray diffraction (XRD) analysis. The powder XRD patterns for all the catalyst samples were recorded on a Bruker D8 Advanced diffractometer using Ni filtered Cu-K_α radiation and LynxEye line detector. Scanning steps were 0.013° from 3 to 93° (θ-2θ) and total counting time was 328 s per step. Structural phases were identified by using the database of the JCPD-ICDD and COD [158]. Prior to the analysis of the XRD patterns by Rietveld refinement,

instrumental resolution function was performed by using a standard powder sample (Al_2O_3). MAUD software was implemented to perform the Rietveld analysis [159].

The X-ray photoelectron spectroscopy (XPS) spectra were acquired with a SCIENTA SES-100 electron analyzer at 200 eV pass energy. The step size for recording survey spectra was 0.5 eV and 0.1 eV for all narrow-scan spectra. A non-monochromatic dual-anode X-ray tube (Thermo XR3E2) was used for excitation source (Mg $K\alpha_{1,2}$ = 1253.6 eV, FWHM = 0.68 eV) at 300 W. For collecting the survey spectra, the following parameters were used: energy range 600–0 eV, pass energy 200 eV, and step size 0.5 eV. In specific regions, high-resolution scans were performed with the pass energy of 200 eV and the 0.1 eV steps. The pressure in the analysis chamber was kept below 10^{-9} Torr each time.

5.11 Electrochemical measurements

Electrochemical experiments were carried out in 0.05 M H_2SO_4, 0.1 M $HClO_4$ or 0.1 M KOH solutions using a five-necked glass cell equipped with the standard three-electrode configuration. Potential was applied using Autolab potentiostat/galvanostat PGSTAT30 (Metrohm Autolab, The Netherlands). All the potential values are reported with respect to the RHE. Electrochemical characterisation of the electrode surface was carried out by cyclic voltammetry measured in the potential range of 0.05 - 1.2 V at 50 mV s^{-1}. CO stripping experiments were performed by electrochemical oxidation of the pre-adsorbed CO (99.95%, AGA) at the electrode surface in N_2-saturated solutions at a potential scan rate (v) of 5 or 20 mV s^{-1} [160, 161]. The electrochemical reduction of oxygen was studied at various electrode rotation rates (ω) in O_2-saturated (99.999%, AGA) electrolyte solutions using the rotating disk electrode (RDE) setup consisting of an EDI101 rotator with a CTV101 speed control unit (Radiometer Analytical). The background currents measured in Ar-saturated (99.999%, AGA) solutions using the same operating procedure were subtracted from the RDE data. Long-term durability of the catalysts was examined by accelerated durability tests (ADT) performed by subjecting the catalysts to repetitive potential cycling in Ar-saturated solutions. Reproducibility of the electrochemical results was confirmed by measuring at least three electrodes of each catalyst.

6. RESULTS AND DISCUSSION

6.1 Oxygen reduction on Pt NPs deposited on MWCNT

6.1.1 Surface morphology of Pt NPs deposited on MWCNT

SEM images show that Pt particles of different shapes, sizes and number density are formed on the surface of MWCNTs (Figure 1). It was observed that the shape of the particles was strictly dependent on the deposition potential, while the particle size and number density were defined by the number of pulses. Briefly, the particles deposited by procedure A acquired spherical, cauliflower-like shape (Figure 1a-c) while procedure B resulted in the formation of cube-shaped particles (Figure 1d-f). It was also revealed that the Pt nanoparticles formed by procedure A are larger in size than those formed by procedure B. The average aggregate size of Pt/MWCNT-A_{200}, Pt/MWCNT-A_{400} and Pt/MWCNT-A_{1200} was 100, 260 and 400 nm, respectively (Figure 1a-c), while that of Pt/MWCNT-B_{200}, Pt/MWCNT-B_{400} and Pt/MWCNT-B_{1200} was 80, 140 and 180 nm, respectively (Figure 1d-f). Furthermore, it can be seen in Figure 1d-f that at more negative deposition potential the Pt particles are formed not only on the outer MWCNT surface, but also on the areas underneath, while at 0 V the Pt particles were mainly formed at the outer surface of MWCNTs only (Figure 1a–c).

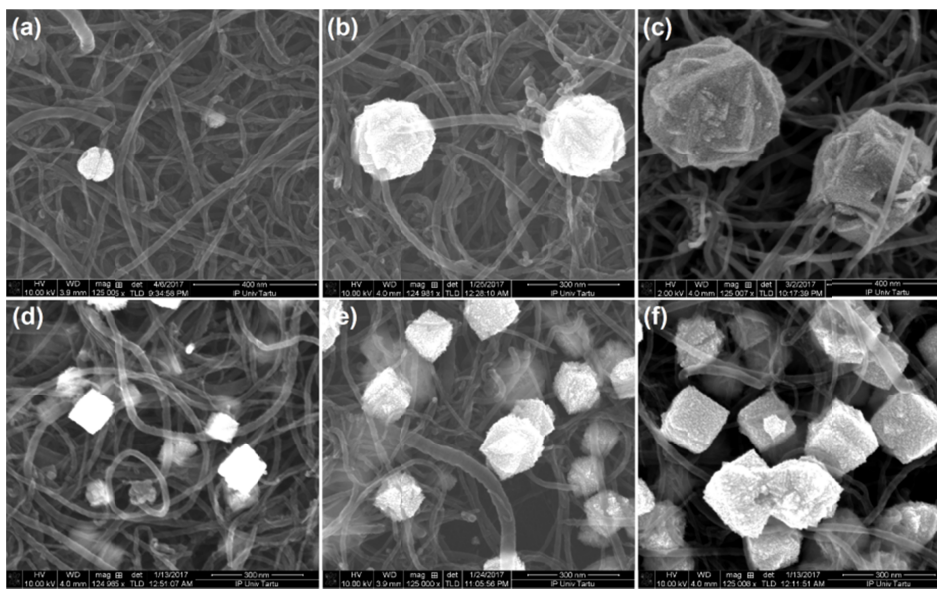

Figure 1. SEM images of Pt/MWCNT-A (a-c) and Pt/MWCNT-B (d-f) with 200, 400 and 1200 pulses, respectively.

As observed in SEM analysis, that the formation of the Pt particles generated at certain nucleation sites, followed a regular pattern. In order to figure out if there is any deposition of smaller Pt NPs dispersed on the surface of MWCNTs, the STEM measurements were carried out as presented in Figure 2. It was confirmed that Pt NPs deposited at certain specific nucleation sites only and there were no smaller Pt nanoparticles dispersed on MWCNTs. The formation of similar clusters at certain active sites on the surface of CNTs has been reported earlier [162–164]. Kar and co-worker suggested that the corroded rough surface of the CNTs after acid-treatment may provide active sites for nucleation [162]. Huang et al. suggested that the number of Pt nuclei formed on the carbon surface depend on the hydrophilicity and uniformity of the support material [163]. Earlier reports confirmed that formation of various functional groups in acid-treated CNTs act as nucleation sites [164]. It can be observed that in the case of Pt/MWCNT-A_{400} (Figure 2a) the Pt aggregate possesses rather compact spherical structure, while on the other hand Pt/MWCNT-B_{200} has dendritic cube-shaped structure (Figure 2b). It was observed that tiny needle-like structures of Pt/MWCNT-B_{200} that resemble the spines of a hedge-hog were pointing outward and thus enhancing the overall ORR activity by increasing the surface area of platinum.

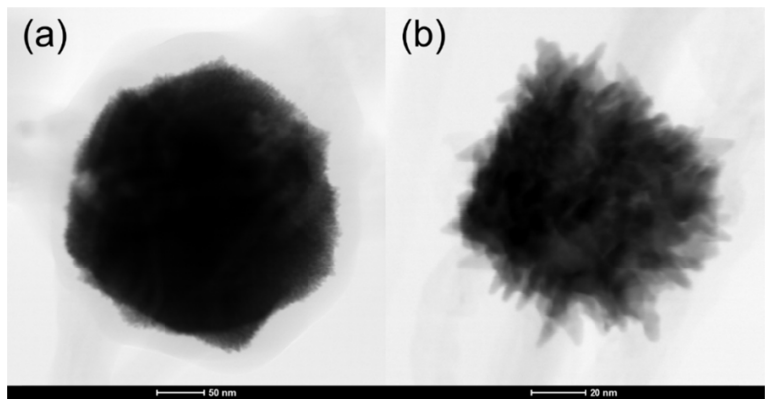

Figure 2. STEM images of Pt/MWCNT-A_{400} (a) and Pt/MWCNT-B_{200} (b).

Recently, many groups have contributed their efforts to figure out the optimum conditions for the electrochemical deposition of Pt NPs onto the support material surface [87–92, 162, 163, 165–168]. Porous Pt aggregates of different shape and surface morphology have been electrochemically deposited on carbon nanotube layer [91]. Basically, two different deposition techniques were applied namely, pulse electrodeposition in which the working electrode was kept switching between two constant potentials and CV at a constant scan rate. It was revealed that Pt aggregates of different size, shape and morphology could be achieved by changing the deposition parameters. The catalysts showed high

ORR activity and stability as compared to that of commercial Pt/C, even after 5000 repetitive potential cycles in the potential range from 0.6 to 1.24 V vs RHE [91]. Another approach is to prepare hierarchical structured catalyst layer for ORR by electrochemical deposition of Pt NPs onto CNTs coated on carbon fibre (CF), which was used as a substrate [162]. Briefly, CNTs were chemically grown on the surface of CF followed by electrodeposition of Pt NPs in H_2PtCl_6 solution. SEM images showed thick forest of Pt NPs coated CNTs finely grown on the surface of CF. The agglomerate size was ranging from ~80 to ~170 nm with an average Pt particle size of ~10 nm. Furthermore, the Pt/CNT/CF electrode showed an enhanced electrocatalytic activity toward the ORR, which is attributed to the Pt NPs clusters formed at the active sites of the CNTs. Unwin and co-workers electrochemically deposited Pt NPs on single-walled carbon nanotubes (SWCNT) grown on Si/SiO_2 [87]. The electrodeposition was performed using cyclic voltammetry for a certain number of cycles, in K_2PtCl_6 solution, where SWCNT network was used as a working electrode. They reported the formation of Pt particles with their size ranged from 175 to 375 nm at certain nucleation sites.

6.1.2 Electrochemical characterisation of Pt/MWCNT

Electrochemical reduction of the pre-adsorbed CO at the electrode surface is a useful approach for decontamination and further characterisation of the electrode surface. The CO stripping experiments were performed on Pt/MWCNT catalysts in 0.05 M H_2SO_4 solution [15, 160, 169]. Figure 3 illustrates characteristic CO stripping voltammogram of the Pt/MWCNT-B_{1200} catalyst. Absence of hydrogen adsorption/desorption peaks in the H_{UPD} region (0.05 to 0.4 V) revealing that the electrode surface is completely blocked by the pre-adsorbed CO, which is removed by oxidative stripping during the second potential cycle (0.05 to 1.0 V). The main CO oxidation peak is centred at ≈0.72 V. It has been reported earlier that the pre-peak in the CO stripping voltammograms of Pt nanoparticles can be attributed to a change in surface morphology such as particle size distribution and aggregation of Pt NPs [170]. Studies with stepped surfaces have shown that the presence of different steps catalyse the oxidation of CO [171–173]. During the third potential cycle, in the same potential range (0.05 to 1.0 V), appearance of the hydrogen adsorption/ desorption peaks confirmed that the pre-adsorbed CO is now completely oxidised [80].

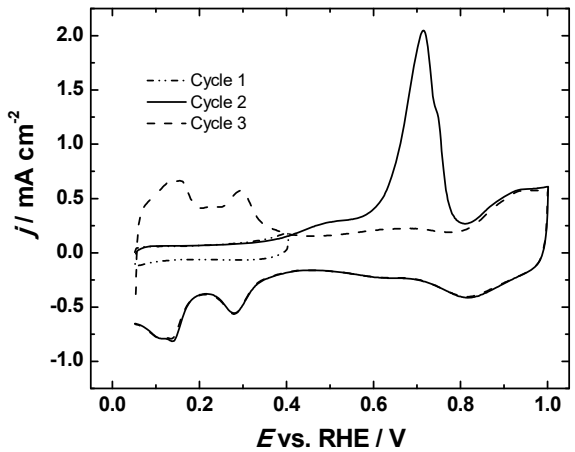

Figure 3. CO stripping profile of Pt/MWCNT-B_{1200} in Ar-saturated 0.05 M H_2SO_4 solution (v = 20 mV s^{-1}). The current densities were normalised to the geometric surface area of GC electrode.

A comparison of the CO stripping profile for Pt/MWCNT-A and Pt/MWCNT-B is shown in Figure 4a and 4b, respectively. It was found that all the electrodes prepared by both electrodeposition procedures (A and B) followed almost the same CO stripping profiles. The only exception was Pt/MWCNT-A_{100} where no Pt was detected and the electrode behaved more like a GC electrode modified with pristine MWCNTs and hence, the electrochemical results for Pt/MWCNT-A_{100} are not presented hereafter. A broad CO oxidation peak at ≈0.72 V and a shoulder at ≈0.75 V was detected in the second potential cycle [174]. The shoulder at ≈0.75 V can be easily detected in Pt/MWCNT-B catalysts but not in the case of Pt/MWCNT-A, especially with increased number of pulses. This can be attributed to the difference in the nature of crystal facets at the surface of the Pt NPs formed at different deposition parameters [174]. The CO stripping peak height increases with increasing the number of pulses, which is attributed to the metal loading. After decontamination and surface characterisation of the electrode surface by CO stripping, CV curves were measured at 50 mV s^{-1} in Ar-saturated 0.05 M H_2SO_4 solution. Three consecutive potential cycles were measured for each electrode in the potential range of 0.05–1.45 V before recording a stable cyclic voltammogram.

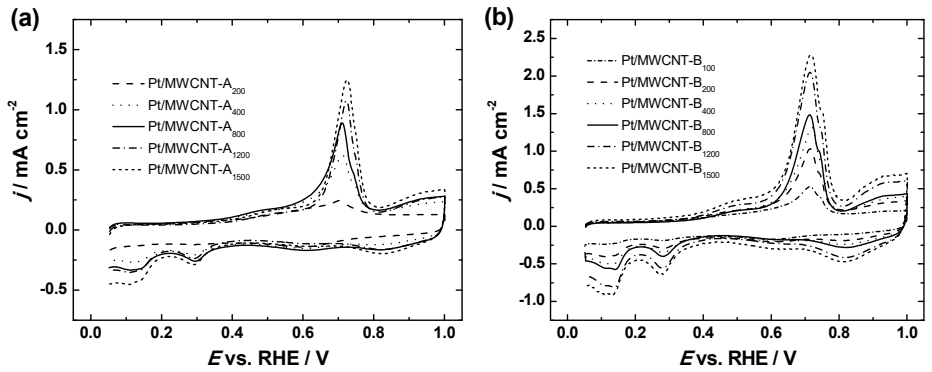

Figure 4. Comparison of CO stripping voltammograms of Pt/MWCNT-A (a) and Pt/MWCNT-B (b) in 0.05 M H_2SO_4 solution (v = 20 mV s^{-1}).

Figure 5a illustrates a comparison of the CV curves obtained for Pt/MWCNT-A at different number of pulses, while Figure 5b shows CV curves for Pt/MWCNT-B at various number of pulses. Like CO oxidation behaviour, Pt/MWCNT electrodes prepared by both procedures showed almost the same profile for cyclic voltammetry. The hydrogen desorption peak at ≈0.14 V is attributed to Pt(110), while that at ≈0.30 V is attributed to Pt(100) crystal facets [174, 175]. Assuming that a charge of ≈210 μC cm^{-2} is required to desorb a monolayer of hydrogen from the Pt catalyst surface, the real surface area (A_r) of the electrocatalyst was calculated by integrating the charge under the hydrogen desorption peaks [176]. The A_r values calculated for all the electrodes studied are given in Table 1. It can be seen that Pt/MWCNT-B possess higher surface areas than Pt/MWCNT-A. This can be attributed to the peculiar dendritic-type Pt clusters formed by procedure B as shown in Figure 2b.

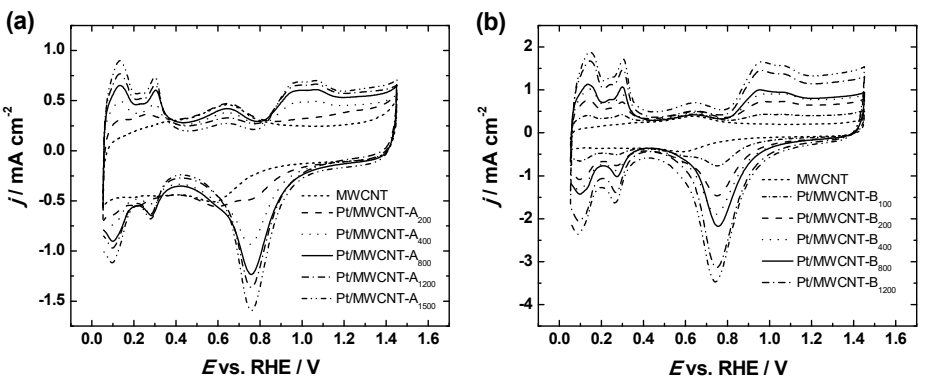

Figure 5. Cyclic voltammograms of Pt/MWCNT-A (a) and Pt/MWCNT-B (b) in Ar-saturated 0.05 M H_2SO_4 solution (v = 50 mV s^{-1}).

6.1.3 ORR studies on Pt/MWCNT catalysts

The electrochemical reduction of oxygen was investigated in O_2-saturated 0.05 M H_2SO_4 solution using the RDE method. The ORR polarisation curves were recorded at 10 mV s^{-1} in the potential range of 0.05–1.1 V. The background current measured in Ar-saturated solution was then subtracted from the RDE data. Only the positive-going potential scans are presented and further analysed. Figure 6a shows the ORR polarisation curves on Pt/MWCNT-B_{400} catalyst measured at various electrode rotation rates (360–4600 rpm). The RDE polarisation data was used to construct the Koutecky-Levich (K-L) plots as shown in Figure 6b. The number of electrons transferred per O_2 molecule (n) during the ORR was calculated using K-L equation as given below:

$$\frac{1}{j} = \frac{1}{j_k} + \frac{1}{j_d} = -\frac{1}{nFkC_{O_2}^b} - \frac{1}{0.62nFD_{O_2}^{2/3}\nu^{-1/6}C_{O_2}^b\omega^{1/2}} \quad (9)$$

where j is the measured current density, j_k and j_d are the kinetic and diffusion-limited current densities, respectively, F is the Faraday constant (96,485 C mol^{-1}), k is the rate constant for ORR, $C_{O_2}^b$ is the concentration of O_2 in 0.05 M H_2SO_4 (1.22×10^{-6} mol cm^{-3}) [177], D_{O_2} is the diffusion coefficient of O_2 in 0.05 M H_2SO_4 (1.93×10^{-5} cm^2 s^{-1}) [177], ν is the kinematic viscosity of the solution (0.01 cm^2 s^{-1}) [178] and ω is the electrode rotation rate (rad s^{-1}). It was confirmed form the RDE data analysed by Eq. (1) that all the Pt/MWCNT electrocatalysts followed the typical four-electron pathway for the electrochemical reduction of oxygen. The four-electron pathway for Pt-based catalysts prepared by electrodeposition method has been reported also earlier [87, 162, 167].

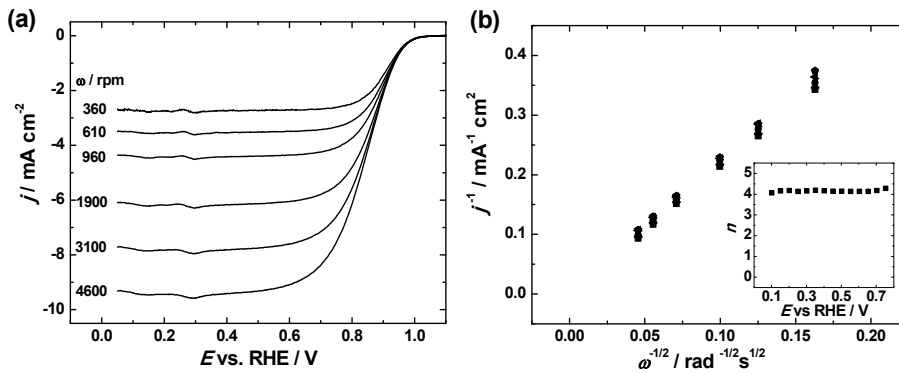

Figure 6. RDE polarisation curves for oxygen reduction on Pt/MWCNT-B_{400} in O_2-saturated 0.05 M H_2SO_4 solution (ν = 10 mV s^{-1}) (a) and K-L plots calculated from the RDE data (b), the inset in figure b shows the potential dependence of n.

Figure 7 displays a comparison of the ORR polarisation curves of Pt/MWCNT-A (Figure 7a) and Pt/MWCNT-B (Figure 7b) with commercial Pt/C measured at 1900 rpm. It was observed that overall the $E_{1/2}$ values increased with increasing pulse number (Table 1). The lowest $E_{1/2}$ value of 0.75 V was shown by Pt/MWCNT-A_{200}. In the case of Pt/MWCNT-A, all the electrodes prepared with the number of pulses ≥800 showed higher $E_{1/2}$ than that of the commercial Pt/C while in the case of Pt/MWCNT-B, the electrodes prepared with the number of pulses ≥400 showed higher $E_{1/2}$ than that of the commercial Pt/C. The highest $E_{1/2}$ value of 0.88 V was shown by Pt/MWCNT-B_{1500}. The deviation of j_d values from the theoretical ones can be attributed to the relatively rough surface of the modified GC electrode.

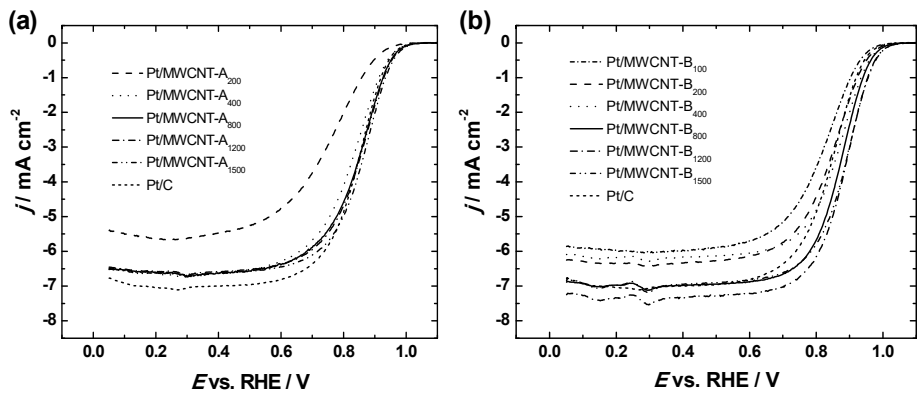

Figure 7. Comparison of RDE polarisation curves for oxygen reduction on Pt/MWCNT-A (a) and Pt/MWCNT-B (b) with commercial Pt/C at 1900 rpm in O_2-saturated 0.05 M H_2SO_4 solution (v = 10 mV s^{-1}).

Further analysis of the ORR data was carried out by constructing mass-transfer corrected Tafel plots for Pt/MWCNT electrodes (Figure 8). The Tafel analysis provides an insight into the ORR mechanism by measuring kinetic currents in the absence of diffusion limitations. Two characteristic Tafel slope regions were observed from which the slope values were determined (Table 1). The Tafel slope values for all Pt/MWCNT-A (Figure 8a) and Pt/MWCNT-B (Figure 8b) electrodes were close to -60 and -120 mV at low current densities and higher current densities, respectively, which indicated that all the electrodes followed the same mechanistic pathway and that the rate of the ORR is determined by the transfer of the first electron to the adsorbed O_2 molecule [82, 179].

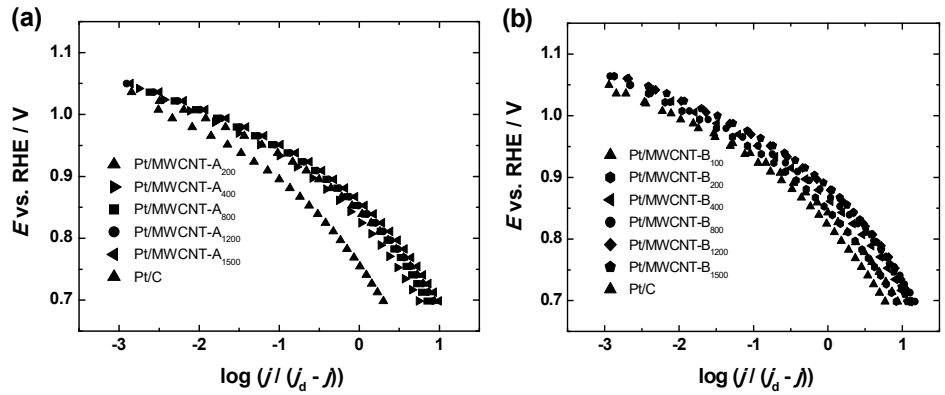

Figure 8. Mass-transfer corrected Tafel plots for oxygen reduction on Pt/MWCNT-A (a) and Pt/MWCNT-B (b) in 0.05 M H_2SO_4 solution.

The specific activity (SA) values of the Pt/MWCNT electrodes for ORR were calculated from the equation given below:

$$SA = I_k/A_r \tag{10}$$

where I_k is the kinetic current and A_r is the real electroactive surface area of the Pt catalyst. All the Pt/MWCNT modified electrodes showed higher SA values than that of commercial Pt/C (Table 1). The electrodes prepared by procedure A showed higher SA than those prepared by procedure B. It was observed that the SA decreased with increasing the number of pulses. In the case of Pt/MWCNT-A, the highest SA (0.45 mA cm^{-2}) was shown by Pt/MWCNT-A_{200}, which is more than 4-times higher than that of the commercial Pt/C. However, a decrease in the specific activities was observed with increasing pulse number to 800 after which a constant value of 0.22 mA cm^{-2} was achieved for both Pt/MWCNT-A_{1200} and Pt/MWCNT-A_{1500}. A similar trend was found for Pt/MWCNT-B electrocatalysts. The SA values drop from 0.42 to 0.23 mA cm^{-2} for Pt/MWCNT-B_{100} and Pt/MWCNT-B_{200}, respectively. Furthermore, Pt/MWCNT-B_{400}, Pt/MWCNT-B_{800} and Pt/MWCNT-B_{1200} showed the same specific activity of 0.18 mA cm^{-2}, while the lowest SA value of 0.16 mA cm^{-2} was observed in the case of Pt/MWCNT-B_{1500}, which was still higher than that of commercial Pt/C catalyst. The specific activities of the electrodes prepared with lower number of deposition pulses are higher than those reported earlier for Pt/C catalysts. Gasteiger and co-workers obtained SA values of 0.20 mA cm^{-2} at 0.9 V in acid electrolyte for state-of-the-art Pt/C catalysts [180]. Li et al. studied composite materials prepared by mixing Pt-coated reduced graphene oxide with carbon black. The SA value obtained from this catalyst was 0.21 mA cm^{-2} [68]. Since the material has dendritic structure and the surface is rather porous, SA is increased with the decrease of surface area.

Table 1. Kinetic parameters for ORR on Pt/MWCNT electrocatalysts in 0.05 M H_2SO_4 solution (ω=1900 rpm).

Electrode	Ar (cm^2)	Tafel slope (mV) lcd	Tafel slope (mV) hcd	$E_{1/2}$ (V)	SA at 0.9 V (mA cm^{-2})
Pt/MWCNT-A200	0.10	−67	−112	0.75	0.45
Pt/MWCNT-A400	0.52	−62	−115	0.82	0.31
Pt/MWCNT-A800	1.02	−63	−115	0.85	0.26
Pt/MWCNT-A1200	1.21	−63	−122	0.85	0.22
Pt/MWCNT-A1500	1.30	−64	−119	0.85	0.22
Pt/MWCNT-B100	0.35	−63	−111	0.82	0.42
Pt/MWCNT-B200	1.02	−69	−113	0.84	0.23
Pt/MWCNT-B400	1.67	−67	−115	0.86	0.18
Pt/MWCNT-B800	2.17	−63	−107	0.87	0.18
Pt/MWCNT-B1200	2.76	−65	−111	0.88	0.18
Pt/MWCNT-B1500	3.25	−68	−118	0.88	0.16
Commercial Pt/C	1.64	−61	−126	0.84	0.13

6.1.4 Long-term durability of Pt/MWCNT catalysts

In addition, accelerated durability tests (ADT) were performed in order to investigate stability of the prepared catalysts in acid media. Figure 9a shows CV curves of Pt/MWCNT-B_{200} during 5000 potential cycles between 0.05 and 1.45 V. As can be seen from the inset of Figure 9a the true area of Pt degraded by almost 48%. Nevertheless, despite the harsh durability testing conditions used the values of $E_{1/2}$ shifted only 15 mV. Figure 9b presents RDE polarisation data before and after 5000 repetitive potential cycles.

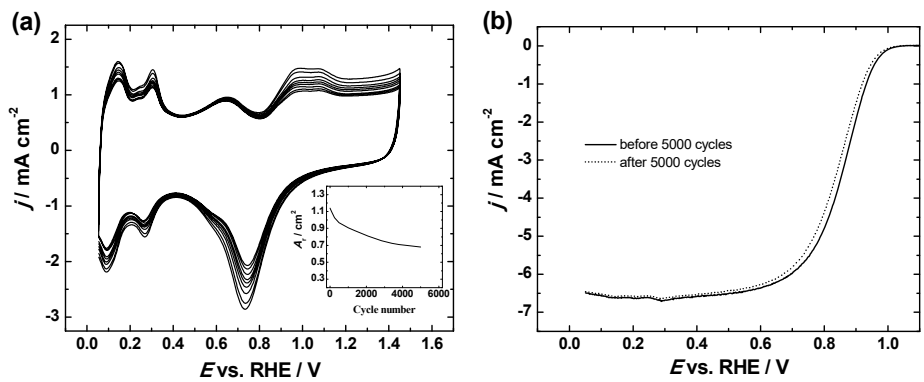

Figure 9. Cyclic voltammograms of Pt/MWCNT-B_{200} recorded during the ADT in Ar-saturated 0.05 M H_2SO_4 solution at 100 mV s^{-1} (a), the inset of Figure 9a shows decrease in surface area; RDE polarisation curves of ORR at 1900 rpm before and after ADT (v = 10 mV s^{-1}) (b).

6.2 Oxygen reduction on Pt-NB/G catalysts

6.2.1 Surface characterisation of Pt-NB/G

SEM analysis of the Pt-NB/G samples revealed that the Pt NPs are uniformly distributed on the NB-modified carbon support (Figure 10a and b). Inset in Figure 10b represents a size distribution for 300 Pt particles analysed and calculated. It can be observed that the Pt NPs possess remarkably narrow particle size distribution on the support surface with an average particle size of ≈3.6 nm. Figure 10c shows the XPS survey spectra of Pt-NB/G catalyst where C1s, N1s, O1s, Pt4f and Pt4d peaks can be detected at the corresponding BE. It was revealed that Pt is present in its zero-valent state. Figure 10d illustrates the XPS core-level spectrum in the N1s region. It was found that the binding energy of N1s corresponds to amino functionality.

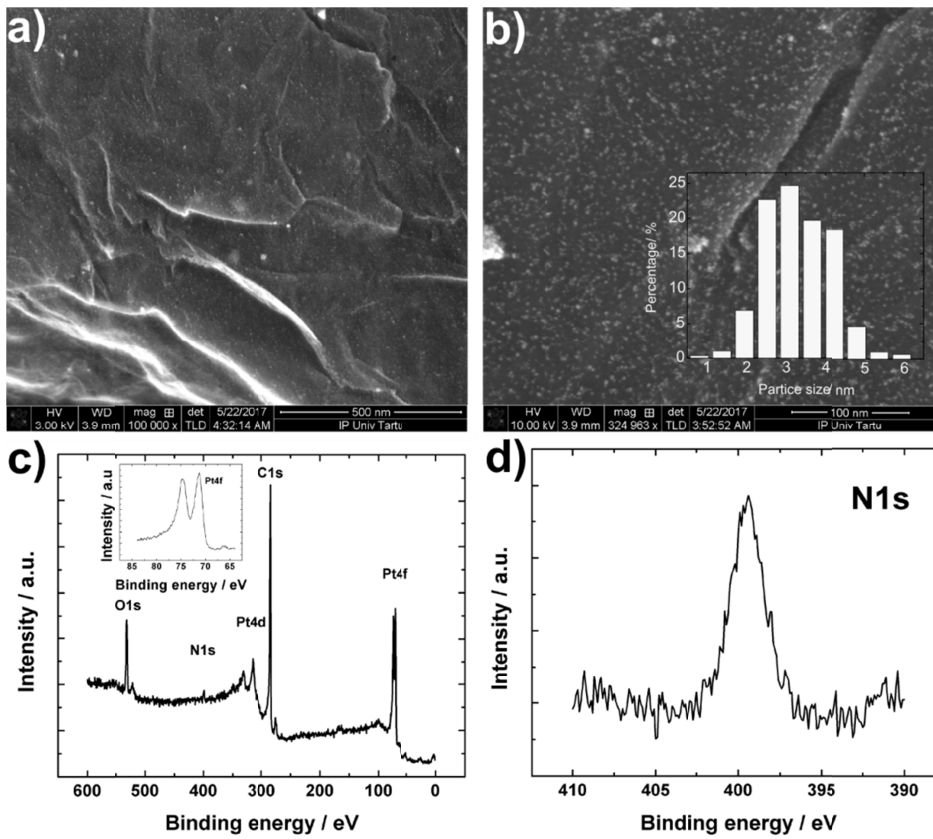

Figure 10. SEM images of Pt-NB/G modified GC electrodes (a and b); Inset of 10b shows Pt particle size distribution; XPS survey spectra for Pt-NB/G sample (c); Inset of 10c shows Pt 4f spectra; the XPS core-level spectrum in the N1s region (d).

6.2.2 Electrochemical characterisation of Pt-NB/G

Surface morphology of the prepared catalysts was further investigated by measuring CV curves in Ar-saturated 0.1 M KOH solution at 50 mV s^{-1} in the potential range of 0.05–1.45 V. Figure 11 illustrates the stable CV curves obtained for Pt-NB/G, Pt-NB/C, commercial Pt/C and bulk Pt electrodes. It can be observed that the overall shape of the cyclic voltammograms of the prepared catalyst is similar to the Pt/C and bulk Pt electrodes. The hydrogen desorption peaks at 0.28 and 0.38 V are associated with Pt(110) and Pt(100) facets [181]. Moreover, Pt surface oxide formation can be observed at ≈0.8 V in the anodic sweep on all catalyst while the reduction peaks are centred at ≈0.7 V in the cathodic sweep. The peak observed at 0.6 V in the anodic sweep on Pt-NB/C catalyst corresponds to the electrochemical oxidation of quinone-type functionalities on the surface of Vulcan carbon.

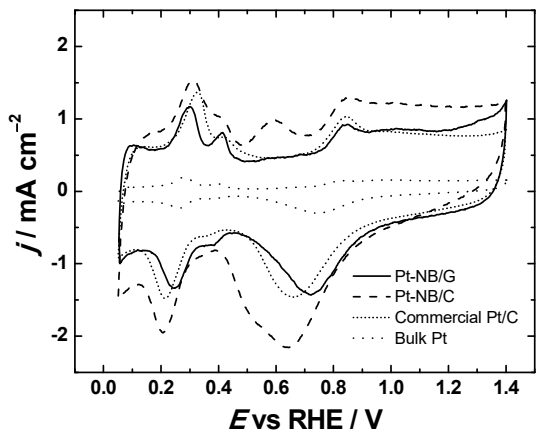

Figure 11. CV curves of Pt-NB/G, Pt-NB/C, commercial Pt/C modified GC and bulk Pt electrodes in Ar-saturated 0.1 M KOH. v = 50 mV s^{-1}.

6.2.3 Oxygen reduction on Pt-NB/G

The electrochemical reduction of oxygen on Pt-NB/G, Pt-NB/C, commercial Pt/C and bulk Pt electrodes was investigated in O_2-saturated 0.1 M KOH solution. Figure 12a illustrates a comparison of the RDE polarisation curves measured at 1900 rpm. The number of electrons transferred per O_2 molecule (n) was calculated from the RDE polarisation data using the Eq. (9). $C^{b}_{O_2}$ is the concentration of O_2 in 0.1 M KOH solution (1.2×10^{-6} mol cm^{-3}) [182] and D_{O2} is the diffusion coefficient of O_2 (1.9×10^{-5} cm^2 s^{-1}) [182]. A four-electron pathway of the ORR was confirmed for Pt-NB/G catalyst. The $E_{1/2}$ value for the ORR on Pt-NB/G modified GC electrode at 1900 rpm was determined to be

0.86 V (Table 2). This $E_{1/2}$ value is 43 mV higher than that of bulk Pt and is close to that found for commercial 20 wt.% Pt/C catalyst ($E_{1/2}$ = 0.87 V). Specific activities of Pt-based catalysts for oxygen reduction were calculated at 0.9 V vs. RHE using Eq. (10).

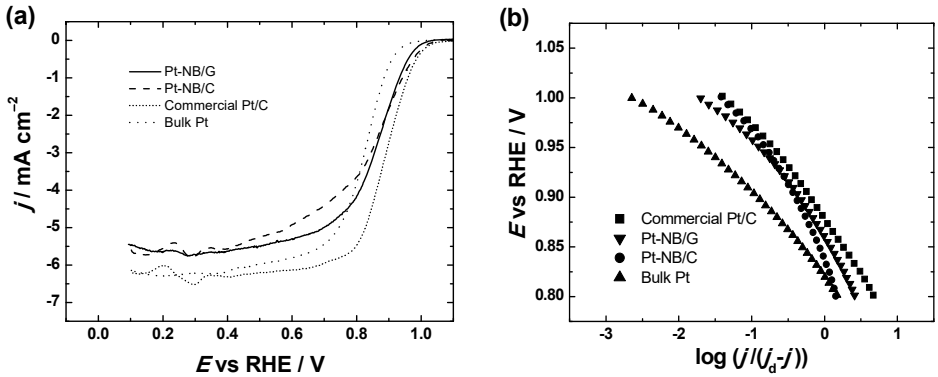

Figure 12. Comparison of RDE results (a) and mass-transfer corrected Tafel plots (b) for O_2 reduction on Pt-NB/G, Pt-NB/C, commercial Pt/C modified GC and bulk Pt electrodes in 0.1 M KOH (ω=1900 rpm).

The results of the ORR kinetics analysis are listed in Table 2. The SA value for Pt-NB/G was 0.18 mA cm^{-2}, which is very close to that obtained for commercial 20 wt% Pt/C catalyst (0.21 mA cm^{-2}). These values of SA are higher than those reported for Pt/NG catalysts in our previous publication [183]. The Tafel slope values have been determined for all the electrocatalysts studied (Table 2). Two distinct regions were obtained for all the catalysts in this study, showing that the ORR mechanism is rather similar.

Table 2. Kinetic parameters for oxygen reduction on Pt-NB/G, Pt-NB/C, commercial Pt/C catalyst and bulk Pt in 0.1 M KOH (ω=1900 rpm).

Electrode	A_r (cm^2)	Tafel slope (mV) lcd	Tafel slope (mV) hcd	$E_{1/2}$ (V)	SA at 0.9 V (mA cm^{-2})
Pt-NB/G	1.73	-72	-129	0.86	0.18
Pt-NB/C	2.62	-89	-169	0.85	0.18
Pt/C	2.35	-84	-110	0.86	0.21
bulk Pt	0.46	-58	-90	0.82	0.05

Durability of the Pt-NB/G catalyst was evaluated by ADT. The catalyst was subjected to 2000 potential cycles between 0.05 and 1.1 V in Ar-saturated 0.1 M KOH (Figure 13). It can be observed in Figure 13a that the catalyst retained

its electrochemically accessible surface area revealing remarkable corrosion resistant capability of the NB/G support. For comparison, durability tests were also performed for the state-of-the-art Pt/C catalyst. Half-wave potential values of the catalysts were calculated from the RDE polarisation curves measured at 1900 rpm before and after the ADT as presented in Figure 13b. It was found that the drop in the $E_{1/2}$ value for Pt-NB/G catalysts during the ADT was 16 mV, while that for the commercial Pt/C was 32 mV. The results obtained in this work suggest that the incorporation of NB into catalyst system offers excellent electrocatalytic behaviour, due possibly to the unique structure of the hybrid where nitrophenyl groups interconnect Pt NPs and graphene support. The superior electrocatalytic properties and remarkable stability in electrochemical conditions makes the Pt-NB/G composite an attractive electrocatalyst for anion exchange membrane fuel cell applications.

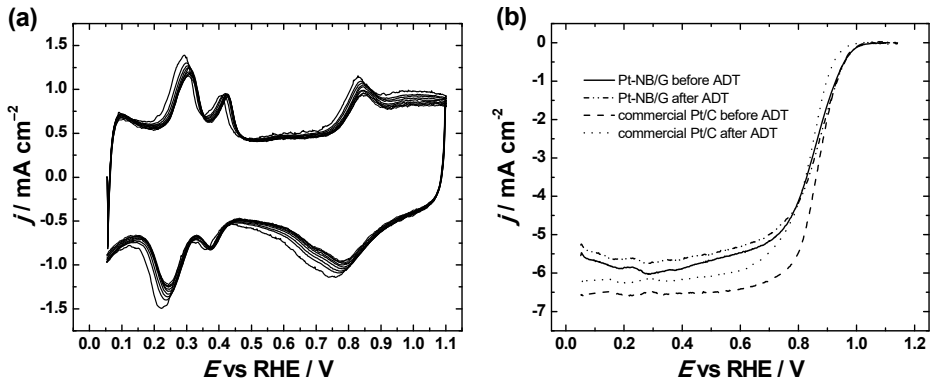

Figure 13. Cyclic voltammograms of a Pt-NB/G modified GC electrode recorded at 50 mV s^{-1} in Ar-saturated 0.1 M KOH solution during the ADT (a) and RDE results before and after the ADT (ω =1900 rpm) (b).

6.3 Oxygen reduction on Pt/rGO and Pt/rGO-N catalysts

6.3.1 Physical characterisation of Pt/rGO andPt/rGO-N

Chemical composition of the rGO-N support and Pt/rGO-N catalyst surfaces was investigated by XPS analysis. Peaks corresponding to C1s, N1s, O1s, Pt4d and Pt4f were observed in the XPS survey spectra. Moreover, the N1s XPS spectra was deconvoluted into 3 peaks located at binding energies of 401.1, 399.6 and 398.3 eV, corresponding to the graphitic, pyrrolic and pyridinic N, respectively. All three types of N species can form strong interactions with Pt atoms [184, 185]. Further information regarding surface morphology of the prepared catalysts was obtained from SEM analysis (Figure 14). As shown in Figure 14a, in Pt/rGO catalyst prepared with NaOH additives, the rGO flakes were not successfully covered by small nonagglomerated Pt NPs. This behaviour may be explained by electrostatic repulsion between the negatively charged Pt NPs and rGO sheets. To trigger the Pt nanoparticle attachment, small additives of diluted HCl were admixed to the solution of Pt NPs containing rGO flakes just after the plasma. As a result, pH of the solution decreased from 7.6 to 4.0 and colloidal solution became unstable – black precipitate separated after a few hours. SEM image of Pt/rGO nanocomposite extracted from the solution is shown in Figure 14b where small nanoparticles dispersed on the surface of rGO sheets can be seen. From general consideration, to achieve homogeneous distribution of Pt NPs over all rGO flakes the concentration of H_2PtCl_6 and rGO as well as HCl additives should be carefully optimised. SEM image of Pt/rGO-N nanocomposite extracted from the solution after the plasma treatment is shown in Figure 14c. Small Pt NPs were homogeneously dispersed on the surface of rGO-N sheets, however, a number of nanoparticles agglomerates were also observed. Pt NPs were produced continuously in the plasma-liquid interface layer and they were ready to deposit immediately to the surface of rGO-N if it was allowed by electrostatic interaction. Therefore, in ideal deposition conditions, Pt NPs are not accumulated in the solution, which prevents the generation of agglomerates. SEM image of Pt/rGO-N nanocomposite is shown in Figure 14d, where small nanoparticles homogeneously dispersed on the surface of rGO-N sheets without agglomeration. Furthermore, nanoparticles attached to the surface of rGO nanoplatelets, prevented restacking of the rGO sheets, resulting in the formation of stable nanocomposites.

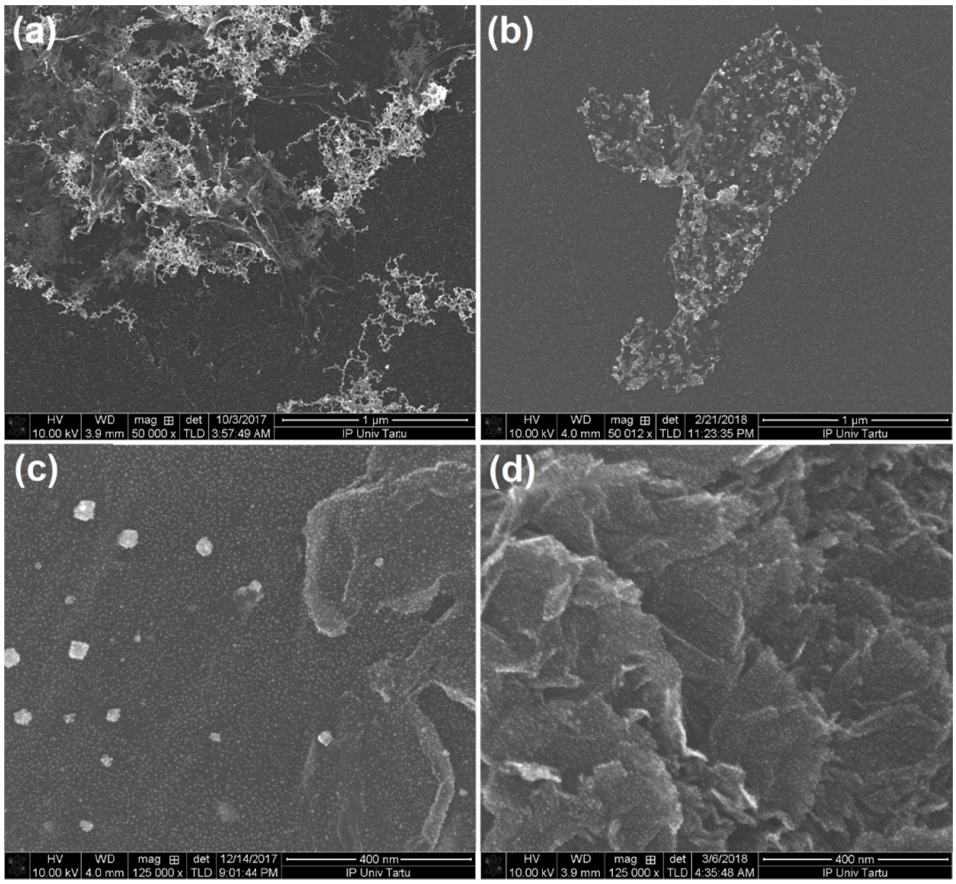

Figure 14. SEM image of Pt/rGO prepared with NaOH additives (pH 7.6) (a); Pt/rGO prepared with NaOH additives, HCl was admixtured after the plasma treatment (pH 4.0) (b). Pt/rGO-N prepared without NaOH additives (pH 3.9) (c), Pt/rGO-N prepared with NaOH additives (pH 5.7) (d).

Figure 15 illustrates TEM and HR-TEM images of Pt/rGO-N nanocomposite with size distribution histogram of the Pt NPs. Quasi-spherical shaped nano-particles with an average diameter of 2.35±0.51 nm (particle agglomerates are excluded) and narrow particle size distributions are obtained. To minimise agglomeration of primary Pt NPs, pH of the starting solution was adjusted to about 9 by small additives of diluted NaOH. After 10 min of plasma processing, slightly grey and stable colloid (pH 5.7) was obtained.

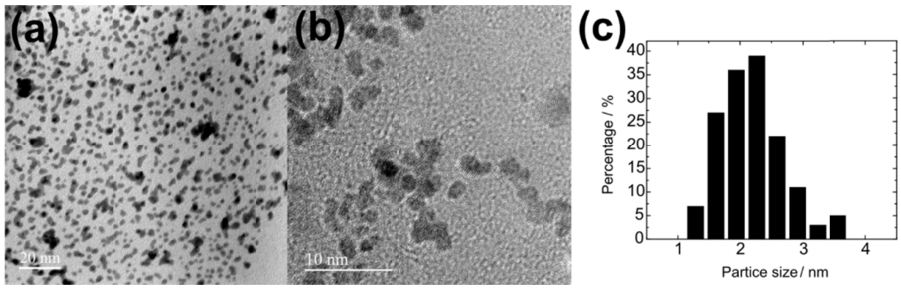

Figure 15. TEM (a) and HR-TEM (b) images of Pt/rGO-N nanocomposite; size distribution histogram of Pt NPs in Pt/rGO-N (c).

6.3.2 Electrochemical characterisation Pt/rGO and Pt/rGO-N

Figure 16 displays comparison of the CO stripping profiles of the Pt/rGO and Pt/rGO-N catalysts in 0.05 M H_2SO_4 (a) and 0.1 M KOH (b). It can be seen that in acid media (Figure 16a), Pt/rGO and Pt/rGO-N catalysts showed nearly the same CO oxidation profiles while in alkaline media, considerably higher current densities were obtained for Pt/rGO-N (Figure 16b). Formation of a well-defined surface oxidation peak at ca 0.85 V observed for Pt/rGO-N catalyst can be explained by Pt oxide formation. Plasma jet treatment is considered to be a clean method, since no reducing agents and stabilising surfactants are used during synthesis. Nevertheless, trace amount of Cl^- anions may remain from precursors and further exacerbate the catalyst efficiency by blocking the active sites at the catalytic centres [186]. Therefore, it is strongly recommended to include CO stripping technique in electrode preparation routine. In PEM fuel cells, chloride impurities arise from the membrane electrode assembly (MEA) preparation and less than 5-ppm of chloride residues can result in a voltage loss of 50 mV and affect the open-circuit voltage [17].

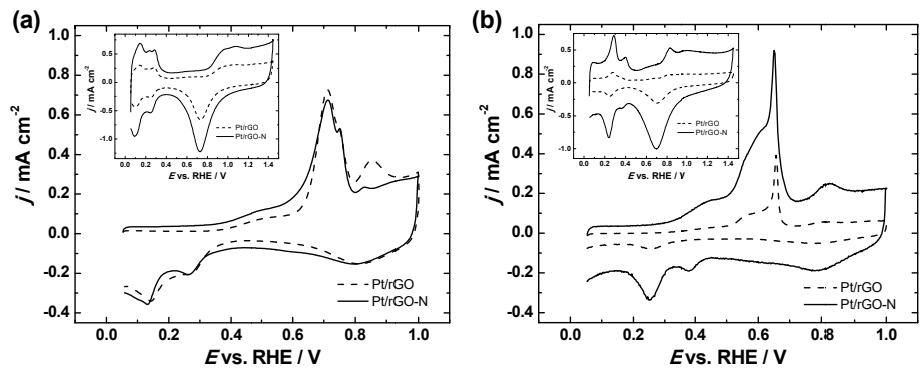

Figure 16. CO stripping voltammograms of Pt/rGO and Pt/rGO-N catalysts in 0.05 M H_2SO_4 (a) and 0.1 M KOH (b) solutions (v = 20 mV s^{-1}). The insets illustrate CV curves of the respective catalysts (v = 50 mV s^{-1}). The current densities are normalised to the geometric surface area of the electrode.

Cyclic voltammetry measurements were carried out in Ar-saturated 0.05 M H_2SO_4 (inset of Figure 16a) and 0.1 M KOH (inset of Figure 16b) solutions in the potential range of 0.05 to 1.45 V at 50 mV s^{-1}. Similar CV profiles of the Pt-based electrocatalysts have been reported earlier [15, 175]. Formation of the Pt surface oxides can be seen in the anodic sweep at a potential above 0.8 V in both media, which are reduced at ≈0.7 V in the cathodic sweep. The hydrogen desorption peaks at ≈0.14 and ≈0.27 V in acidic media and at ≈0.28 and ≈0.38 V in alkaline media correspond to the presence of (110) and (100) adsorption sites on the Pt surface. The Pt/rGO-N nanocatalyst exhibited broader peaks with higher current in the hydrogen adsorption/desorption region than the Pt/rGO. The real surface areas of the Pt catalysts (A_r) calculated from the hydrogen desorption peaks are given in Table 3. The double-layer capacitance for the Pt/rGO-N is larger than that for Pt/rGO, showing that the rGO-N support has higher surface area than rGO support. Increased specific surface area of the support material is influential for mass activity enhancement for Pt-based catalysts [82, 187].

6.3.3 ORR on Pt/rGO and Pt/rGO-N

Electrochemical reduction of oxygen was investigated in O_2-saturated 0.05 M H_2SO_4 and 0.1 M KOH solutions using the RDE method. The ORR measurements were performed for Pt/rGO and Pt/rGO-N catalysts at different electrode rotation rates. The number of electrons transferred per O_2 molecule was calculated using Eq. (9). It was revealed that the catalysts follow the typical 4-electron transfer pathway in both acidic and alkaline media. Figure 17a displays a comparison of the RDE polarisation curves measured at 1900 rpm in acidic media, while Figure 17b presents the ORR polarisation curves recorded in alkaline media. In comparison to commercial Pt/C catalyst in acid media, both Pt/rGO and Pt/rGO-N electrocatalysts showed relatively lower current density in the diffusion-limited region, indicating that the kinetic current is lower than that obtained for Pt/C. However, Pt/rGO-N exhibits higher current at mixed kinetic-diffusion control region (between 0.8 and 0.9 V) than commercial Pt/C. Moreover, in alkaline media Pt/rGO-N catalyst shows superior performance in terms of all the kinetic parameters for O_2 reduction mentioned above. The $E_{1/2}$ values were calculated from the RDE data and are presented in Table 3. It was observed that in acidic media, all the electrodes showed comparable $E_{1/2}$ values to that of the commercial Pt/C (≈0.85 V). In alkaline media, however, the highest $E_{1/2}$ value of 0.87 V was obtained for Pt/rGO-N catalyst. Introducing N into the nanocarbon structure plays an important role in determining the ORR performance. It has been reported previously, that pyridinic and/or graphitic N are actually responsible for the high ORR performance of N-doped carbon materials [183, 188].

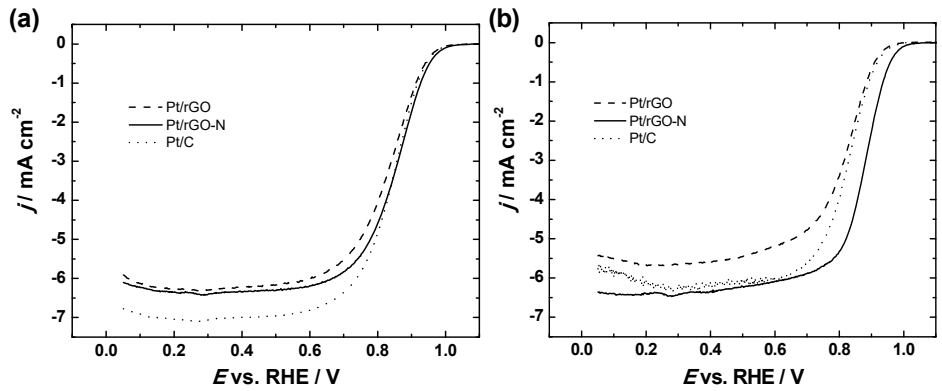

Figure 17. Comparison of the RDE polarisation curves for oxygen reduction on Pt/rGO, Pt/rGO-N and commercial Pt/C catalysts measured at 1900 rpm in O_2-saturated 0.05 M H_2SO_4 (a) and 0.1 M KOH (b) solutions.

Figure 18 presents Tafel plots constructed on the basis of the RDE data shown in Figure 17. Tafel slope values were determined from two characteristic Tafel regions and are listed in Table 3. It can be seen that the Tafel slope values for all the electrodes are close to -60 and -120 mV at low and high current densities, respectively, indicating that the O_2 reduction reaction follows the same mechanistic pathway for all the electrodes in both media. According to previous reports, the change of the slope is not related to different reaction mechanism, but it has been attributed to the potential-dependent coverage of surface oxides on Pt catalyst that inhibit the adsorption of O_2 and reaction intermediates [167]. Tafel analysis results indicate that the reaction mechanism was the same for Pt/rGO, Pt/rGO-N and commercial Pt/C electrocatalysts.

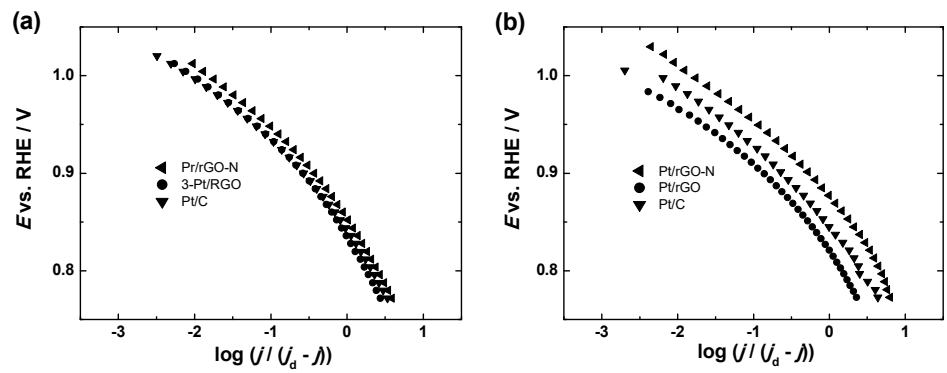

Figure 18. Tafel plots of Pt/rGO, Pt/rGO-N and Pt/C catalysts for ORR at 1900 rpm in 0.05 M H_2SO_4 (a) and 0.1 M KOH (b) solutions. Data derived from Figure 17.

Specific activities for O_2 reduction on the prepared catalysts were calculated using Eq. (10) and are given in Table 3. In general, all the electrodes showed higher SA than that of the commercial Pt/C. The highest SA value of 0.22 and 0.38 mA cm^{-2} in acidic and alkaline media, respectively, was obtained for Pt/rGO-N catalyst. The values of SA obtained for commercial Pt/C catalyst were 2 and 3 fold lower than those obtained for Pt/rGO-N catalyst in acid and alkaline media, respectively. The superior SA values of plasma jet treated catalyst materials are obviously related to the unique morphology and uniform distribution of Pt NPs, which is essential for enhancing the electrocatalytic ORR performance [63]. In addition, the enhanced ORR activity may be ascribed to the superior electrical conductivities of Pt/rGO-N composites. The RDE results clearly demonstrate that using one-step plasma-jet method in preparation of rGO-supported catalysts has a great effect on the activity of the supported metal nanoparticles.

Table 3. Kinetic parameters for oxygen reduction on Pt/rGO, Pt/rGO-N and commercial Pt/C catalysts in acid (0.05 M H_2SO_4) and alkaline (0.1 M KOH) media (ω=1900 rpm).

Electrode	A_r (cm^2)	Tafel slope (mV) lcd	Tafel slope (mV) hcd	$E_{1/2}$ (V)	SA at 0.9 V (mA cm^{-2})
Acid media					
Pt/rGO	0.71	-70	-155	0.84	0.20
Pt/rGO-N	1.24	-63	-121	0.85	0.22
Pt/C	1.67	-59	-125	0.84	0.13
Alkaline media					
Pt/rGO	0.22	-50	-119	0.82	0.36
Pt/rGO-N	1.01	-63	-129	0.87	0.38
Pt/C	1.11	-62	-107	0.85	0.11

6.4 Oxygen reduction on heat-treated Pt/MWCNT catalysts

6.4.1 Surface morphology of the heat-treated Pt/MWCNT

Figure 19a illustrates scanning electron micrograph of the acid-treated MWCNTs where nanotubes of various sizes and thicknesses can be observed. Figure 19b shows the SEM micrograph of Pt/MWCNT-RT. It can be observed that the nanotubes are finely covered with uniformly dispersed Pt NPs. SEM images of Pt/MWCNT catalysts annealed at different temperatures are presented in Figure 19c-f. No considerable change in the surface morphology of the Pt/MWCNT annealed at 300 ºC was observed (Figure 19c). The distribution of the Pt NPs is similar to that of the Pt/MWCNT-RT. However, the electrodes annealed at higher temperature ($T \geq$400 ºC) show different surface morphologies. For example, annealing the catalysts at 400 °C or higher temperature leads to the formation of two different size ranges of Pt particles. The size of smaller nanoparticles ranged from 5 to 15 nm while the larger ones had a diameter up to 120 nm. Agglomeration was first found in Pt/MWCNT-400 (Figure 1d). At higher annealing temperature much larger agglomerates were detected (Figure 1e-g). In general, there was no significant heat-treatment effect on the size of smaller nanoparticles at annealing temperatures of 400, 500 and 600 °C. However, remarkable effect on the morphology and size of larger nanoparticles was observed. Namely, the diameter of the larger nanoparticles increased steadily by increasing the annealing temperature and at the same time the coverage of MWCNTs by Pt decreased. By annealing at 400 °C the average size of the bigger nanoparticles ranged from 20 to 50 nm. At 500 °C the average size ranged from 40 to 50 nm, which further increased from 60 to 120 nm at 600 °C. Similar results obtained with annealed Pt-based materials have been also reported by other groups [189–193].

Concerning distribution density of the Pt NPs in the annealed sample one can see that the particles number density decreases in the depth direction of the coating, caused by the origin of the magnetron sputtering method. This is well observable by distribution of the bigger particles lying on the outermost layers of the Pt/MWCNT-x coatings, and showing that these layers already had a thicker Pt-coverage before the annealing. What is interesting that the number density of smaller Pt NPs seems to be more homogeneous in depth, and is somewhat bigger for coatings annealed at 500 °C if compared with other annealed coatings. It is probably connected with circumstances that Pt NPs are nucleating first on the defective sites of the nanotubes, and diffusion of Pt atoms from those sites needs to overcome some energy barrier.

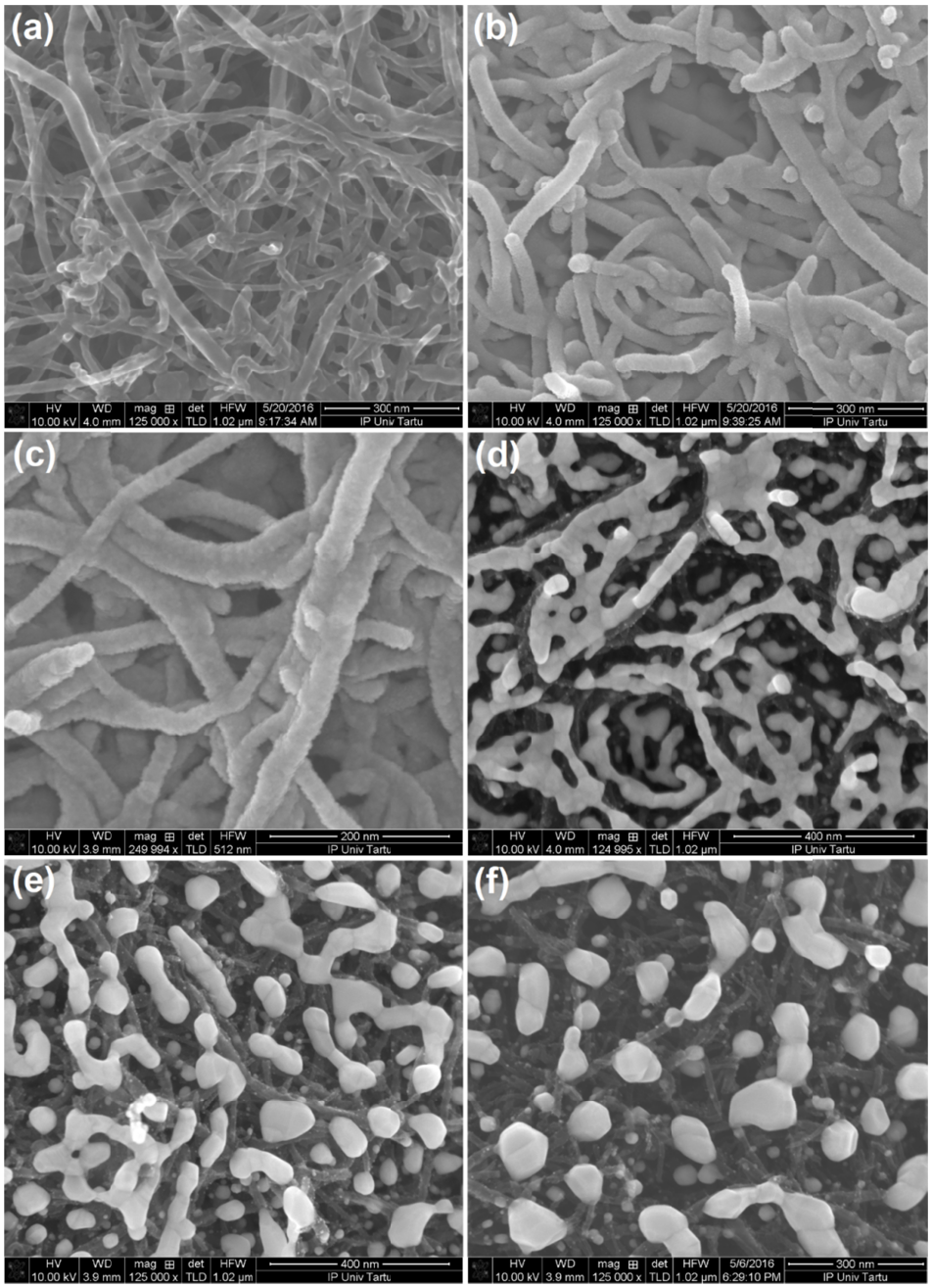

Figure 19. SEM images of acid-treated MWCNT (a), Pt/MWCNT-RT (b), Pt/MWCNT-300 (c), Pt/MWCNT-400 (d), Pt/MWCNT-500 (e) and Pt/MWCNT-600 samples (f).

6.4.2 Electrochemical characterisation of heat-treated Pt/MWCNT catalysts

Prior to the electrochemical characterisation of the catalyst surface by cyclic voltammetry, oxidative stripping of pre-adsorbed CO was performed in Ar-saturated 0.05 M H_2SO_4 solution to clean the electrode surface [160]. CO oxidation peaks were found in the potential range from 0.6 to 0.8 V for all Pt/MWCNT catalysts. However, different CO oxidation profiles were obtained that might be attributed to different Pt particle size and crystallographic facets as seen in Figure 19 [15, 174].

Following CO stripping, cyclic voltammograms were measured in Ar-saturated 0.1 M KOH and 0.05 M H_2SO_4 solutions at 50 mV s^{-1} in the potential range from 0.05 to 1.4 V. Figure 20 displays characteristics CVs for Pt-based electrocatalysts measured in both acidic (Figure 20a) and alkaline media (Figure 20b). In the low potential range from 0.05 to 0.4 V hydrogen adsorption and desorption peaks can be observed at the cathodic and anodic sweeps, respectively [46, 80, 84]. On the anodic sweep Pt surface oxides are formed above 0.8 V and are reduced at ~0.75 V in H_2SO_4 and at ~0.7 V in KOH on the cathodic sweep. It was observed that on Pt/MWCNT annealed at different temperatures, the peak corresponding to Pt(100) becomes more pronounced indicating the development of Pt(100) facets during annealing [194]. The real surface area of the MWCNT-supported Pt catalysts were calculated from the hydrogen desorption peaks [176]. Table 4 shows that Pt/MWCNT-300 catalyst has higher A_r than that of Pt/MWCNT-RT in both acidic and alkaline media. However, those annealed at higher temperatures showed a decrease in A_r due to increase in Pt particle size as observed in Figure 19. The decrease in A_r due to increase in particle size at elevated temperatures have been reported earlier [192, 193].

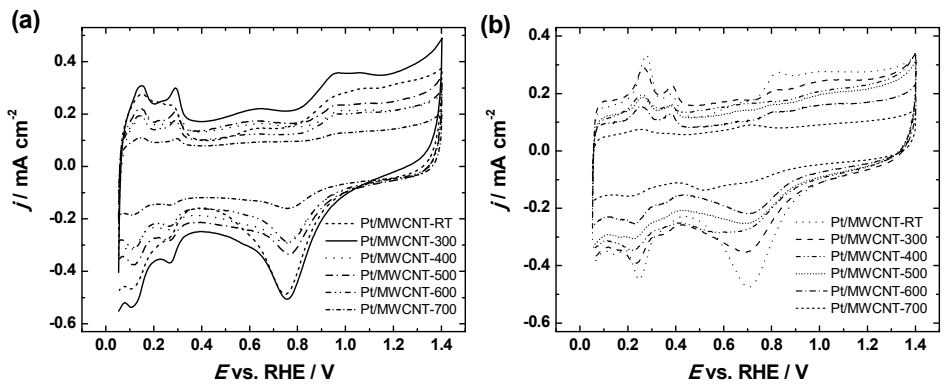

Figure 20. Cyclic voltammograms of Pt/MWCNT catalysts in Ar-saturated 0.05 M H_2SO_4 (a) and 0.1 M KOH (b) solutions at v = 50 mV s^{-1}.

6.4.3 ORR studies on Pt/MWCNT in alkaline medium

RDE measurements for oxygen reduction were first carried out in O_2-saturated 0.1 M KOH solution at a potential scan rate of 10 mV s^{-1}. The RDE results for all Pt/MWCNT-x electrodes measured at 960 rpm in comparison to commercial Pt/C are presented in Figure 21a. Table 6 shows the values of $E_{1/2}$ determined from the RDE results. The $E_{1/2}$ values of Pt/C, Pt/MWCNT-RT, bulk Pt and Pt/MWCNT-300 were close to each other. The electrodes annealed at temperature >300 ºC showed a decrease in the $E_{1/2}$ values, which is expected as the electroactive surface area decreased with increased temperature. The value of n calculated using Eq. (9) was close to 4 over the whole potential range studied, which indicates a typical 4-electron pathway of O_2 reduction on Pt surfaces as reported earlier [15, 128, 195].

In order to further analyse the ORR data, mass-transfer corrected Tafel plots were constructed for all the Pt/MWCNT-x electrodes as shown in Figure 21b. The Tafel slope value at low current densities was around -60 mV and the second slope at high current densities was close to -120 mV for all the electrodes studied (Table 4). These values indicate that the charge transfer is the rate-determining step for O_2 reduction on the Pt/MWCNT-x electrode surface. As the Tafel slope values obtained were similar for all the electrodes it can be concluded that the reaction mechanism is the same for all Pt/MWCNT-x catalysts. Similar Tafel slope values in alkaline medium have been reported earlier [15, 33, 42, 196]. The change in Tafel slope value has been suggested to arise from the change of oxygen adsorption conditions [42].

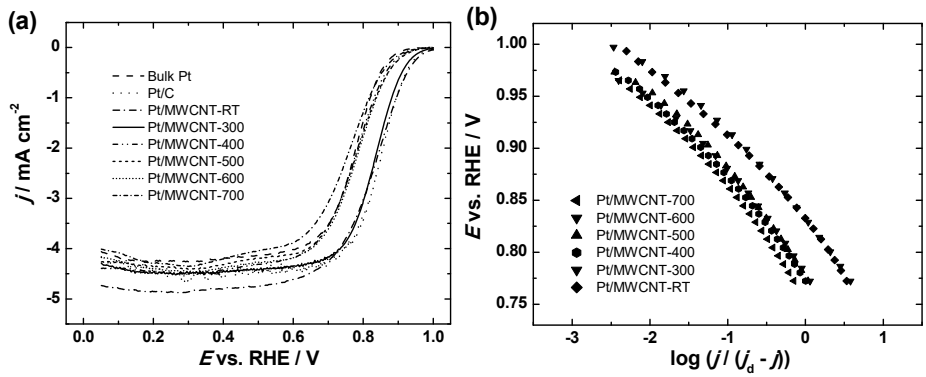

Figure 21. Comparison of RDE polarisation curves at 960 rpm in oxygen-saturated 0.1 M KOH solution. v = 10 mV s^{-1} (a) and Tafel plots for ORR (ω = 960 rpm) (b).

In order to compare intrinsic activities of the catalysts the specific activity and mass-activity (MA) of the ORR for all the Pt/MWCNT-x electrodes were determined. SA was calculated at 0.9 V using Eq. 10. As presented in Table 4, the SA of Pt/MWCNT-300 is higher than that of Pt/MWCNT-RT after which

the SA starts decreasing with increasing the annealing temperature. The higher SA of the catalyst annealed at 300 ºC suggests better utilisation of the Pt in the catalyst.

The mass-activity values were calculated at 0.9 V using the following equation:

$$MA = I_k / m_{Pt} \quad (11)$$

where m_{Pt} is the nominal mass of Pt in Pt/MWCNT composite materials. The mass activity of Pt/C is much higher than that of Pt/MWCNT-x modified electrodes. This can be attributed to the smaller size of Pt particles in commercial Pt/C as compared to Pt/MWCNT-x composites. It was observed that with increasing annealing temperature the MA values of the electrodes decreases, which can be attributed to the increase in particle size with increasing annealing temperature. Wang et al. observed, that annealing of Pt/CNTs in hydrogen atmosphere leads to noticeable agglomeration of the Pt NPs and subsequent decrease of the active Pt sites, leading to a decrease in the overall electrocatalytic performance in 1.0 M KOH [197].

Table 4. Kinetic parameters for ORR on Pt/MWCNT catalysts in 0.1 M KOH solution (ω=960 rpm).

Electrode	A_r (cm^2)	Tafel slope (mV) lcd	Tafel slope (mV) hcd	$E_{1/2}$ (V)	SA at 0.9 V (mA cm^{-2})	MA at 0.9 V (mA mg^{-1})
Pt/MWCNT-RT	0.29	-60	-118	0.82	0.23	16.9
Pt/MWCNT-300	0.41	-62	-110	0.83	0.38	20.1
Pt/MWCNT-400	0.23	-66	-114	0.76	0.17	5.8
Pt/MWCNT-500	0.27	-64	-118	0.77	0.17	6.8
Pt/MWCNT-600	0.30	-63	-116	0.77	0.13	6.1
Pt/MWCNT-700	0.15	-62	-117	0.72	0.19	3.9
Pt/C	1.09	-61	-115	0.84	0.10	38.1
Bulk Pt	0.32	-61	-110	0.82	0.30	

6.4.4 ORR studies on Pt/MWCNT in acid medium

The electrochemical reduction of O_2 was also studied in 0.05 M H_2SO_4 solution. The number of electrons transferred per O_2 molecule was calculated using Eq. (9), confirmed the 4-electron pathway of the O_2 reduction reaction, which is in agreement with previous work [193]. The RDE results of Pt/MWCNT-x were compared with Pt/C as shown in Figure 22a. The $E_{1/2}$ values (Table 5) are close to those obtained in 0.1 M KOH. It was found that with increasing annealing temperature the $E_{1/2}$ values decrease in the following order: Pt/C > Pt/MWCNT-RT ≈ Pt/MWCNT-300 ≈ bulk Pt > Pt/MWCNT-400 ≈ Pt/MWCNT-500 ≈

Pt/MWCNT-600 > Pt/MWCNT-700. Tafel plots constructed on the basis of the RDE polarisation data are presented in Figure 22b, the slope values are given in Table 5. It can be seen that the Tafel slope values determined at low current densities are little bit higher than those in the alkaline medium, but they are still close to the previously reported value of -60 mV. An increase in the slope values at low current densities was observed with increasing annealing temperature. Tafel slope values at high current densities were close to -120 mV. Tafel slope values confirm that the first electron transfer to the adsorbed O_2 molecule is the rate-determining step.

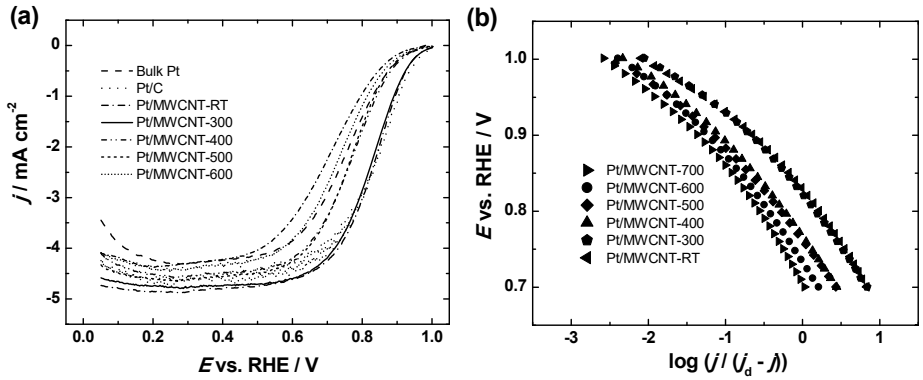

Figure 22. Comparison of RDE polarisation curves at 960 rpm in O_2-saturated 0.05 M H_2SO_4 solution (v = 10 mV s^{-1}) (a) and Tafel plots (b) for the ORR.

Specific activity of the Pt/MWCNT-x catalysts calculated at 0.9 V (using Eq. 10), were close to those observed in 0.1 M KOH and almost the same trend of decreasing the SA values with increasing annealing temperature was observed (Table 5). Su et al. reported that the ORR activity of Pt nanowires decreases as the annealing temperature is increased from 200 to 600 ºC [198]. MA values calculated from Eq. (11) are also presented in Table 5. Pt/C showed the maximum MA as compared to Pt/MWCNT electrodes. The MA decreased with increasing annealing temperature as in the case of alkaline medium. In general, a decrease of the catalyst electrochemically active area and mass activity is observed with increasing particle size. The number density of the catalyst particles also plays an important role. When Pt particles are well separated from each other, the full particle surface is active for ORR. When Pt particles are close, they have so called mutual influence on the diffusion layer and negative effect on the catalytic activity, since the whole catalyst area is not available [199]. Platinum nanocrystals supported on CNTs annealed at 300 ºC in 20% H_2–80% Ar atmosphere showed the highest specific surface area value (39.57 m^2 g^{-1}) and a better electrocatalytic activity toward the ORR in 0.1 M H_2SO_4 [193]. Bezerra et al. reviewed the heat-treatment effects of fuel cell catalysts and summarised that the optimum annealing procedure regarding the ORR activity

improvement depends on the individual catalyst [200]. However, too high annealing temperature (>1000 ºC) degrades the electrocatalyst activity. Chung et al. proposed that the ORR activity is mainly influenced by the degree of catalyst surface atom rearrangement, such as by increasing the amount of Pt(111) facets, not the change of surface oxide [192]. Same observation was made by Su et al., after heat-treatment the Pt nanowires had more Pt(111) sites on the catalyst surface and exhibited better electrocatalytic activity toward the ORR in acid electrolyte [198]. Several groups reported that by changing the particle size, surface coordination number and distribution of the surface atoms is changed that results in a change of the ORR activity [201–203]. However, there is no clear agreement in the literature regarding particle size effect on the ORR activity of Pt/C catalysts [200]. Shinozaki et al. studied particle size effect on the ORR using polycrystalline Pt and commercial Pt/C in 0.1 M $HClO_4$ [204]. They reported an increase in the SA values with increasing the average Pt/C particle size in the range of 2.1–9.9 nm. Anastasopoulos et al. compared particle size dependence of Pt and Pd for the ORR in 0.5 M $HClO_4$ [31]. They observed an increased specific current density for Pt NPs from 1.5 up to 4 nm in diameter. The MA maximum was observed from 3.5 to 4 nm. These results are in good agreement with the previous results [201, 205, 206]. Maximum MA of Pt NPs in 0.1 M $HClO_4$ with an average diameter of 3 nm has also been reported [207]. Gasteiger and co-workers reported that in case of PEMFC, the variation of mass activity and specific activity with particle size is due to the adsorption of oxygen-containing species [180]. The aspects regarding particle size are highly important in the practical design of Pt-based cathode catalysts for low-temperature fuel cells.

Table 5. Kinetic parameters for the ORR on Pt/MWCNT catalysts in 0.05 M H_2SO_4 (ω=960 rpm).

Electrode	A_r (cm^2)	Tafel slope (mV) lcd	Tafel slope (mV) hcd	$E_{1/2}$ (V)	SA at 0.9 V (mA cm^{-2})	MA at 0.9 V (mA mg^{-1})
Pt/MWCNT-RT	0.45	-62	-119	0.82	0.26	26.7
Pt/MWCNT-300	0.46	-66	-120	0.81	0.32	22.6
Pt/MWCNT-400	0.21	-72	-125	0.75	0.29	9.7
Pt/MWCNT-500	0.29	-66	-115	0.74	0.15	6.6
Pt/MWCNT-600	0.28	-73	-119	0.73	0.15	6.7
Pt/MWCNT-700	0.13	-86	-122	0.69	0.15	3.3
Commercial Pt/C	1.42	-71	-139	0.84	0.12	70.1
Bulk Pt	0.40	-91	-121	0.80	0.39	-

6.5 Oxygen reduction on Pt-TiO_2/MWCNT catalysts in acid media

6.5.1 Surface morphology of the Pt-TiO_2/MWCNT

Surface morphology of TiO_2/MWCNT and Pt-TiO_2/MWCNT modified GC electrodes was examined by SEM as presented in Figure 23. Figure 23a displays MWCNTs uniformly coated with TiO_2 (35 ALD cycles) while 2Pt-35TiO_2/MWCNT, 4Pt-35TiO_2/MWCNT, 8Pt-35TiO_2/MWCNT, 8Pt-50-TiO_2/MWCNT and 12Pt-35TiO_2/MWCNT are presented in Figure 23b-f, respectively. It can be observed that TiO_2 decorated MWCNTs are uniformly coated with Pt NPs. Similar uniform distribution of Pt NPs on acid-treated MWCNTs using magnetron sputtering technique has been observed previously [IV]. Moreover, it was found that the surface morphology of the electrodes is changed by varying the amount of Pt and TiO_2.

Figure 24 displays HAADF-STEM images of 35TiO_2/MWCNT (a) and 2Pt-35TiO_2/MWCNT (b). It can be observed in that the TiO_2 is deposited onto the carbon nanotube surface as separate islands that in some regions are connected forming a well-dispersed network-type coating (Figure 24a). Thus the deposited titania layer can be a good inhibitor to the carbon corrosion during the electrochemical process. Some groups have previously reported carbon corrosion inhibition with TiO_2 coating [132, 208]. In accordance with the SEM results for similar material (Figure 23b), HAADF-STEM results (Figure 24b) clearly indicate that sputter-deposition of the Pt NPs on the TiO_2/MWCNT composite results into a granular coating of the composite support (Figure 24b). Elemental mapping (shown in insets of Figures 24a and 24b) demonstrate uniform distribution of Pt and TiO_2 over the surface of carbon nanotubes.

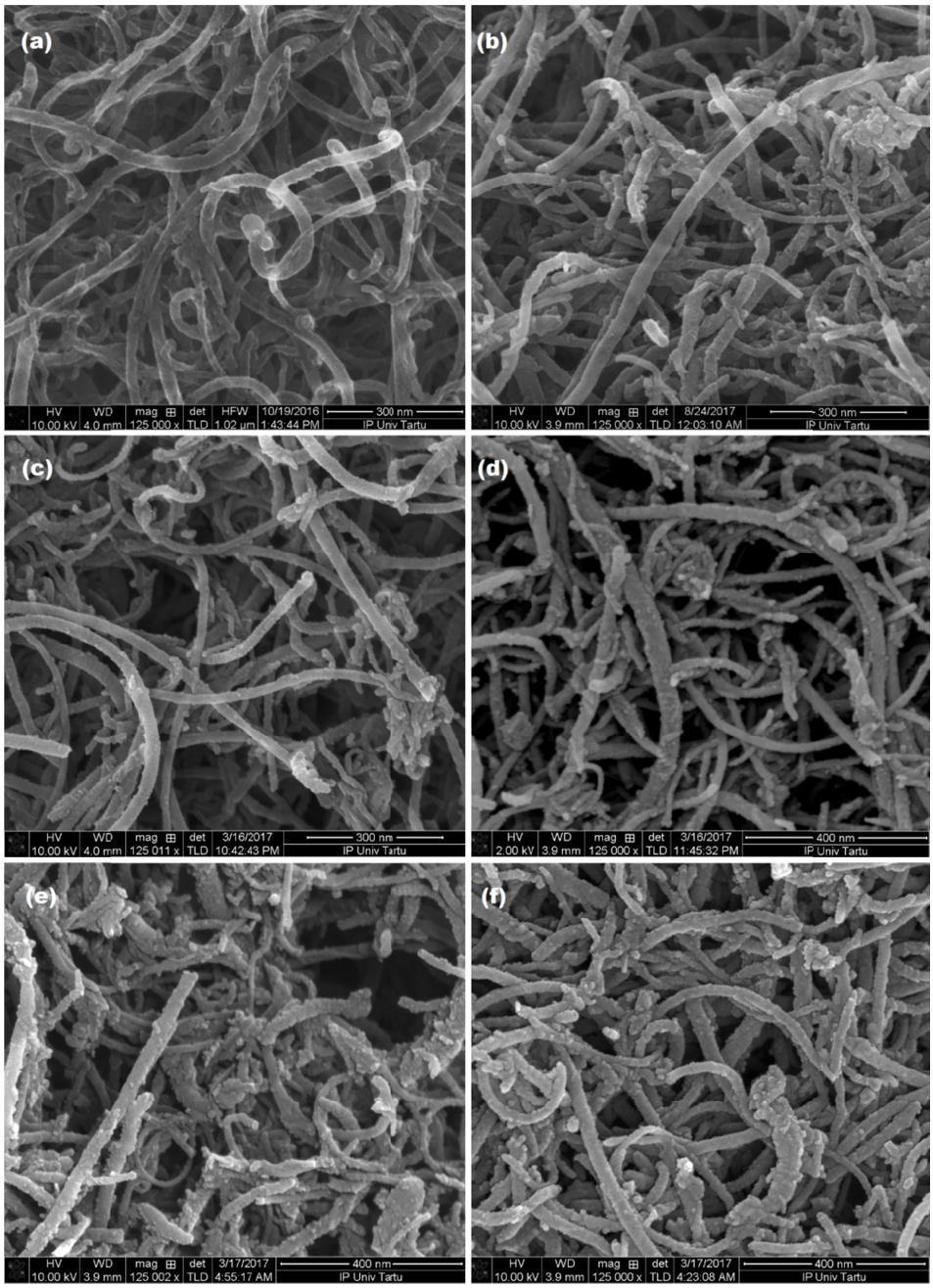

Figure 23. SEM images of TiO_2/MWCNT (a), 2Pt-35TiO_2/MWCNT (b), 4Pt-35TiO_2/MWCNT (c), 8Pt-35TiO_2/MWCNT (d), 8Pt- 50TiO_2/MWCNT (e) and 12Pt-35TiO_2/MWCNT (f) samples.

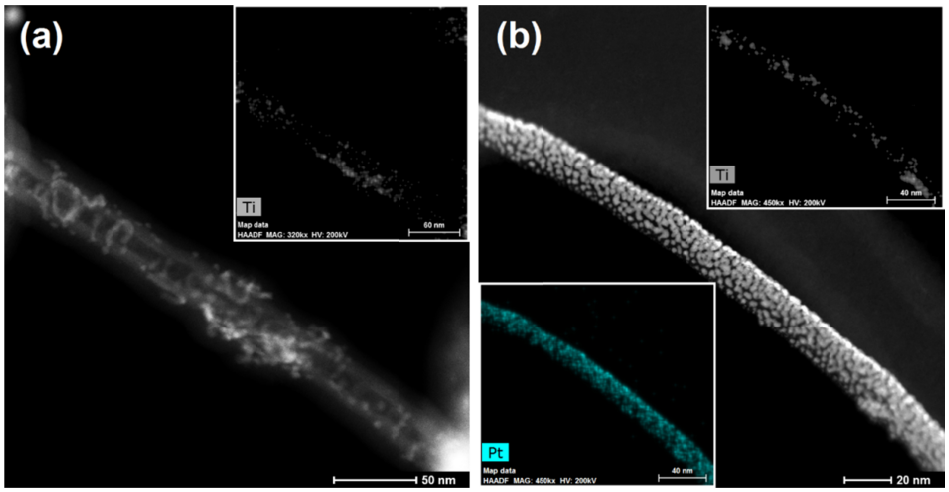

Figure 24. HAADF-STEM images of $35TiO_2$/MWCNT (a) and 2Pt-$35TiO_2$/MWCNT (b). Insets in the Figures show elemental map of Pt and Ti.

XPS survey spectra shows the C1s peak at 284 eV, O1s peak at 531 eV, Ti2p peak at 458 eV, Pt4f peaks at 73 and 76 eV, Pt4d peaks at 314 and 331 eV and Pt4p peak at 519 eV (Figure 25). Insets in the Figure 25 present the XPS core-level spectra in the Ti2p and Pt4f regions, respectively. As expected, all Ti is in an oxidised form (Ti^{4+}) that indicates the formation of TiO_2 by ALD. The XPS peak of $Ti2p_{3/2}$ centred at 458.7 eV is in agreement with our previous studies on Pt-TiO_2 catalysts [209]. High-resolution XPS spectrum in the Pt4f region shows that Pt is mainly in the zero-valence (metallic) state.

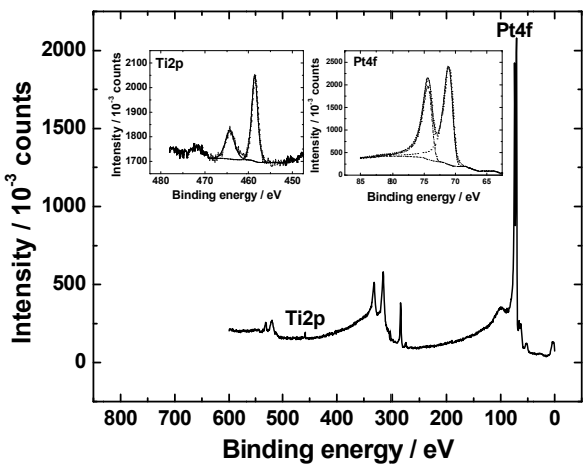

Figure 25. XPS wide scan spectra of a 2Pt-$35TiO_2$/MWCNT catalyst, the insets show core-level spectra in the Ti 2p and Pt 4f regions.

6.5.2 Electrochemical characterisation of Pt-TiO_2/MWCNT

Figure 26a displays CO electro-oxidation voltammograms measured for all Pt-TiO_2/MWCNT electrocatalysts. It was revealed that all catalysts follow similar CO oxidation behaviour. All the electrodes showed a broad peak at 0.7 V, a less pronounced peak at 0.75 V and a shoulder at 0.8 V. The difference in the peak current densities can be ascribed to the different Pt loading. Influence of the size, shape and dispersion of the Pt NPs on the electro-oxidation of CO monolayer has been demonstrated earlier [194, 210]. After electrochemical decontamination of the electrode surface, CV curves were recorded in Ar-saturated 0.05 M H_2SO_4 solution (Figure 26b). A stable CV was obtained for each electrode after measuring five successive potential cycles. For all the Pt-TiO_2/MWCNT catalysts studied, the CV curves represent the typical polycrystalline Pt features. For comparison, CV curve for Pt-free 35TiO_2/MWCNT with no significant features is also shown in Figure 26b. As can be seen from the CV results, the double-layer contribution for different TiO_2 layer thicknesses of 8Pt-35TiO_2/MWCNT and 8Pt-50TiO_2/MWCNT remains practically the same and the CV curves look very similar. The real surface area of the Pt catalysts were calculated from the hydrogen desorption peaks [176] as 0.09, 0.23, 0.33, 0.33, 0.42 cm^2 for 2Pt-35TiO_2/MWCNT, 4Pt-35TiO_2/MWCNT, 8Pt-35TiO_2/MWCNT, 8Pt-50TiO_2/MWCNT and 12Pt-35TiO_2/MWCNT, respectively. The differences in the real surface areas of the catalysts are well-reflected in the different CO_{ad} oxidation peak currents and peak charges. The slight down-shift of CO_{ads} peak maxima for electrodes with higher Pt loading may be due to the electronic effects caused by metal-support interactions [112].

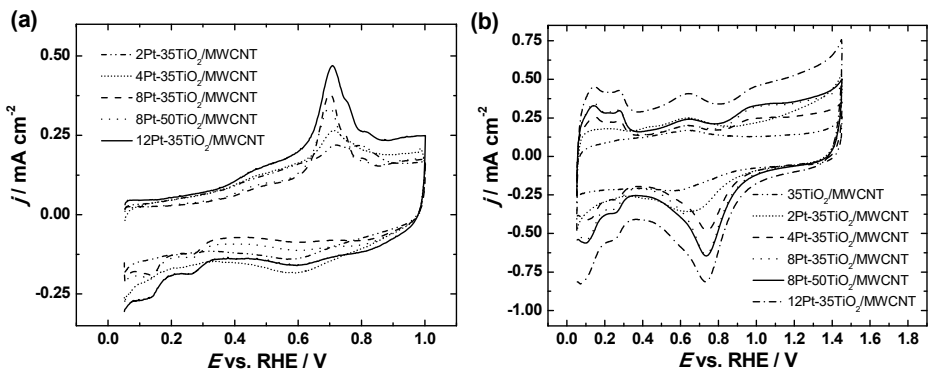

Figure 26. CO stripping voltammograms of various Pt-TiO_2/MWCNT catalysts in Ar-saturated 0.05 M H_2SO_4 solution measured at 20 mV s^{-1} (a) and cyclic voltammograms of the respective catalysts measured at 50 mV s^{-1} (b).

6.5.3 ORR studies on Pt-TiO_2/MWCNT in acid media

The electrochemical reduction of oxygen was investigated at various electrode rotation speed (360–4600 rpm) in O_2-saturated 0.05 M H_2SO_4 in the potential range of 0.05–1.1 V at a scan rate of 10 mV s^{-1} using RDE. The number of electrons transferred per O_2 molecule, calculated from the RDE data using Eq. (9) was close to four that revealed the 4-electron pathway of the O_2 reduction reaction. The 4-electron ORR pathway is extremely important for PEM fuel cell cathode catalysts, since H_2O_2 formed in case of competing 2-electron ORR pathway is very corrosive towards the membrane-electrode assembly. It is still unclear whether intermediate formation of hydrogen peroxide takes place or not, but according to earlier investigations using the rotating ring-disk electrode technique it has been reported that peroxide formation is less than 1% in the potential range of 0.6–0.8 V vs RHE [65].

A comparison of the RDE polarisation curves of the Pt-TiO_2/MWCNT catalysts, along with commercial Pt/C catalyst, measured at 1900 rpm, is shown in Figure 27a. The onset of cathodic oxygen reduction current is shifted positively with an increase in Pt loading in composite material and it is basically due to an increase in the total amount of electroactive Pt. It was found that in case of 2Pt-35TiO_2/MWCNT and 4Pt-35TiO_2/MWCNT, the $E_{1/2}$ value is considerably lower than that of commercial Pt/C while on the other hand, 8Pt-35TiO_2/MWCNT, 8Pt-50TiO_2/MWCNT and 12Pt-35TiO_2/MWCNT showed similar $E_{1/2}$ to that of the commercial Pt/C (Table 6). Similar results were obtained by Huang et al., as the mass loading of Pt increased with increasing Pt deposition time, the onset potential shifted positively [211]. The ORR onset potential (E_{onset}) values determined from the RDE data are also presented in Table 6 which are in line with the $E_{1/2}$ values. Figure 27b illustrates mass-transfer corrected Tafel plots for Pt-TiO_2/MWCNT electrodes in comparison to commercial Pt/C. Tafel slope values calculated for all Pt-based electrodes were close to –60 and –120 mV at low current densities and high current densities, respectively (Table 6), which confirms that the transfer of the first electron to the O_2 molecule is the rate-determining step.

Specific activity of the Pt-TiO_2/MWCNT and Pt/C catalysts, calculated at 0.9 V (using Eq. (10)) are listed in Table 8. It was observed that all the Pt-TiO_2/MWCNT catalysts showed higher SA than that of the commercial Pt/C. The maximum SA of 0.57 mA cm^{-2} is shown by 2Pt-35TiO_2/MWCNT while lowest value was shown by 4Pt-35TiO_2/MWCNT (0.37 mA cm^{-2}). In the case of 8Pt-35TiO_2/MWCNT and 8Pt-50TiO_2/MWCNT the specific activities are 0.47 and 0.45 mA cm^{-2}, respectively.

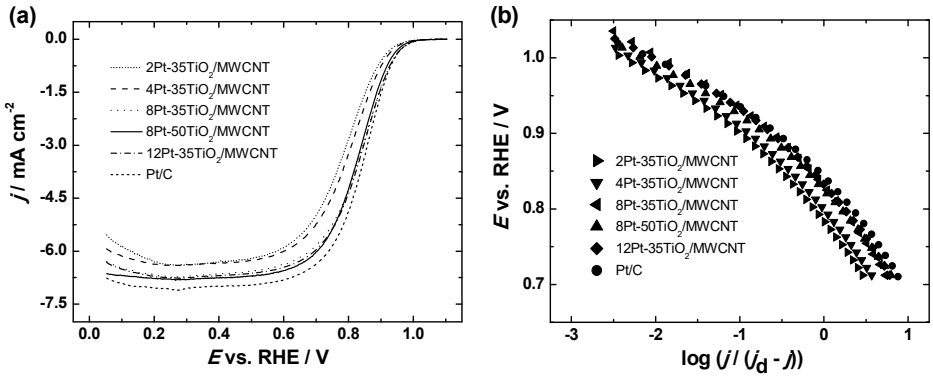

Figure 27. RDE polarisation curves for O_2 reduction on Pt-TiO_2/MWCNT and commercial Pt/C catalysts measured at 1900 rpm in O_2-saturated 0.05 M H_2SO_4 solution (v = 10 mV s^{-1}) (a) and Tafel plots for ORR on the respective catalysts (b).

A slight decrease in the SA (0.39 mA cm^{-2}) was observed for 12Pt-35TiO_2-/MWCNT. Huang and co-workers studied the ORR kinetics on Pt nanoparticles electrodeposited into nanocrystalline mesoporous TiO_2 thin films and similarly, they observed the decrease in electrocatalytic activity with increasing the Pt electrodeposition time [211]. According to Lewara et al., the increased electronic density on Pt, due to the metal-support interaction increases the ORR activity of the Pt catalyst supported on TiO_2 coated carbon materials [105].

The mass activities of the prepared catalysts were calculated using Eq. (11). Mass activities of the Pt-TiO_2/MWCNT catalysts along with the commercial Pt/C, calculated at 0.9 V are given in Table 6. Like SA, the maximum MA (118 mA mg^{-1}) is shown by 2Pt-35TiO_2/MWCNT, which can be ascribed to the uniform dispersion of the Pt NPs on the TiO_2/MWCNT support. Similarly, 4Pt-35TiO_2/MWCNT also showed higher MA (92 mA mg^{-1}) than that of the commercial Pt/C (84 mA mg^{-1}). The mass activities of 8Pt-35TiO_2/MWCNT and 8Pt-50TiO_2/MWCNT are 67 mA mg^{-1} and 65 mA mg^{-1}, respectively, which are lower than that of Pt/C. Further decrease in the MA was observed in the case of 12Pt-35TiO_2/MWCNT (52 mA mg^{-1}). The decrease in MA with increasing Pt loading is in accordance with previous studies [211] and it indicated the low accessibility of oxygen to the electroactive Pt surface.

Table 6. Kinetic parameters for the ORR on Pt-TiO_2/MWCNT catalysts in 0.05 M H_2SO_4 solution (ω=960 rpm).

Electrode	A_r (cm^2)	Tafel slope (mV) lcd	Tafel slope (mV) hcd	E_{onset} (V)	$E_{1/2}$ (V)	SA at 0.9 V (mA cm^{-2})	MA at 0.9 V (A g^{-1})
2Pt-35TiO_2/MWCNT	0.09 ± 0.01	-62 ± 3	-133 ± 7	0.92 ± 0.01	0.75 ± 0.03	0.57 ± 0.08	118 ± 8
4Pt-35TiO_2/MWCNT	0.23 ± 0.02	-63 ± 5	-128 ± 9	0.94 ± 0.01	0.78 ± 0.03	0.37 ± 0.05	92 ± 1
8Pt-35TiO_2/MWCNT	0.33 ± 0.02	-61 ± 6	-126 ± 9	0.95 ± 0.01	0.83 ± 0.01	0.47 ± 0.07	67 ± 2
8Pt-50TiO_2/MWCNT	0.33 ± 0.01	-61 ± 2	-121 ± 4	0.95 ± 0.01	0.82 ± 0.01	0.45 ± 0.04	65 ± 2
12Pt-35TiO_2/MWCNT	0.42 ± 0.05	-61 ± 2	-126 ± 3	0.96 ± 0.01	0.83 ± 0.01	0.39 ± 0.03	52 ± 9
Commercial Pt/C	1.65 ± 0.04	-62 ± 4	-127 ± 5	0.95 ± 0.01	0.84 ± 0.01	0.14 ± 0.02	84 ± 2

6.5.4 Long-term durability of Pt-TiO_2/MWCNT

In order to investigate the durability of the Pt-TiO_2/MWCNT catalysts and its dependence on the loading of Pt and/or TiO_2, 1000 repetitive potential cycles were performed for all Pt-TiO_2/MWCNT catalysts in the potential range from 0.05 to 1.2 V at 50 mV s^{-1}. Figure 28a illustrates a comparison of the RDE polarisation curves measured at 1900 rpm before and after the ADT. It can be seen that there is no significant change in the half-wave potential before and after the ADT revealing that the prepared 8Pt-35TiO_2/MWCNT catalyst retains its electrocatalytic activity after the durability measurements.

A comparison of the percent loss in the surface area of the catalysts during the stability test is shown in Figure 28b. It was observed that Pt-TiO_2/MWCNT catalysts are more resistant to degradation than commercial Pt/C, retaining up to 95% (8Pt-50TiO_2/MWCNT) of the catalyst surface area after the ADT. Superior long-term durability of the prepared catalysts is attributed to the higher corrosion resistant property of TiO_2/MWCNT composite in comparison to Vulcan carbon induced by the SMSI between Pt and the metal oxide [208, 211–213]. The SMSI in Pt-TiO_2 system, according to Alonso-Vante and Luo, is the modification in the electronic structure of the Pt catalyst as result of the interaction between the two metals (Pt and Ti) [108]. The modification can be due to alloy formation and/or charge transfer from the metal oxide to the catalytic metal. Comparison of the real surface area change during long-term potential cycling (Figure 28b) indicates significance of the TiO_2/MWCNT support. Considering the importance of the durability of fuel cell catalysts in harsh environments, Pt-TiO_2/MWCNT is a promising catalyst for PEM fuel cells.

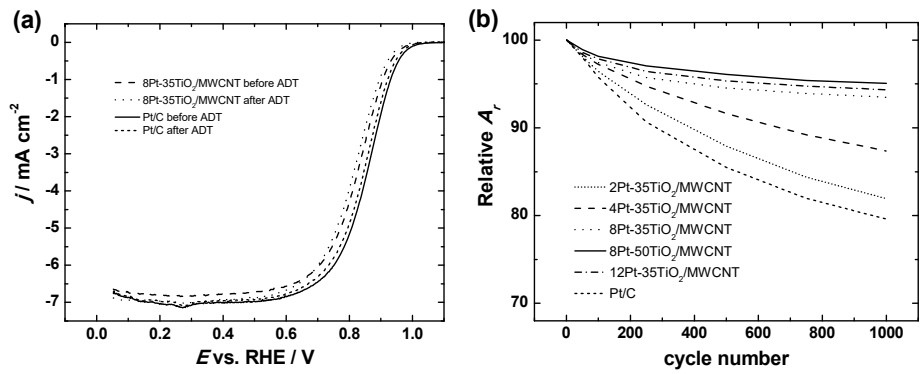

Figure 28. RDE polarisation curves of 8Pt-35TiO_2/CNT and commercial Pt/C in O_2-saturated 0.05 M H_2SO_4 solution at 1900 rpm before and after the ADT (v = 10 mV s^{-1}) (a) and relative loss in the real surface areas during ADT (b).

6.6 Oxygen reduction on Pt-TiO_2/MWCNT catalysts in alkaline media

6.6.1 Surface morphology of the Pt-TiO_2/MWCNT

Surface morphology of the platinum nanoparticles sputter-deposited on TiO_2 coated MWCNT has been investigated earlier in sub-section 6.5.1 (Figure 23). It was observed that the Pt NPs are uniformly distributed on the surface of TiO_2/MWCNT composite support. In the present work we compared the surface morphology, electrocatalytic activity and durability of the Pt NPs sputter-deposited on TiO_2/MWCNT to that of the Pt NPs photo-deposited on the same support. Carbon nanotubes were decorated with TiO_2 using ALD as presented in Figure 23a. Figure 29 shows HAADF-STEM image of 4Pt-35TiO_2/CNT and $Pt_{(PD)}$-35TiO_2/CNT catalysts. It is seen that the nanotubes are fully covered with titania ALD film having Pt NPs on it. The elemental mappings given in the same image clearly show distribution of the Pt nanoparticles and uniform TiO_2 coating on the surface of MWCNTs. It should be noted that relatively tightly lying particles of Pt metal absorb part of Ti K_α radiation generated by probe electrons in the underlying TiO_2 film. For that reason, the X-ray signal of Ti is less intense as it would be without Pt addition. Moreover, it is observed that magnetron sputtering results in uniform distribution of Pt NPs on the TiO_2 coated MWCNTs, while photo-deposition leads to the formation of smaller agglomerates at the support surface as seen in SEM analysis. This can be attributed to the selective deposition of the Pt NPs and the anchoring mechanism of photo-deposition where metal oxide acts as nucleation site for the deposition of Pt nanoparticles.

Surface composition of the prepared catalysts and chemical states of Pt and Ti were investigated by the XPS analysis. The XPS survey spectrum of $Pt_{(PD)}$-35TiO_2/CNT catalyst is presented in Figure 30. The Pt 4f and Ti 2p deconvoluted XPS peaks are shown in the insets. The peak centred at 71.0 eV corresponds to Pt^0 $4f_{7/2}$ and that at 74.5 eV Pt^{4+} $4f_{7/2}$ indicating that platinum mainly exists in two oxidation states. XPS results for Pt sputter-deposited on TiO_2/CNT composite have been presented earlier (Figure 25).

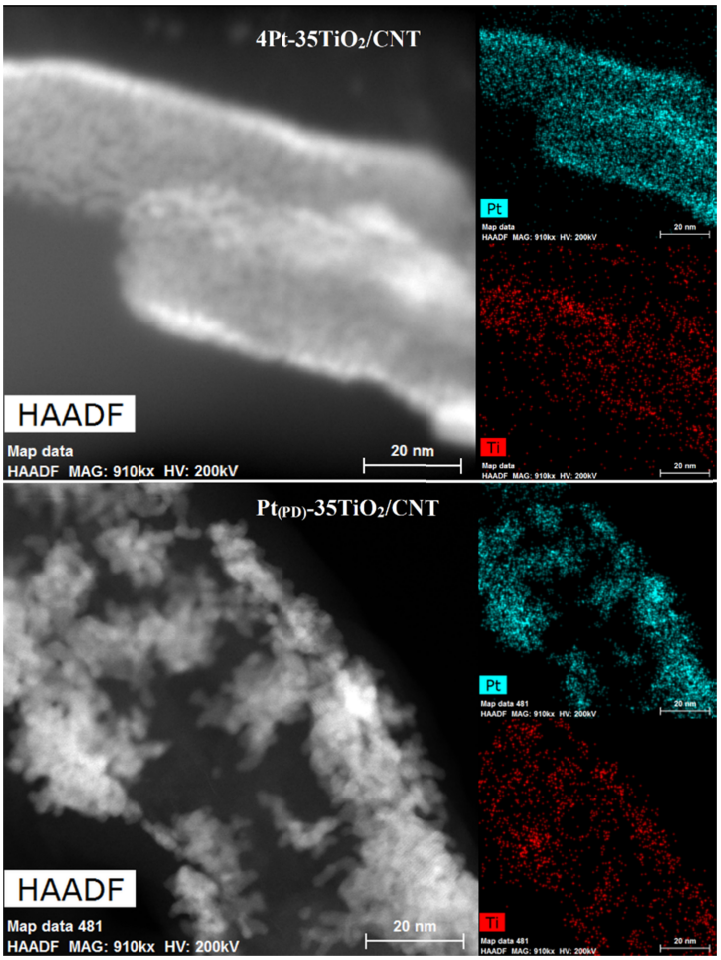

Figure 29. HAADF-STEM images of 4Pt-35TiO_2/CNT and $Pt_{(PD)}$-35TiO_2/CNT samples with corresponding elemental mappings of Pt and Ti.

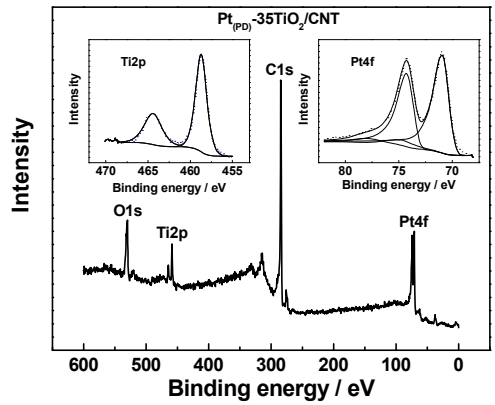

Figure 30. XPS spectra of $Pt_{(PD)}$-35TiO_2/CNT catalyst. The inset show deconvoluted peaks of Pt 4f and Ti 2p.

6.6.2 Electrochemical characterisation of Pt-TiO_2/MWCNT

Further characterisation of the electrodes surface was carried out by CO stripping and cyclic voltammetry in 0.1 M KOH solution. As demonstrated in Figure 31a, all prepared catalysts show similar CO stripping profile with an onset potential of 0.38 V. The main CO oxidation peak is located at 0.67 V with a shoulder centred at ~0.58 V. CO oxidation profile of Pt-based catalysts is an important tool for evaluation of the SMSI at the interface. For instance, the CO oxidation main peaks on 8Pt-35TiO_2/CNT, 8Pt-50TiO_2/CNT and $Pt_{(PD)}$-35TiO_2/CNT are located at 0.67, 0.66 and 0.65 V, respectively. The negative shift in the CO oxidation peaks corresponds to the relative strength of metal-support interaction at the interface [119]. Comparing CO stripping peak potentials of 8Pt-35TiO_2/CNT to 8Pt-50TiO_2/CNT indicates that the thickness of TiO_2 coating with respect to Pt loading plays a significant role in the metal-support interaction. Further negative shift for $Pt_{(PD)}$-35TiO_2/CNT indicates relatively stronger metal-support interaction that can be attributed to the anchoring mechanism of Pt NPs to the oxide-carbon composite. The pre-peak at approximately 0.5 V observed at relatively higher Pt loading can be attributed to agglomeration of the nanoparticles [183]. The difference in the peaks height is ascribed to the different Pt loading and surface morphology of the catalysts.

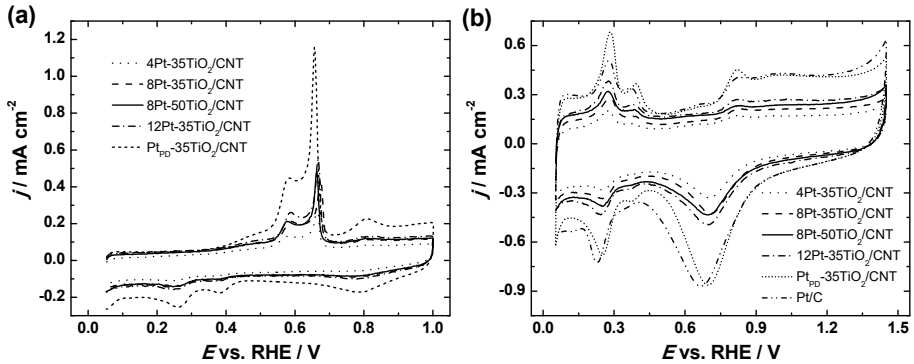

Figure 31. CO stripping profiles of Pt-TiO_2/CNT catalysts in Ar-saturated 0.1 M KOH solution (v = 20 mV s^{-1}) (a) and cyclic voltammograms of the respective catalysts in comparison to commercial Pt/C (v = 50 mV s^{-1}) (b).

Figure 31b illustrates the stable cyclic voltammograms recorded in 0.1 M KOH solution after conditioning the electrode surface by CO stripping. The real surface area of the Pt catalyst was determined from the hydrogen desorption peaks [214]. As presented in Table 7, the highest A_r value of 1.06 cm^2 is shown by Pt photo-deposited on 35TiO_2/CNT (PD). However, catalysts prepared by magnetron sputtering showed much smaller surface areas, which may be due to the compact deposition of Pt nanoparticles on the support surface as observed in Figures 23b-f, 24 and 29. For example, 4Pt-35TiO_2/CNT catalyst had the lowest value of A_r (0.18 cm^2) attributed to the relatively low Pt loading. Expectedly, the 8Pt-35TiO_2/CNT and 8Pt-50TiO_2/CNT catalysts had nearly the same A_r values of 0.31 and 0.32 cm^2, respectively. A slight increase was observed for 12Pt-35TiO_2/CNT (A_r = 0.37 cm^2). Commercial Pt/C (20 wt.%) catalyst showed a higher surface area of Pt (A_r = 0.86 cm^2).

6.6.3 ORR studies on Pt-TiO_2/MWCNT in alkaline media

To investigate the electrocatalytic ORR behaviour of the TiO_2/CNT supported Pt catalysts in alkaline media, the RDE measurements were carried out in O_2-saturated 0.1 M KOH solution. The number of electrons calculated by Eq. (9) was found close to four revealing that the catalyst followed a typical 4-electron pathway for the whole range of potentials studied. This is in a good agreement with the previous results [81, 122]. Figure 32a displays the RDE polarisation curves (ω=1900 rpm) of all the prepared catalysts in comparison to that of the commercial Pt/C (20 wt%). The $E_{1/2}$ values, for all the electrodes were determined and are summarised in Table 7. The highest $E_{1/2}$ value of 0.86 V is shown by $Pt_{(PD)}$-35TiO_2/CNT. In the case of sputter-deposited Pt, 12Pt-35TiO_2/CNT showed similar $E_{1/2}$ value to that of commercial Pt/C (0.84 V). However, 4Pt-35TiO_2/CNT, 8Pt-35TiO_2/CNT and 8Pt-50TiO_2/CNT catalysts showed relati-

vely lower $E_{1/2}$ of 0.80±0.10 V. The highest ORR activity of $Pt_{(PD)}$-35TiO_2/CNT can be attributed to the increased electronic cloud on the catalytic centre as a result of SMSI [105]. It has been observed earlier that the interfacial interaction between the Ti atoms and the supported Pt catalyst in Pt/TiO_2 system increases electronic density on the catalyst, which results into improved ORR activity [105, 108]. Hwang and co-workers have also revealed changes in electronic structure of the Pt catalyst as a result of synergistic interaction with $Ti_{0.7}Mo_{0.3}O_2$ support [215]. Moreover, the ORR activity of 8Pt-50TiO_2/CNT is moderately higher than that of the 8Pt-35TiO_2/CNT counterpart, which further justifies the metal-support interaction.

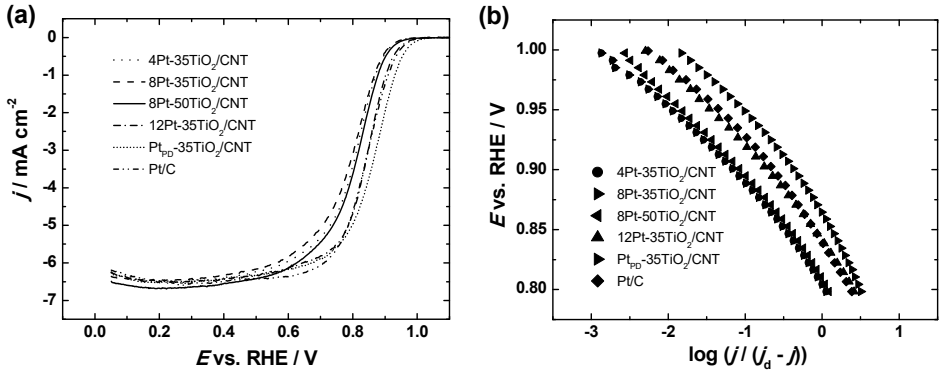

Figure 32. Comparison of RDE polarisation curves of Pt-TiO_2/CNT catalysts and commercial Pt/C measured at 1900 rpm in O_2-saturated 0.1 M KOH solution (a) and Tafel plots constructed from the ORR data (b).

Figure 32b presents mass-transfer corrected Tafel plots constructed from the RDE data shown in Figure 32a. The Tafel slope values calculated at low current densities were close to -60 mV, while those at high current density were close to -120 mV, indicating that the slow transfer of the first electron to the adsorbed O_2 molecule is the rate-determining step. Similar findings regarding the ORR kinetics on supported Pt cathode catalysts have been reported earlier [33, 42, 216, 217]. It was discovered that 4Pt-35TiO_2/CNT catalyst possesses remarkably higher SA value (0.22 mA cm^{-2}) than that of the 8Pt-35TiO_2/CNT (0.17 mA cm^{-2}) (Table 7), which is ascribed to the highly dispersed Pt NPs on the TiO_2 coated MWCNTs as can be seen in the SEM (Figure 23) and STEM (Figure 29) images. A comparison of the 8Pt-35TiO_2/CNT catalyst to its 8Pt-50TiO_2/CNT counterpart revealed that the latter showed a slight increase in the SA value as expected based on the Pt NPs supported on relatively thicker TiO_2 layer providing SMSI. The specific activities of 12Pt-35TiO_2/CNT (0.35 mA cm^{-2}) and $Pt_{(PD)}$-35TiO2/CNT (0.30 mA cm^{-2}) are much higher to that of the commercial Pt/C catalyst (0.20 mA cm^{-2}). The MA values calculated for all the prepared catalysts in comparison to that of the Pt/C are given in Table 7. The

highest MA of 124 A g^{-1} was shown by $Pt_{(PD)}$-35TiO_2/CNT, which is twice higher as that of the commercial Pt/C (62 A g^{-1}). This can be attributed to the dispersion of the Pt NPs on the TiO_2/CNT support as seen in Figure 29. In the case of sputter-deposited Pt NPs, the mass activities of the catalysts followed nearly the same trend as that of the specific activities. It can be concluded that the deposition of Pt NPs and the metal-support interaction plays an important role in the ORR activity of Pt-TiO_2/CNT catalysts. For example, the higher MA of 4Pt-35TiO_2/CNT of 36 A g^{-1} in comparison to 8Pt-35TiO_2/CNT (22 A g^{-1}) and 8Pt-50TiO_2/CNT (25 A g^{-1}) can be explained on the basis of deposition of the Pt nanoparticles and their interaction with the metal oxide. Similarly, 8Pt-50TiO_2/CNT catalysts appeared to be slightly more active than 8Pt-35TiO_2/CNT that can be attributed to the relative thickness of the metal oxide coating.

Table 7. Kinetic parameters for the ORR on Pt-TiO_2/MWCNT catalysts measured in 0.1 M KOH solution (ω=1900 rpm).

Electrode	A_r (cm^2)	Tafel slope (mV) lcd	Tafel slope (mV) hcd	$E_{1/2}$ (V)	SA at 0.9 V (mA cm^{-2})	MA at 0.9 V (A g^{-1})
4Pt-35TiO_2/CNT	0.18	-55	-121	0.80	0.22	36
8Pt-35TiO_2/CNT	0.31	-55	-121	0.79	0.17	22
8Pt-50TiO_2/CNT	0.32	-60	-122	0.81	0.19	25
12Pt-35TiO_2/CNT	0.37	-61	-126	0.84	0.35	38
$Pt_{(PD)}$-35TiO_2/CNT	1.06	-61	-124	0.86	0.30	124
Commercial Pt/C	0.86	-64	-120	0.84	0.20	62

6.5.4 Long-term durability of Pt-TiO_2/MWCNT

Long-term durability of 8Pt-35TiO_2/CNT and $Pt_{(PD)}$-35TiO_2/CNT catalysts was examined in comparison to Pt/C (20 wt.%) by measuring repetitive potential cycles in 0.1 M KOH solution. During this test 10,000 cycles were measured in the potential range from 0.6 to 1.0 V at a scan rate of 100 mV s^{-1}. Relative loss in the real surface area of Pt during ADT was determined from the hydrogen desorption peaks in the CV curves measured from 0.05 to 1.45 V at 50 mV s^{-1} after each 1000^{th} cycle. A comparison of the relative loss in the surface areas of the electrode during ADT revealed that $Pt_{(PD)}$-35TiO_2/CNT and 8Pt-35TiO_2/CNT are more resistant to degradation retaining 77% and 74% of their real surface areas after 10,000 potential cycles, respectively (Figure 33b). However, commercial Pt/C retained only 60% of its surface area, which is due to the weaker interaction of the Pt NPs with the carbon support. The ORR activity was investigated by measuring RDE polarisation curves at 1900 rpm in O_2-saturated

0.1 M KOH solution, before and after the durability test (Figure 33a). It was found that the $E_{1/2}$ value for $Pt_{(PD)}$-35TiO_2/CNT, 8Pt-35TiO_2/CNT and Pt/C (20 wt.%) decreased by 12, 22 and 108 mV, respectively. Similar results regarding durability of TiO_2 supported Pt NPs in comparison to Pt/C have been reported earlier [122, 126, 132]. Previous studies regarding durability of Pt catalyst supported on chemically synthesised graphene-TiO_2 composite revealed relatively low durability of the prepared catalyst as compared to that of the commercial Pt/C, which might be associated with the weak anchoring of the Pt NPs on the TiO_2 coated graphene support [128]. Similar studies on Nb-doped TiO_2 supported Pt catalyst have been reported by Elezovic et al. [216]. They reported 4-electron reduction pathway of the Nb-TiO_2/Pt catalyst with comparable ORR activity to that of Pt/C (20 wt%). However, they performed 50 repetitive cycles in the potential range of 0.03–1.2 V at 100 mV s^{-1}, which is not enough to investigate long-term durability of the catalyst. Interestingly, the specific activity of the 8Pt-35TiO_2/CNT catalyst increased from 0.16 to 0.25 mA cm^{-2} with cycling, which might be because of the surface modification of the catalyst and development of more active sites during potential cycling.

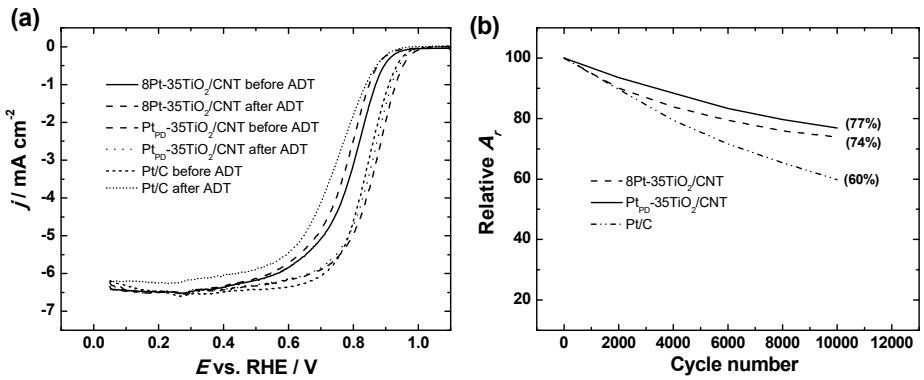

Figure 33. RDE polarisation curves of Pt-TiO_2/CNT and commercial Pt/C in O_2-saturated 0.1 M KOH solution at 1900 rpm before and after ADT (v = 10 mV s^{-1}) (a) and relative loss in the surface areas during ADT (b).

6.7 Oxygen reduction on Pt/C (PD) and Pt/SnO_2-C (PD) catalysts

6.7.1 Surface characterisation of Pt/C (CCR), Pt/C (PD), and Pt/SnO_2-C (PD)

Depending on the deposition method and nature of the support surface, Pt catalysts of different surface morphology were prepared. Figure 34 displays scanning electron micrographs and transmission electron micrographs of Pt/C synthesised via carbonyl chemical rout (CCR), Figures 34(a, d), Pt/C synthe-

sised by photo-deposition (PD), Figures 34(b, e) and Pt/40wt.%-SnO_2-C (PD), Figures 34(c, f) catalysts. It can be seen that in case of CCR, the Pt NPs are uniformly distributed over the carbon support particles indicating a narrow particle-size distribution. Pt photo-deposition, on the other hand, gives rise to the formation of Pt NPs of various shape and size, agglomerated at particular nucleation sites. This can be explained on the basis of the deposition mechanism of the two methods. In CCR, Pt NPs deposit on the sp^3 like nanodomains of the carbon support while in photo-deposition the nanoparticles tend to deposit on the sp^2 nanodomains [157]. Figure 34(c) and 34(f) show SEM and TEM images of Pt/40wt.%-SnO_2-C (PD), respectively, revealing that Pt NPs are preferably deposited on the SnO_2 nanoparticles rather than on carbon support. Similar results were observed for Pt/20wt.%-SnO_2-C (PD), Pt/60wt.%-SnO_2-C (PD) and Pt/SnO_2 (PD) catalysts. These results can be explained on the basis of the photo-deposition mechanism reported by Ma et al. [148]. Briefly, deposition of the Pt NPs is triggered by the generation of electron-hole pair in the semiconductor metal oxides, induced by photon whereas isopropanol acts as a hole scavenger.

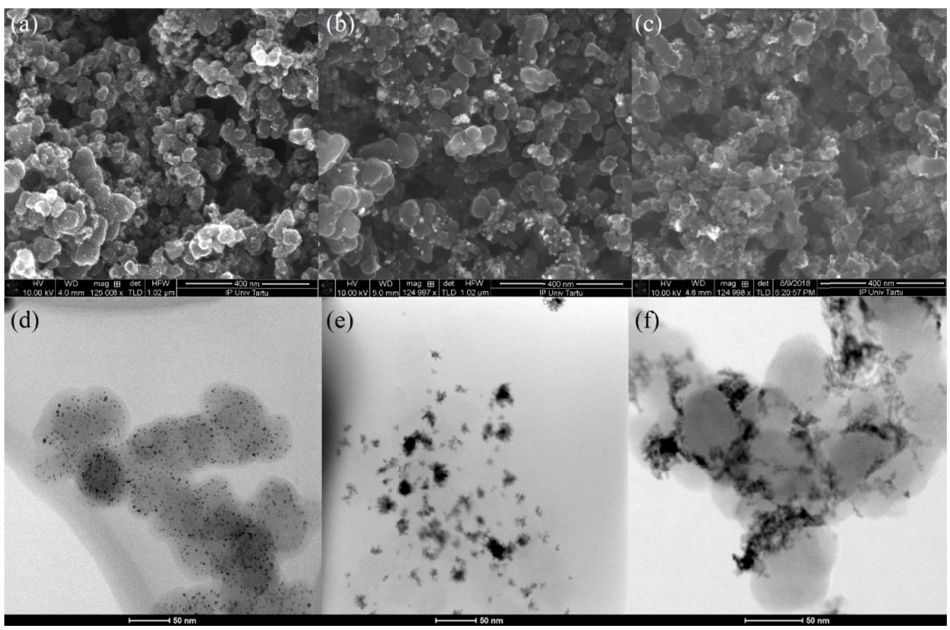

Figure 34. SEM images of Pt/C (CCR) (a), Pt/C (PD) (b) and Pt/40wt.%-SnO_2-C (PD) (c), and TEM images of Pt/C (CCR) (d), Pt/C (PD) (e), and Pt/40wt.%-SnO_2-C (PD) (f) catalysts.

Figure 35 shows the XRD patterns for the Pt/C and Pt-SnO_2/C samples synthesised by the carbonyl complex route and photo-deposition in the range of 2θ from 20 to 95º. In Pt/C (CCR), we can observe the characteristic Bragg angles for the platinum planes (ICCD-PDF#04-0802) which is as reference for the catalytic centre. The Pt-SnO_2/C (CCR) sample has only one phase, which is directly related to the catalytic centre without modification in the diffraction angle. This analysis revealed that the presence of SnO_2 does not directly or indirectly influence the lattice of Pt. This phenomenon is not similar when comparing the samples synthesised by the photo-deposition for Pt/C (PD) and Pt-SnO_2/C (PD). First, two phases related to Pt and SnO_2 (ICCD-PDF#077-0451) are present in the Pt-SnO_2/C sample. The structural parameters obtained from the Rietveld adjustment (R_{wp}: weighted pattern R factor; R_{exp}: experimental R factor; GofF: Goodness of fit = R_{wp}/R_{exp}) are summarised in Table 9. For CCR synthesis, the Pt particle size and lattice parameter of the Pt/C and Pt-SnO_2/C samples are not significantly modified, which would indicate that there is not interaction with the support. On the other hand, this phenomenon is not the same using the photo-deposition path, the particle size increases from 13.4 ± 0.03 to 17.4 ± 0.03 nm for Pt. This modification can be associated to the metal support interaction, where the lattice parameter increases from $3.9171 \pm 8.5\times10^{-5}$ to $3.9229 \pm 9.1\times10^{-4}$ Å

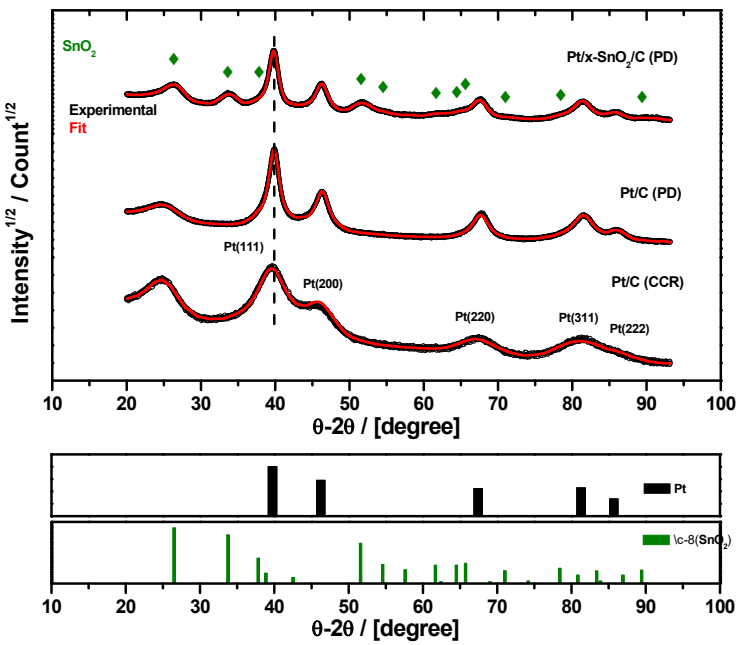

Figure 35. XRD profiles and Rietveld adjustment for Pt/C (CCR): %R_{wp} = 1.94, %GofF = 1.34, Pt/C (PD): %R_{wp} = 2.57, %GofF = 1.64, and Pt-SnO_2/C (PD): %R_{wp} = 2.55, %GofF = 1.44.

Table 9. Structural properties for materials synthesised via CCR and PD.

Sample	a (Å)	$< d >$ (nm)	%α	%ε
Pt/C (CCR)	$3.9435 \pm 3.14\times10^{-4}$	5.10 ± 0.10	6.5 ± 0.11	1.3 ± 0.03
Pt/C (PD)	$3.9174 \pm 8.50\times10^{-5}$	13.40 ± 0.03	1.5 ± 0.01	0.63 ± 0.01
Pt-SnO_2/C (CCR)	$3.9351 \pm 2.10\times10^{-4}$	4.70 ± 0.03	4.0 ± 0.07	0.90 ± 0.02
Pt/20wt.%-SnO_2-C (PD)	$3.9229 \pm 9.10\times10^{-4}$	17.03 ± 0.06	1.7 ± 0.02	0.65 ± 0.01

Adjustment parameter for Pt-SnO_2/C (CCR): $\%R_{wp} = 1.85$, %GofF = 1.26

Figure 36 shows the XPS spectra of Pt/C, Pt/20wt.%SnO_2-C and Pt/SnO_2 catalysts. The XPS spectra of Pt/C (CCR) in the Pt 4f region show the doublet centred at 71.20 (Pt $4f_{7/2}$) and 74.60 eV (Pt $4f_{5/2}$). For Pt NPs photo-deposited on carbon, a binding energy downshift, in both peaks to 71.00 and 74.30 eV, is observed, indicating interaction of the Pt NPs with the sp^2 nanodomains of the carbon support [104, 157]. Further downshift in peak corresponding to Pt $4f_{7/2}$ to 70.90 eV is observed for all Pt/x-SnO_2-C (PD) catalysts. This can be, again, attributed to the interaction of the Pt NPs with the metal oxide sites of the oxide-carbon composite that results into an increased electronic change on the catalytic centre. In case of Pt/SnO_2 (PD), both emission peaks are centred at 71.14 and 74.54 eV, respectively.

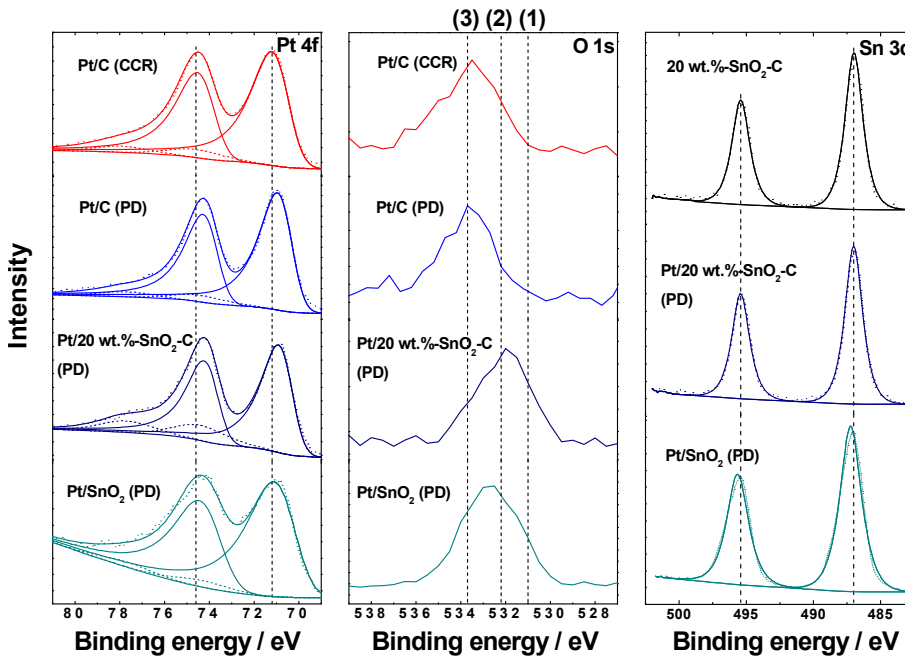

Figure 36. XPS spectra in the Pt 4f, O 1s and Sn 3d regions for Pt/C, Pt/20wt.%SnO_2-C and Pt/SnO_2 catalysts.

The XPS spectra of SnO_2 show two main peaks at 487.00 and 495.00 eV for 20 wt.%-SnO_2-C composite and all Pt/x-SnO_2-C (PD) type materials that corresponds to Sn $3d_{5/2}$ and Sn $3d_{3/2}$ (Table 10). However, in the case of Pt/SnO_2 (PD) the BE for Sn $3d_{5/2}$ and Sn $3d_{3/2}$ upshifts by ca. 240 meV. Figure 36 also summarises the main O 1s photoemission peaks as lines 1–3 for all samples containing Pt NPs. For Pt/C (CCR) or (PD) two components at 532.2, and 533.7 eV can be associated to carbonyl group and/or oxidised Pt, and to adsorbed molecular water, respectively, lines (2) and (3). These species are also present in Pt/20 wt.%-SnO_2-C (PD) and Pt/SnO_2 (PD), plus an additional component at 531 eV assigned to the oxygen in the SnO_2. The mass Pt loading in all the samples, as determined by ICP-MS, was found to be 20 wt.%.

Table 10. Analysis of the Pt 4f and Sn 3d photoemission lines for Pt/C (CCR), Pt/C (PD), Pt/x%SnO_2-C (PD) catalysts.

Sample	Pt $4f_{7/2}$ (eV)	Pt $4f_{5/2}$ (eV)	Sn $3d_{5/2}$ (eV)	Sn $3d_{3/2}$ (eV)
Pt/C (CCR)	71.2	74.6	-	-
Pt/C (PD)	71.0	74.3	-	-
20wt/%-SnO_2-C	-	-	487.0	495.4
Pt/20wt/%-SnO_2-C (PD)	70.9	74.3	487.0	495.4
Pt/40wt/%-SnO_2-C (PD)	70.9	74.3	487.0	495.4
Pt/60wt/%-SnO_2-C (PD)	70.9	74.3	487.0	495.4
Pt/SnO_2 (PD)	71.1	74.5	487.2	495.6

6.7.2 Electrochemical characterisation of Pt/C (CCR), Pt/C (PD), and Pt/SnO_2-C (PD)

Cyclic voltammograms of Pt/C (CCR), Pt/C (PD) and Pt/x-SnO_2-C (PD) catalysts, measured in N_2-saturated 0.1 M $HClO_4$ at 50 mV s^{-1} are shown in Figure 37. Surface modification of the catalysts and its dependence on the deposition method and support can be observed in the H_{UPD} and Pt surface oxidation/OH adsorption regions. For example, in addition to the hydrogen desorption peaks at 0.15 and 0.24 V attributed to the adsorption states associated to (110) and (100) sites [181], a small anodic wave centred at 0.34 V also appears on all the catalysts prepared by PD. This wave may be attributed to the formation of Pt (111) sites [218, 219], meaning that photo-deposited Pt NPs offer relatively more adsorption/desorption sites. The real surface area of Pt was calculated from the hydrogen desorption peaks and is presented in Table 11 [176]. The higher surface area of Pt/C (CCR) (A_r = 3.35 cm^2) can be expected from its narrow particle size distribution as shown in Figures 34(a, d). The A_r value of Pt/C (PD) (3.79 cm^2) is closer to Pt/C (CCR), which can be attributed to the morphology of Pt NPs formed by photo-deposition, Figure 34(e), and formation

of more adsorption/desorption sites at the electrode surface (Figure 37). The lowest surface area of Pt/20wt.%-SnO_2-C (PD) can be related to low metal oxide content in the support. Pt/40wt.%-SnO_2-C (PD) and Pt/60wt.%-SnO_2-C (PD), however, showed similar A_r values of 3.63 and 3.35 cm^2, respectively. Due to the poor *i-E* profile, which can be ascribed to the low conductivity of the metal oxide, the electrochemical results of Pt/SnO_2 (PD) are not presented here and after.

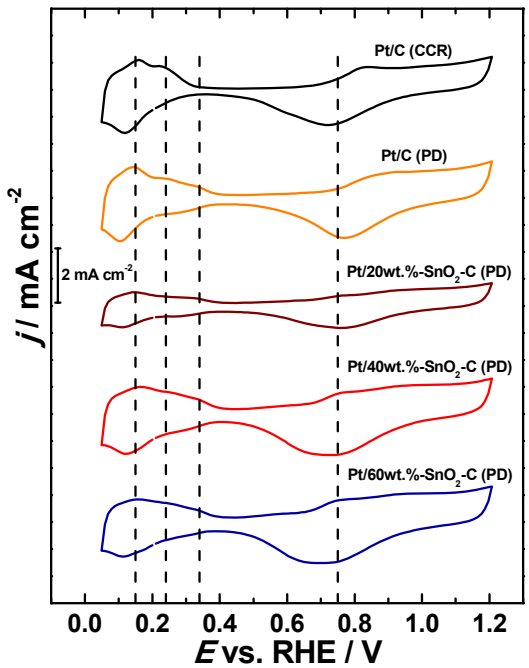

Figure 37. Cyclic voltammograms of Pt/C (CCR), Pt/C (PD), Pt/x%SnO_2-C (PD) catalysts in N_2-saturated 0.1 M $HClO_4$ solution (v = 50 mV s^{-1}).

Figure 38 displays the CO oxidation profile of Pt/40wt.%-SnO_2-C (PD), which is entirely different from the one obtained from Pt/C (Figure 39), hence providing evidence of the SMSI at the interface. The absence of hydrogen oxidation peaks between $0.0 < E < 0.4$ V in the first forward scan confirms blockage of the electrode surface by adsorbed CO species. It can be seen that the electrooxidation of the CO monolayer takes place in a wide potential range. Multiple anodic peaks with an onset potential of 0.28 V can be observed. Briefly, in addition to the main CO oxidation peak at 0.61 V, another broad peak appeared at 0.38 V. Moreover, a small peak at 0.67 V and a hump at 0.75 V were also observed. Similar CO oxidation profiles were obtained for all Pt/x-SnO_2-C catalysts. Gonzalez and al. [220] reported similar CO oxidation profiles for Pt-Sn catalyst in acid media. CO oxidation behaviour on Pt-Sn type electro-

catalysts has been explained on the basis of a bifunctional mechanism, where oxidation of the adsorbed CO is facilitated by the active O species provided by the OH adsorbed on Sn sites [221, 222]. According to Gasteiger et al., alloying Pt with a more active metal provides adsorbed OH at a relatively more negative potential [223]. A typical example of which is Pt-Ru bimetallic catalysts used for the methanol oxidation reaction. Pt/x-SnO_2-C (PD) shows an oxophilic effect of Sn, comparable to that of Ru alloyed with Pt [224]. Likewise, the CO oxidation profile of Pt/x-SnO_2-C (PD) catalysts can be better interpreted when compared to Pt/C (CCR) and Pt/C (PD) catalyst as shown in Figure 39.

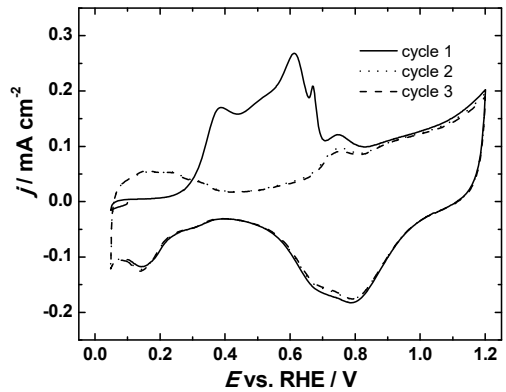

Figure 38. CO oxidation profile of Pt/40wt.%-SnO_2-C (PD) catalyst in N_2-saturated 0.1 M $HClO_4$ solution (v = 5 mV s^{-1}).

The main peak of CO oxidation on Pt/C (CCR) is centred at 0.75 V. This typical CO stripping response is attributed to Pt NPs deposited on -C-C- domains (sp^3-like) of the carbon support [157]. The photo-deposition process points to a selective deposition of Pt NPs onto sp^2 domains of carbon [157], and/or onto the oxide sites of the oxide-carbon composite [225]. This is the reason why, on Pt/C (PD) the main peak is shifted negatively and centred at 0.67 V. The main peak (0.61 V) in Pt/20wt.%-SnO_2-C (PD), can be ascribed to the selective deposition of the Pt NPs on the metal oxide, whereas the onset at 0.2 V peaking at 0.38 V may be attributed to the formation of Pt-Sn nanoalloys at the interface [221, 222, 226], where the oxophilicity of Sn centres (a chemical effect), in acid medium, plays an essential role for the negative potential shift of the CO stripping (bifunctional-like effect). This phenomenon is, apparently, nullified in alkaline medium, since for the same system in this medium, just gives a glimpse of the electronic effect, as compared to Pt/C (CCR) in the same medium (Figure 39). Herein, the main peak appears at 0.63 V with a shoulder at 0.56 V and a pre-peak at ~0.4 V. On the Pt photodeposited Pt, the small peak at 0.75 V in Pt/C (PD) and Pt/20wt.%-SnO_2-C (PD) reveals a small quantity of Pt NPs deposited on the sp^3-like nanodomains.

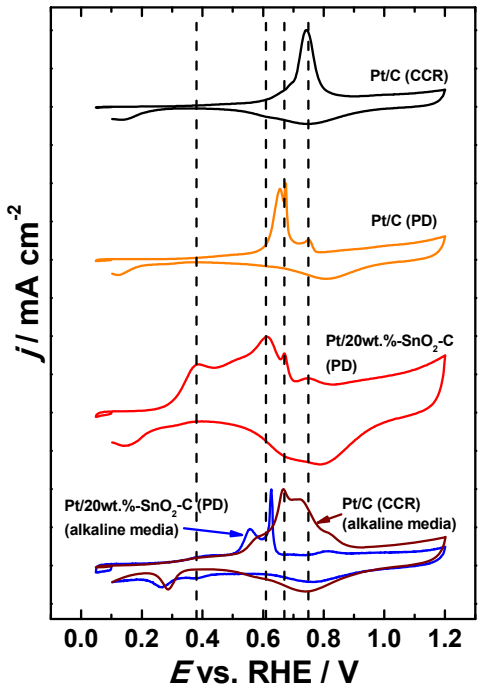

Figure 39. Comparison of normalised CO oxidation peaks of the Pt/C (CCR), Pt/C (PD), Pt/x%SnO_2-C (PD) catalysts in N_2-saturated 0.1 M $HClO_4$ and 0.1 M KOH solutions (v = 5 mV s^{-1}).

6.7.3 ORR studies on Pt/C (CCR), Pt/C (PD), and Pt/SnO_2-C (PD) catalysts

Electrochemical reduction of oxygen was carried out at various electrode rotation rates in O_2-saturated 0.1 M $HClO_4$ solution. Comparison of the ORR activity is presented in Figure 40(a). The $E_{1/2}$ values for all the electrodes are close to each other (~0.89 V) as given in Table 11. These results are in good agreement with the previous work [119]. Tafel slope values calculated at low and high current densities for electrodes are close to –60 and –120 mV, respectively, (Table 11), revealing the first electron transfer to the O_2 molecule as the rate-determining step.

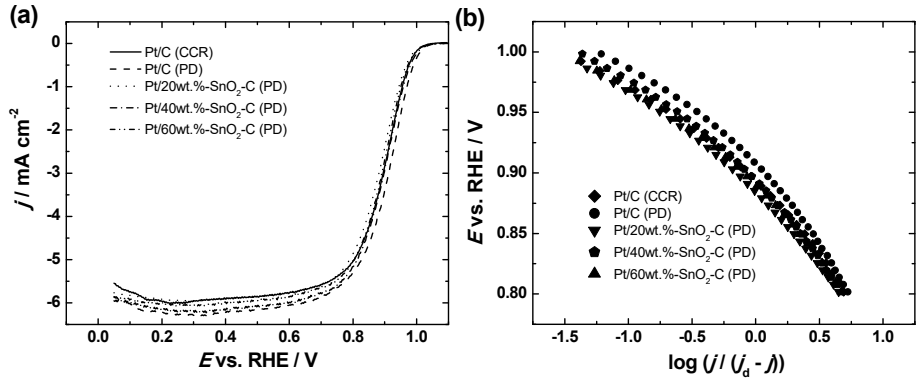

Figure 40. RDE polarisation curves for O_2 reduction measured at 1600 rpm in O_2-saturated 0.1 M $HClO_4$ solution (v = 10 mV s^{-1}) (a) and mass transfer corrected Tafel plots (b).

Specific activity values were calculated from the determined kinetic current I_k at a specific potential using Eq. (10). The highest SA of 0.41 and 0.44 mA cm^{-2} at 0.9 V was shown by Pt/C (PD) and Pt/20wt.%-SnO_2-C (PD), respectively. Pt/C (CCR) showed SA of 0.37 mA cm^{-2} while Pt/40wt.%-SnO_2-C (PD) and Pt/60wt.%-SnO_2-C (PD) showed similar SA values of 0.30 mA cm^{-2} (Table 11). Mass activity of the catalysts was determined by Eq. (11). The highest MA of 94 mA mg^{-1} at 0.9 V is shown by Pt/C (PD), while Pt/C (CCR) showed MA of 75 mA mg^{-1} (Table 11). The mass activities of Pt/20wt/%-SnO_2-C (PD), Pt/40wt/%-SnO_2-C (PD) and Pt/60wt/%-SnO_2-C (PD) are 49, 66 and 61 mA mg^{-1}, respectively. In addition to the MA, we calculated the turnover frequency (TOF, e^- $site^{-1}$ s^{-1}) as a function of particle size using Eq. (12) [227]:

$$TOF\ (e^{-}site^{-1}s^{-1}) = \frac{M_{Pt}}{F} MA \qquad (12)$$

where M_{Pt} and F are the atomic mass of Pt and Faraday constant, respectively. According to Fig. 10(b) a similar phenomenon with the SA is observed. We could expect that the increase of the Pt crystallite size might affect the TOF [205]. Although, the crystallite size increased, the heterojunction between Pt NPs and oxide domains maintain the same electro-activity in all crystallite size interval. This finding is related to the strong-metal support interaction effect, where SnO_2 can act as an active site to adsorb OH^- ions at the surface [228].

Table 11. Kinetic parameters for ORR on Pt/C (CCR), Pt/C (PD) and Pt/x-SnO_2-C (PD) catalysts in 0.1 M $HClO_4$ solution.

Electrode	A_r (cm^2)	ECSA ($m^2\ g^{-1}_{Pt}$)	Tafel slope (mV) lcd	Tafel slope (mV) hcd	$E_{1/2}$ (V)	SA at 0.9 V (mA cm^{-2})	MA at 0.9 V (mA mg^{-1})
Pt/C (CCR)	3.35 ± 0.10	63 ± 2	-59 ± 1	-119 ± 3	0.90 ± 0.01	0.37 ± 0.01	75 ± 1
Pt/C (PD)	3.79 ± 0.09	72 ± 2	-65 ± 1	-133 ± 6	0.90 ± 0.01	0.41 ± 0.02	94 ± 5
Pt/20wt.%-SnO_2-C (PD)	1.72 ± 0.07	33 ± 1	-63 ± 3	-119 ± 5	0.88 ± 0.01	0.44 ± 0.05	49 ± 4
Pt/40wt.%-SnO_2-C (PD)	3.63 ± 0.05	69 ± 1	-63 ± 2	-127 ± 2	0.89 ± 0.01	0.30 ± 0.06	66 ± 5
Pt/60wt.%-SnO_2-C (PD)	3.35 ± 0.05	63 ± 1	-62 ± 2	-122 ± 4	0.89 ± 0.01	0.30 ± 0.03	61 ± 4

6.7.4 Long-term durability of Pt/SnO_2-C (PD) and Pt/C (CCR) catalysts

It has been reported earlier that the thermodynamic degradation of carbon support that takes place at $E > 0.9$ V, can be (partially) inhibited by incorporating metal oxide at the interface [105]. Degradation of the Pt catalyst itself is one of the main obstacles in the industrial development of fuel cell technology. Chorkendorff et al. [229] studied the degradation of Pt NPs by subjecting the Pt/C catalyst, prepared by the inverse micelles method into various durability measurements. In their analysis, TEM and particle size distribution investigation showed that the dominant mechanism of Pt degradation is the dissolution of the nanoparticles in acid media. Moreover, Pt degradation accelerated at $E >$ 1.1 V vs RHE. In the present work, durability of the Pt/C (CCR) and Pt/20wt.%-SnO_2-C (PD) catalysts was investigated by performing 2500 potential cycles in the potential range of 0.6–1.2 V at 50 mV s^{-1}. In order to observe degradation of the nanoparticles and modification of the electrocatalyst surface, cyclic voltammograms in the potential window (0.05–1.2 V), CO stripping and ORR at 1600 rpm were measured after each 500^{th} cycle. During the ADT, Pt/C (CCR) showed a consistent degradation during potential cycling, while on the other hand, photo-deposited Pt nanoparticles were resistant to degradation, particularly after 2000^{th} cycle. After the first 500 cycles, Pt/20wt.%-SnO_2-C (PD) showed an increase in the real surface area of Pt, which might be attributed to the cleaning of the surface and exposure of more catalytic sites with potential cycling. Similar results are presented by Ozouf et al. [230] where they reported 33% decrease in the specific surface area of Pt deposited on Sb-doped SnO_2 (Pt/ATO) after 5000 potential cycles between 1.0–1.5 V vs. RHE. The CO stripping performed after each 500^{th} cycle revealed remarkable corrosion resistant property of photo-deposited Pt NPs onto SnO_2-C composite for the ORR as a result of the SMSI effect.

Figure 41b illustrates the RDE polarisation curves for O_2 reduction measured during ADT. It was observed that the drop in the $E_{1/2}$ value for Pt/C (CCR) is 44 mV, while Pt/20wt.%-SnO_2-C (PD) showed a decrease of 14 mV during ADT. From the ADT, it can be concluded that Pt photo-deposited on metal oxide is more resistant to degradation as compared to Pt/C (CCR).

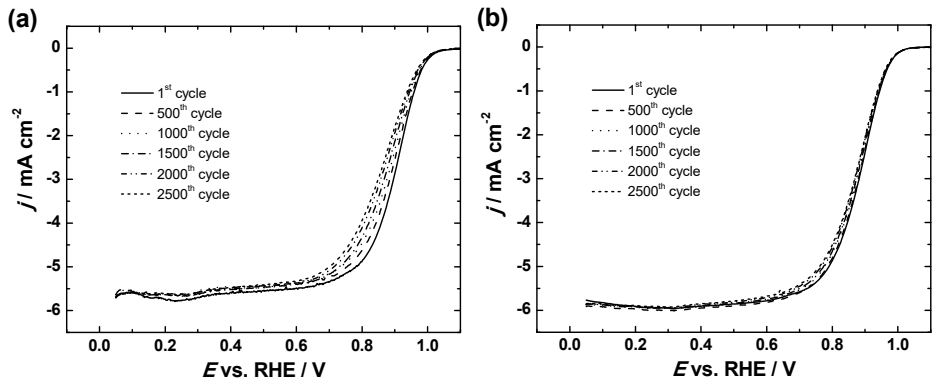

Figure 41. ORR polarisation curves of Pt/C (CCR) (a) and Pt/20wt.%-SnO_2-C (PD) (b) catalysts in O_2-saturated 0.1 M $HClO_4$ solution measured at 1600 rpm during ADT.

7. SUMMARY

The electrochemical reduction of oxygen on supported catalysts was investigated on various carbon-based and oxide-carbon composite supports in acidic and alkaline media using the rotating disk electrode system. Different methods used for the deposition of Pt nanoparticles on the support materials include electrodeposition, ethylene glycol method, He/H_2 plasma jet treatment, magnetron sputtering, carbonyl chemical synthesis and photo-deposition. Metal oxide-carbon composites were synthesised by atomic layer deposition technique and by modified sol-gel method.

In the first part of the thesis, the ORR activity of the Pt NPs electrochemically deposited on acid-treated MWCNTs were studied in 0.05 M H_2SO_4 solution. Two different deposition potentials and various number of pulses (in the range of 100–1500) were employed to evaluate surface morphology of the prepared Pt/MWCNT catalysts and its influence on the ORR activity. Pt/MWCNT catalysts showed higher specific activities than that of the commercial 20 wt.% Pt/C. The O_2 reduction reaction followed a four-electron pathway on Pt/MWCNT catalysts as was determined using the Koutecky-Levich equation. Tafel slope values revealed that slow transfer of the first electron to adsorbed O_2 molecule is the rate-determining step for ORR on Pt/MWCNT.

Electrocatalytic activity and long-term durability of Pt nanoparticles supported on nitrobenzene-modified graphene was investigated in 0.1 M KOH solution. The prepared Pt-NB/G catalyst showed excellent electrocatalytic activity for ORR in alkaline media, with half-wave potentials and specific activity values very close to those obtained for commercial 20 wt.% Pt/C catalyst in identical conditions. Long-term durability measurements showed high stability of the Pt-NB/G catalyst.

Afterwards, the ORR activity of Pt nanoparticles deposited on reduced graphene oxide and N-doped reduced graphene oxide prepared by plasma-assisted synthesis, was studied in 0.05 M H_2SO_4 and 0.1 M KOH solutions. The prepared Pt/rGO and Pt/rGO-N catalysts showed remarkable electrocatalytic behaviour towards the ORR in both alkaline and acidic media.

Heat-treatment effect on Pt/MWCNT catalysts prepared by magnetron sputtering, was investigated in 0.05 M H_2SO_4 and 0.1 M KOH solutions. The catalysts were annealed at different temperatures between 300 and 700 ºC in N_2 atmosphere for 30 min. Physico-chemical and electrochemical characterisation confirmed modification of the Pt/MWCNT electrodes surface morphology after heat-treatment at different temperatures. From RDE results it is concluded that 300 ºC is the optimum annealing temperature to improve the ORR activity of Pt/MWCNT electrocatalysts.

In the next step, Pt NPs were sputter-deposited on the TiO_2 coated MWCNTs. Different loadings of Pt and TiO_2 were employed to evaluate its effect on the ORR activity and long-term durability of Pt-TiO_2/MWCNT catalysts. Electrochemical results in 0.05 M H_2SO_4 and 0.1 M KOH solutions

revealed that all the Pt-TiO_2/MWCNT catalysts possess relatively higher ORR activity and better stability than that of commercial 20 wt% Pt/C. The Koutecky–Levich analysis confirmed four-electron pathway of O_2 reduction on Pt-TiO_2/MWCNT catalysts.

In the last part of the thesis, Pt nanoparticles were photo-deposited on SnO_2-C composites prepared by a modified sol-gel method. Various loadings of SnO_2 were used to evaluated support effect on the electrocatalytic activity and durability of Pt/SnO_2-C in 0.1 M $HClO_4$ solution, in comparison to Pt/C prepared by carbonyl chemical route. It was concluded that Pt/SnO_2-C catalysts possess remarkable ORR activity and long-term durability due to the strong metal-support effect.

8. REFERENCES

[1] A. Rabis, P. Rodriguez, T.J. Schmidt, Electrocatalysis for polymer electrolyte fuel cells: Recent achievements and future challenges, ACS Catalysis 2(5) (2012) 864–890.

[2] A.M. Gomez-Marin, J.M. Feliu, Oxygen reduction at platinum electrodes: The interplay between surface and surroundings properties, Current Opinion in Electrochemistry 9 (2018) 166–172.

[3] K. Kinoshita, Electrochemical oxygen technology, Wiley, New York, 1992.

[4] R. Adžic, Recent advances in the kinetics of oxygen reduction, in: J. Lipkowski, P.N. Ross (Eds.), Electrocatalysis, Wiley-VCH, New York, 1998, pp. 197–242.

[5] E. Yeager, Dioxygen electrocatalysis - mechanisms in relation to catalyst structure, Journal of Molecular Catalysis 38(1–2) (1986) 5–25.

[6] J. Stacy, Y.N. Regmi, B. Leonard, M.H. Fan, The recent progress and future of oxygen reduction reaction catalysis: A review, Renewable & Sustainable Energy Reviews 69 (2017) 401–414.

[7] M.R. Tarasevich, A. Sadkowski, E. Yeager, in: B.E. Conway, J.O.M. Bockris, E. Yeager, S.U.M. Khan, R.E. White (Eds.), Comprehensive treatise of electrochemistry, Plenum Press, New York, 1983, pp. 301–398.

[8] J.X. Wang, N.M. Markovic, R.R. Adzic, Kinetic analysis of oxygen reduction on Pt(111) in acid solutions: Intrinsic kinetic parameters and anion adsorption effects, Journal of Physical Chemistry B 108(13) (2004) 4127–4133.

[9] A.J. Medford, A. Vojvodic, J.S. Hummelshoj, J. Voss, F. Abild-Pedersen, F. Studt, T. Bligaard, A. Nilsson, J.K. Norskov, From the Sabatier principle to a predictive theory of transition-metal heterogeneous catalysis, Journal of Catalysis 328 (2015) 36–42.

[10] H.A. Hansen, V. Viswanathan, J.K. Nørskov, Unifying kinetic and thermodynamic analysis of 2 e^- and 4 e^- reduction of oxygen on metal surfaces, The Journal of Physical Chemistry C 118(13) (2014) 6706–6718.

[11] I.S. Flyagina, K.J. Hughes, M. Pourkashanian, D.B. Ingham, DFT study of the oxygen reduction reaction on iron, cobalt and manganese macrocycle active sites, International Journal of Hydrogen Energy 39(36) (2014) 21538–21546.

[12] J.K. Norskov, J. Rossmeisl, A. Logadottir, L. Lindqvist, J.R. Kitchin, T. Bligaard, H. Jonsson, Origin of the overpotential for oxygen reduction at a fuel-cell cathode, Journal of Physical Chemistry B 108(46) (2004) 17886–17892.

[13] B.W. Zhang, H.L. Yang, Y.X. Wang, S.X. Dou, H.K. Liu, A comprehensive review on controlling surface composition of Pt-based bimetallic electrocatalysts, Advanced Energy Materials 8(20) (2018) 17.

[14] C.L. Zhang, X.C. Shen, Y.B. Pan, Z.M. Peng, A review of Pt-based electrocatalysts for oxygen reduction reaction, Frontiers in Energy 11(3) (2017) 268–285.

[15] N. Alexeyeva, K. Tammeveski, A. Lopez-Cudero, J. Solla-Gullon, J.M. Feliu, Electroreduction of oxygen on Pt nanoparticle/carbon nanotube nanocomposites in acid and alkaline solutions, Electrochimica Acta 55(3) (2010) 794–803.

[16] N. Jung, D.Y. Chung, J. Ryu, S.J. Yoo, Y.E. Sung, Pt-based nanoarchitecture and catalyst design for fuel cell applications, Nano Today 9(4) (2014) 433–456.

[17] N.M. Markovic, T.J. Schmidt, V. Stamenkovic, P.N. Ross, Oxygen reduction reaction on Pt and Pt bimetallic surfaces: A selective review, Fuel Cells 1(2) (2001) 105–116.

[18] S. Sui, X.Y. Wang, X.T. Zhou, Y.H. Su, S. Riffatc, C.J. Liu, A comprehensive review of Pt electrocatalysts for the oxygen reduction reaction: Nanostructure, activity, mechanism and carbon support in PEM fuel cells, Journal of Materials Chemistry A 5(5) (2017) 1808–1825.
[19] Y.J. Wang, W.Y. Long, L.L. Wang, R.S. Yuan, A. Ignaszak, B.Z. Fang, D.P. Wilkinson, Unlocking the door to highly active ORR catalysts for PEMFC applications: polyhedron-engineered Pt-based nanocrystals, Energy & Environmental Science 11(2) (2018) 258–275.
[20] N.M. Markovic, H.A. Gasteiger, P.N. Ross, Oxygen reduction on platinum low-index single-crystal surfaces in sulphuric acid solution: rotating ring-Pt(hkl) disk studies, Journal of Physical Chemistry 99(11) (1995) 3411–3415.
[21] F. Sugimura, M. Nakamura, N. Hoshi, The oxygen reduction reaction on kinked stepped surfaces of Pt, Electrocatalysis 8(1) (2017) 46–50.
[22] S.W. Lee, S. Chen, J. Suntivich, K. Sasaki, R.R. Adzic, Y. Shao-Horn, Role of surface steps of pt nanoparticles on the electrochemical activity for oxygen reduction, Journal of Physical Chemistry Letters 1(9) (2010) 1316–1320.
[23] A. Kuzume, E. Herrero, J.M. Feliu, Oxygen reduction on stepped platinum surfaces in acidic media, Journal of Electroanalytical Chemistry 599(2) (2007) 333–343.
[24] M.D. Macia, J.M. Campina, E. Herrero, J.M. Feliu, On the kinetics of oxygen reduction on platinum stepped surfaces in acidic media, Journal of Electroanalytical Chemistry 564(1–2) (2004) 141–150.
[25] N. Hoshi, M. Nakamura, A. Hitotsuyanagi, Active sites for the oxygen reduction reaction on the high index planes of Pt, Electrochimica Acta 112 (2013) 899–904.
[26] M. Shao, Q. Chang, J.-P. Dodelet, R. Chenitz, Recent Advances in Electrocatalysts for oxygen reduction reaction, Chemical Reviews 116(6) (2016) 3594–3657.
[27] N.M. Markovic, R.R. Adzic, B.D. Cahan, E.B. Yeager, Structural effects in electrocatalysis – oxygen reduction on platinum low-index single-crystal surfaces in perchloric-acid solutions, Journal of Electroanalytical Chemistry 377(1–2) (1994) 249–259.
[28] V.R. Stamenkovic, B. Fowler, B.S. Mun, G.F. Wang, P.N. Ross, C.A. Lucas, N.M. Markovic, Improved oxygen reduction activity on $Pt_3Ni(111)$ via increased surface site availability, Science 315(5811) (2007) 493–497.
[29] D.G. Li, C. Wang, D.S. Strmcnik, D.V. Tripkovic, X.L. Sun, Y.J. Kang, M.F. Chi, J.D. Snyder, D. van der Vliet, Y.F. Tsai, V.R. Stamenkovic, S.H. Sun, N.M. Markovic, Functional links between Pt single crystal morphology and nanoparticles with different size and shape: the oxygen reduction reaction case, Energy & Environmental Science 7(12) (2014) 4061–4069.
[30] W. Yuan, S. Lu, Y. Xiang, S.P. Jiang, Pt-based nanoparticles on non-covalent functionalized carbon nanotubes as effective electrocatalysts for proton exchange membrane fuel cells, RSC Advances 4(86) (2014) 46265–46284.
[31] A. Anastasopoulos, J.C. Davies, L. Hannah, B.E. Hayden, C.E. Lee, C. Milhano, C. Mormiche, L. Offin, The particle size dependence of the oxygen reduction reaction for carbon-supported platinum and palladium, Chemsuschem 6(10) (2013) 1973–1982.
[32] A. Sarapuu, A. Kasikov, T. Laaksonen, K. Kontturi, K. Tammeveski, Electrochemical reduction of oxygen on thin-film Pt electrodes in acid solutions, Electrochimica Acta 53(20) (2008) 5873–5880.

[33] A. Damjanovic, M.A. Genshaw, J.O.M. Bockris, The mechanism of oxygen reduction at platinum in alkaline solutions with special reference to H_2O_2, Journal of The Electrochemical Society 114(11) (1967) 1107–1112.
[34] A. Damjanovic, On the kinetics and mechanism of oxygen reduction at oxide film-covered Pt electrodes in acid-solutions II. electron-transfer through the oxide film and mechanism of the reduction, Journal of the Electrochemical Society 138(8) (1991) 2315–2320.
[35] N. Markovic, H. Gasteiger, P.N. Ross, Kinetics of oxygen reduction on Pt(hkl) electrodes: Implications for the crystallite size effect with supported Pt electrocatalysts, Journal of the Electrochemical Society 144(5) (1997) 1591–1597.
[36] A. Parthasarathy, S. Srinivasan, A.J. Appleby, C.R. Martin, Pressure-dependence of the oxygen reduction reaction at the platinum microelectrode nafion interface - electrode-kinetics and mass-transport, Journal of the Electrochemical Society 139(10) (1992) 2856–2862.
[37] S. Mukerjee, S. Srinivasan, A.J. Appleby, Effect of sputtered film of platinum on low platinum loading electrodes on electrode kinetics of oxygen reduction in proton exchange membrane fuel cells, Electrochimica Acta 38(12) (1993) 1661–1669.
[38] C. Song, J. Zhang, Electrocatalytic oxygen reduction reaction, in: J. Zhang (Ed.), PEM Fuel cell electrocatalysts and catalyst layers: Fundamentals and applications, Springer London, London, 2008, pp. 89–134.
[39] D.B. Sepa, M.V. Vojnovic, L.M. Vracar, A. Damjanovic, Different views regarding the kinetics and mechanisms of oxygen reduction at Pt and Pd electrodes, Electrochimica Acta 32(1) (1987) 129–134.
[40] X. Ge, A. Sumboja, D. Wuu, T. An, B. Li, F.W.T. Goh, T.S.A. Hor, Y. Zong, Z. Liu, Oxygen reduction in alkaline media: From mechanisms to recent advances of catalysts, ACS Catalysis 5(8) (2015) 4643–4667.
[41] A. Parthasarathy, S. Srinivasan, A.J. Appleby, C.R. Martin, Temperature-dependence of the electrode-kinetics of oxygen reduction at the platinum/nafion® interface – a microelectrode investigation, Journal of the Electrochemical Society 139(9) (1992) 2530–2537.
[42] D.B. Sepa, M.V. Vojnovic, A. Damjanovic, Kinetics and mechanism of O_2 reduction at-Pt in alkaline-solutions, Electrochimica Acta 25(11) (1980) 1491–1496.
[43] D.B. Sepa, M.V. Vojnovic, L.M. Vracar, A. Damjanovic, Apparent enthalpies of activation of electrodic oxygen reduction at platinum in different current density regions—I. Acid solution, Electrochimica Acta 31(1) (1986) 91–96.
[44] D.B. Sepa, M.V. Vojnovic, L.M. Vracar, A. Damjanovic, Apparent enthalpies of activation of electrodic oxygen reduction at platinum in different current density regions—II. Alkaline solution, Electrochimica Acta 31(1) (1986) 97–101.
[45] M.T. Anwar, X.H. Yan, M.R. Asghar, N. Husnain, S.Y. Shen, L.X. Luo, J.L. Zhang, Recent advances in hybrid support material for Pt-based electrocatalysts of proton exchange membrane fuel cells, International Journal of Energy Research 43(7) (2019) 2694–2721.
[46] S.N. Stamatin, M. Borghei, R. Dhiman, S.M. Andersen, V. Ruiz, E. Kauppinen, E.M. Skou, Activity and stability studies of platinized multi-walled carbon nanotubes as fuel cell electrocatalysts, Applied Catalysis B-Environmental 162 (2015) 289–299.

[47] M.A. Molina-Garcia, N.V. Rees, Effect of catalyst carbon supports on the oxygen reduction reaction in alkaline media: a comparative study, RSC Advances 6(97) (2016) 94669–94681.
[48] P. Trogadas, T.F. Fuller, P. Strasser, Carbon as catalyst and support for electrochemical energy conversion, Carbon 75 (2014) 5–42.
[49] U.A. Paulus, T.J. Schmidt, H.A. Gasteiger, R.J. Behm, Oxygen reduction on a high-surface area Pt/Vulcan carbon catalyst: a thin-film rotating ring-disk electrode study, Journal of Electroanalytical Chemistry 495(2) (2001) 134–145.
[50] E. Hark, V. Steinberg, S. Sepp, K. Vaarmets, J. Nerut, T. Kallio, K. Kontturi, E. Lust, Electrochemical and physical characterization of Pt activated micromesoporous vanadium carbide derived carbon electrodes in sulfuric acid solution, Journal of the Electrochemical Society 160(9) (2013) F923-F930.
[51] R. Jager, E. Hark, P.E. Kasatkin, E. Lust, Investigation of a carbon-supported Pt electrode for oxygen reduction reaction in 0.1M KOH aqueous solution, Journal of the Electrochemical Society 161(9) (2014) F861-F867.
[52] A.L. Dicks, The role of carbon in fuel cells, Journal of Power Sources 156(2) (2006) 128–141.
[53] Y. Wang, J. Li, Z.D. Wei, Recent progress of carbon-based materials in oxygen reduction reaction catalysis, Chemelectrochem 5(14) (2018) 1764–1774.
[54] S. Samad, K.S. Loh, W.Y. Wong, T.K. Lee, J. Sunarso, S.T. Chong, W.R.W. Daud, Carbon and non-carbon support materials for platinum-based catalysts in fuel cells, International Journal of Hydrogen Energy 43(16) (2018) 7823–7854.
[55] S. Sharma, B.G. Pollet, Support materials for PEMFC and DMFC electrocatalysts-A review, Journal of Power Sources 208 (2012) 96–119.
[56] E. Higuchi, H. Uchida, M. Watanabe, Effect of loading level in platinum-dispersed carbon black electrocatalysts on oxygen reduction activity evaluated by rotating disk electrode, Journal of Electroanalytical Chemistry 583(1) (2005) 69–76.
[57] J. Liu, M. Jiao, L. Lu, H.M. Barkholtz, Y. Li, Y. Wang, L. Jiang, Z. Wu, D.-j. Liu, L. Zhuang, C. Ma, J. Zeng, B. Zhang, D. Su, P. Song, W. Xing, W. Xu, Z. Jiang, G. Sun, High performance platinum single atom electrocatalyst for oxygen reduction reaction, Nature Communications 8 (2017) 15938.
[58] S.C. Roy, A.W. Harding, A.E. Russell, K.M. Thomas, Spectroelectrochemical study of the role played by carbon functionality in fuel cell electrodes, Journal of the Electrochemical Society 144(7) (1997) 2323–2328.
[59] E. Antolini, Carbon supports for low-temperature fuel cell catalysts, Applied Catalysis B: Environmental 88(1) (2009) 1–24.
[60] E. Auer, A. Freund, J. Pietsch, T. Tacke, Carbons as supports for industrial precious metal catalysts, Applied Catalysis A-General 173(2) (1998) 259–271.
[61] J.H. Jiang, B.L. Yi, Thickness effects of a carbon-supported platinum catalyst layer on the electrochemical reduction of oxygen in sulfuric acid solution, Journal of Electroanalytical Chemistry 577(1) (2005) 107–115.
[62] I.N. Leontyev, S.V. Belenov, V.E. Guterman, P. Haghi-Ashtiani, A.P. Shaganov, B. Dkhil, Catalytic activity of carbon-supported Pt nanoelectrocatalysts. Why reducing the size of Pt nanoparticles is not always beneficial, Journal of Physical Chemistry C 115(13) (2011) 5429–5434.
[63] K. Jukk, N. Kongi, K. Tammeveski, R.M. Arán-Ais, J. Solla-Gullón, J.M. Feliu, Loading effect of carbon-supported platinum nanocubes on oxygen electroreduction, Electrochimica Acta 251 (2017) 155–166.

[64] G.J.M. Janssen, E.F. Sitters, Performance of thin-film cathodes for proton-exchange-membrane fuel cells based on high-surface-area carbon supports, Journal of Power Sources 171(1) (2007) 8–17.
[65] M. Inaba, H. Yamada, J. Tokunaga, A. Tasaka, Effect of agglomeration of Pt/C catalyst on hydrogen peroxide formation, Electrochemical and Solid State Letters 7(12) (2004) A474-A476.
[66] R. Kou, Y.Y. Shao, D.H. Wang, M.H. Engelhard, J.H. Kwak, J. Wang, V.V. Viswanathan, C.M. Wang, Y.H. Lin, Y. Wang, I.A. Aksay, J. Liu, Enhanced activity and stability of Pt catalysts on functionalized graphene sheets for electrocatalytic oxygen reduction, Electrochemistry Communications 11(5) (2009) 954–957.
[67] M. Sharma, N. Jung, S.J. Yoo, Toward high-performance Pt-based nanocatalysts for oxygen reduction reaction through organic-inorganic hybrid concepts, Chemistry of Materials 30(1) (2018) 2–24.
[68] Y.J. Li, E.B. Zhu, T. McLouth, C.Y. Chiu, X.Q. Huang, Y. Huang, Stabilization of high-performance oxygen reduction reaction Pt electrocatalyst supported on reduced graphene oxide/carbon black composite, Journal of the American Chemical Society 134(30) (2012) 12326–12329.
[69] D.-H. Lim, J. Wilcox, Mechanisms of the oxygen reduction reaction on defective graphene-supported Pt nanoparticles from first-principles, The Journal of Physical Chemistry C 116(5) (2012) 3653–3660.
[70] J.B. Zhu, M.L. Xiao, X. Zhao, C.P. Liu, J.J. Ge, W. Xing, Strongly coupled Pt nanotubes/N-doped graphene as highly active and durable electrocatalysts for oxygen reduction reaction, Nano Energy 13 (2015) 318–326.
[71] S. Stambula, N. Gauquelin, M. Bugnet, S. Gorantla, S. Turner, S.H. Sun, J. Liu, G.X. Zhang, X.L. Sun, G.A. Botton, Chemical structure of nitrogen-doped graphene with single platinum atoms and atomic clusters as a platform for the PEMFC electrode, Journal of Physical Chemistry C 118(8) (2014) 3890–3900.
[72] M. Zhou, H.-L. Wang, S. Guo, Towards high-efficiency nanoelectrocatalysts for oxygen reduction through engineering advanced carbon nanomaterials, Chemical Society Reviews 45(5) (2016) 1273–1307.
[73] D. Higgins, M.A. Hoque, M.H. Seo, R.Y. Wang, F. Hassan, J.Y. Choi, M. Pritzker, A.P. Yu, J.J. Zhang, Z.W. Chen, Development and simulation of sulfur-doped graphene supported platinum with exemplary stability and activity towards oxygen reduction, Advanced Functional Materials 24(27) (2014) 4325–4336.
[74] J.E. Park, Y.J. Jang, Y.J. Kim, M.S. Song, S. Yoon, D.H. Kim, S.J. Kim, Sulfur-doped graphene as a potential alternative metal-free electrocatalyst and Pt-catalyst supporting material for oxygen reduction reaction, Physical Chemistry Chemical Physics 16(1) (2014) 103–109.
[75] J. Melke, B. Peter, A. Habereder, J. Ziegler, C. Fasel, A. Nefedov, H. Sezen, C. Woell, H. Ehrenberg, C. Roth, Metal-support interactions of platinum nanoparticles decorated N-doped carbon nanofibers for the oxygen reduction reaction, ACS Applied Materials & Interfaces 8(1) (2016) 82–90.
[76] L. Perini, C. Durante, M. Favaro, V. Perazzolo, S. Agnoli, O. Schneider, G. Granozzi, A. Gennaro, Metal-support interaction in platinum and palladium nanoparticles loaded on nitrogen-doped mesoporous carbon for oxygen reduction reaction, ACS Applied Materials & Interfaces 7(2) (2015) 1170–1179.

[77] C.X. Zhang, J. Hu, X.D. Zhang, X.K. Wang, Y.D. Meng, Certain nitrogen functionalities on carbon nanofiber support for improving platinum performance, Catalysis Today 256 (2015) 193–202.
[78] A. Heydari, H. Gharibi, Fabrication of electrocatalyst based on nitrogen doped graphene as highly efficient and durable support for using in polymer electrolyte fuel cell, Journal of Power Sources 325 (2016) 808–815.
[79] M. Rahsepar, M. Pakshir, H. Kim, Synthesis of multiwall carbon nanotubes with a high loading of Pt by a microwave-assisted impregnation method for use in the oxygen reduction reaction, Electrochimica Acta 108 (2013) 769–775.
[80] A.O. Al-Youbi, J.L. Gomez de la Fuente, F.J. Perez-Alonso, A.Y. Obaid, J.L.G. Fierro, M.A. Pena, M.A. Salam, S. Rojas, Effects of multiwalled carbon nanotube morphology on the synthesis and electrocatalytic performance of Pt supported by multiwalled carbon nanotubes, Applied Catalysis B-Environmental 150 (2014) 21–29.
[81] K. Jukk, N. Kongi, A. Tarre, A. Rosental, A.B. Treshchalov, J. Kozlova, P. Ritslaid, L. Matisen, V. Sammelselg, K. Tammeveski, Electrochemical oxygen reduction behaviour of platinum nanoparticles supported on multi-walled carbon nanotube/titanium dioxide composites, Journal of Electroanalytical Chemistry 735 (2014) 68–76.
[82] K. Jukk, J. Kozlova, P. Ritslaid, V. Sammelselg, N. Alexeyeva, K. Tammeveski, Sputter-deposited Pt nanoparticle/multi-walled carbon nanotube composite catalyst for oxygen reduction reaction, Journal of Electroanalytical Chemistry 708 (2013) 31–38.
[83] S.-H. Wen, S.-G. Cui, L. Shi, R.-P. Liang, J.-D. Qiu, Decoration of carbon nanotubes with highly dispersed platinum nanoparticles for electrocatalytic application, Journal of Electroanalytical Chemistry 738 (2015) 77–83.
[84] M. Sahoo, K. Scott, S. Ramaprabhu, Platinum decorated on partially exfoliated multiwalled carbon nanotubes as high performance cathode catalyst for PEMFG, International Journal of Hydrogen Energy 40(30) (2015) 9435–9443.
[85] C.R.K. Rao, D.C. Trivedi, Chemical and electrochemical depositions of platinum group metals and their applications, Coordination Chemistry Reviews 249(5–6) (2005) 613–631.
[86] S. Dominguez-Dominguez, J.A. Pardilla, A.B. Murcia, E. Morallon, D. Cazorla-Amoros, Electrochemical deposition of platinum nanoparticles on different carbon supports and conducting polymers, Journal of Applied Electrochemistry 38(2) (2008) 259–268.
[87] T.S. Miller, S. Sansuk, S.E. Pei, S.C.S. Lai, J.V. Macpherson, P.R. Unwin, Pt nanoparticle modified single walled carbon nanotube network electrodes for electrocatalysis: Control of the specific surface area over three orders of magnitude, Catalysis Today 244 (2015) 136–145.
[88] E. Negro, R. Latsuzbaia, M. Dieci, I. Boshuizen, G.J.M. Koper, Pt electrodeposited over carbon nano-networks grown on carbon paper as durable catalyst for PEM fuel cells, Applied Catalysis B-Environmental 166 (2015) 155–165.
[89] U.S. Mohanty, Electrodeposition: a versatile and inexpensive tool for the synthesis of nanoparticles, nanorods, nanowires, and nanoclusters of metals, Journal of Applied Electrochemistry 41(3) (2011) 257–270.
[90] B. Geboes, J. Ustarroz, K. Sentosun, H. Vanrompay, A. Hubin, S. Bals, T. Breugelmans, Electrochemical behavior of electrodeposited nanoporous Pt catalysts for the oxygen reduction reaction, ACS Catalysis 6(9) (2016) 5856–5864.

[91] Y. Chen, X.X. Wang, B. Li, X.X. Huang, J.N. Wang, Porous Pt aggregates deposited on a carbon nanotube film with high catalytic activity and durability, Chemelectrochem 3(11) (2016) 1908–1914.
[92] K. Saminathan, V. Kamavaram, V. Veedu, A.M. Kannan, Preparation and evaluation of electrodeposited platinum nanoparticles on in situ carbon nanotubes grown carbon paper for proton exchange membrane fuel cells, International Journal of Hydrogen Energy 34(9) (2009) 3838–3844.
[93] O.K. Alexeeva, V.N. Fateev, Application of the magnetron sputtering for nanostructured electrocatalysts synthesis, International Journal of Hydrogen Energy 41(5) (2016) 3373–3386.
[94] K. Yoshii, K. Yamaji, T. Tsuda, H. Matsumoto, T. Sato, R. Izumi, T. Torimoto, S. Kuwabata, Highly durable Pt nanoparticle-supported carbon catalysts for the oxygen reduction reaction tailored by using an ionic liquid thin layer, Journal of Materials Chemistry A 4(31) (2016) 12152–12157.
[95] K.L. Huang, Y.C. Lai, C.H. Tsai, Effects of sputtering parameters on the performance of electrodes fabricated for proton exchange membrane fuel cells, Journal of Power Sources 156(2) (2006) 224–231.
[96] K. Jukk, N. Alexeyeva, A. Sarapuu, P. Ritslaid, J. Kozlova, V. Sammelselg, K. Tammeveski, Electroreduction of oxygen on sputter-deposited Pd nanolayers on multi-walled carbon nanotubes, International Journal of Hydrogen Energy 38(9) (2013) 3614–3620.
[97] S. Zhang, X.-Z. Yuan, J.N.C. Hin, H. Wang, K.A. Friedrich, M. Schulze, A review of platinum-based catalyst layer degradation in proton exchange membrane fuel cells, Journal of Power Sources 194(2) (2009) 588–600.
[98] D.A. Stevens, J.R. Dahn, Thermal degradation of the support in carbon-supported platinum electrocatalysts for PEM fuel cells, Carbon 43(1) (2005) 179–188.
[99] J. Speder, A. Zana, I. Spanos, J.J.K. Kirkensgaard, K. Mortensen, M. Hanzlik, M. Arenz, Comparative degradation study of carbon supported proton exchange membrane fuel cell electrocatalysts – The influence of the platinum to carbon ratio on the degradation rate, Journal of Power Sources 261 (2014) 14–22.
[100] K.J.J. Mayrhofer, J.C. Meier, S.J. Ashton, G.K.H. Wiberg, F. Kraus, M. Hanzlik, M. Arenz, Fuel cell catalyst degradation on the nanoscale, Electrochemistry Communications 10(8) (2008) 1144–1147.
[101] L. Castanheira, W.O. Silva, F.H.B. Lima, A. Crisci, L. Dubau, F. Maillard, Carbon corrosion in proton-exchange membrane fuel cells: Effect of the carbon structure, the degradation protocol, and the gas atmosphere, ACS Catalysis 5(4) (2015) 2184–2194.
[102] I. Katsounaros, S. Cherevko, A.R. Zeradjanin, K.J.J. Mayrhofer, Oxygen electrochemistry as a cornerstone for sustainable energy conversion, Angewandte Chemie-International Edition 53(1) (2014) 102–121.
[103] T. Asset, R. Chattot, M. Fontana, B. Mercier-Guyon, N. Job, L. Dubau, F. Maillard, A review on recent developments and prospects for the oxygen reduction reaction on hollow Pt-alloy nanoparticles, Chemphyschem 19(13) (2018) 1552–1567.
[104] J.W. Ma, A. Habrioux, C. Morais, A. Lewera, W. Vogel, Y. Verde-Gomez, G. Ramos-Sanchez, P.B. Balbuena, N. Alonso-Vante, Spectroelectrochemical probing of the strong interaction between platinum nanoparticles and graphitic domains of carbon, ACS Catalysis 3(9) (2013) 1940–1950.

[105] A. Lewera, L. Timperman, A. Roguska, N. Alonso-Vante, Metal-support interactions between nanosized Pt and metal oxides (WO_3 and TiO_2) studied using X-ray photoelectron spectroscopy, Journal of Physical Chemistry C 115(41) (2011) 20153–20159.
[106] N.R. Elezovic, V.R. Radmilovic, N.V. Krstajic, Platinum nanocatalysts on metal oxide based supports for low temperature fuel cell applications, RSC Advances 6(8) (2016) 6788–6801.
[107] T. Binninger, E. Fabbri, R. Kotz, T.J. Schmidt, Determination of the electrochemically active surface area of metal-oxide supported platinum catalyst, Journal of the Electrochemical Society 161(3) (2014) H121-H128.
[108] Y. Luo, N. Alonso-Vante, The effect of support on advanced pt-based cathodes towards the oxygen reduction reaction. State of the art, Electrochimica Acta 179 (2015) 108–118.
[109] L. Timperman, N. Alonso-Vante, Oxide substrate effect toward electrocatalytic enhancement of platinum and ruthenium-selenium catalysts, Electrocatalysis 2(3) (2011) 181–191.
[110] P.S.M. Kumar, V.K. Ponnusamy, K.R. Deepthi, G. Kumar, A. Pugazhendhi, H. Abe, S. Thiripuranthagan, U. Pal, S.K. Krishnan, Controlled synthesis of Pt nanoparticle supported TiO_2 nanorods as efficient and stable electrocatalysts for the oxygen reduction reaction, Journal of Materials Chemistry A 6(46) (2018) 23435–23444.
[111] L. Zhang, L.Y. Wang, C.M.B. Holt, B. Zahiri, Z. Li, K. Malek, T. Navessin, M.H. Eikerling, D. Mitlin, Highly corrosion resistant platinum-niobium oxide-carbon nanotube electrodes for the oxygen reduction in PEM fuel cells, Energy & Environmental Science 5(3) (2012) 6156–6172.
[112] C. Gebauer, D. Hoffmann, Z. Jusys, R.J. Behm, Novel, Highly Conductive Pt/TiO_2 thin-film model catalyst electrodes: The role of metal-support interactions, Chemelectrochem 3(10) (2016) 1553–1563.
[113] S. von Kraemer, J. Wikander, G. Lindbergh, A. Lundblad, A.E.C. Palmqvist, Evaluation of TiO_2 as catalyst support in $Pt\text{-}TiO_2/C$ composite cathodes for the proton exchange membrane fuel cell, Journal of Power Sources 180(1) (2008) 185–190.
[114] G. Cognard, G. Ozouf, C. Beauger, G. Berthome, D. Riassetto, L. Dubau, R. Chattot, M. Chatenet, F. Maillard, Benefits and limitations of Pt nanoparticles supported on highly porous antimony-doped tin dioxide aerogel as alternative cathode material for proton-exchange membrane fuel cells, Applied Catalysis B-Environmental 201 (2017) 381–390.
[115] M. Nakada, A. Ishihara, S. Mitsushima, N. Kamiya, K. Ota, Effect of tin oxides on oxide formation and reduction of platinum particles, Electrochemical and Solid State Letters 10(1) (2007) F1-F4.
[116] P. Zhang, S.Y. Huang, B.N. Popov, Mesoporous tin oxide as an oxidation-resistant catalyst support for proton exchange membrane fuel cells, Journal of the Electrochemical Society 157(8) (2010) B1163-B1172.
[117] H. Chhina, S. Campbell, O. Kesler, Ex situ evaluation of tungsten oxide as a catalyst support for PEMFCs, Journal of the Electrochemical Society 154(6) (2007) B533-B539.
[118] B. Rajesh, V. Karthik, S. Karthikeyan, K.R. Thampi, J.M. Bonard, B. Viswanathan, $Pt\text{-}WO_3$ supported on carbon nanotubes as possible anodes for direct methanol fuel cells, Fuel 81(17) (2002) 2177–2190.

[119] L.A. Estudillo-Wong, Y. Luo, J.A. Diaz-Real, N. Alonso-Vante, Enhanced oxygen reduction reaction stability on platinum nanoparticles photo-deposited onto oxide-carbon composites, Applied Catalysis B-Environmental 187 (2016) 291–300.
[120] B. Ruiz Camacho, C. Morais, M.A. Valenzuela, N. Alonso-Vante, Enhancing oxygen reduction reaction activity and stability of platinum via oxide-carbon composites, Catalysis Today 202 (2013) 36–43.
[121] Y. Jeon, Y. Ji, Y.I. Cho, C. Lee, D.H. Park, Y.G. Shul, Oxide-carbon nanofibrous composite support for a highly active and stable polymer electrolyte membrane fuel-cell catalyst, ACS Nano 12(7) (2018) 6819–6829.
[122] P. Dhanasekaran, S.V. Selvaganesh, L. Sarathi, S.D. Bhat, Rutile TiO_2 supported Pt as stable electrocatalyst for improved oxygen reduction reaction and durability in polymer electrolyte fuel cells, Electrocatalysis 7(6) (2016) 495–506.
[123] D.S. Kim, E.F.A. Zeid, Y.T. Kim, Additive treatment effect of TiO_2 as supports for Pt-based electrocatalysts on oxygen reduction reaction activity, Electrochimica Acta 55(11) (2010) 3628–3633.
[124] M. Gustavsson, H. Ekstrom, R. Hanarp, L. Eurenius, G. Lindbergh, E. Olsson, B. Kasemo, Thin film Pt/TiO_2 catalysts for the polymer electrolyte fuel cell, Journal of Power Sources 163(2) (2007) 671–678.
[125] N. Rajalakshmi, N. Lakshmi, K.S. Dhathathreyan, Nano titanium oxide catalyst support for proton exchange membrane fuel cells, International Journal of Hydrogen Energy 33(24) (2008) 7521–7526.
[126] F. Ando, T. Tanabe, T. Gunji, T. Tsuda, S. Kaneko, T. Takeda, T. Ohsaka, F. Matsumoto, Improvement of ORR activity and durability of Pt electrocatalyst nanoparticles anchored on TiO_2/cup-stacked carbon nanotube in acidic aqueous media, Electrochimica Acta 232 (2017) 404–413.
[127] N. Alonso-Vante, L.A. Estudillo-Wong, G. Ramos-Sanchez, L. Calvillo, G. Granozzi, The support interaction effect on platinum nanoparticles on non-, Y-, Ce-doped anatase and its implication on the ORR in acid and alkaline media, ChemElectroChem 4(12) (2017) 3264–3275.
[128] K. Tiido, N. Alexeyeva, M. Couillard, C. Bock, B.R. MacDougall, K. Tammeveski, Graphene-TiO_2 composite supported Pt electrocatalyst for oxygen reduction reaction, Electrochimica Acta 107 (2013) 509–517.
[129] B. Ruiz-Camacho, O. Martinez-Alvarez, H.H. Rodriguez-Santoyo, V. Granados-Alejo, Pt/C and Pt/TiO_2-C electrocatalysts prepared by chemical vapor deposition with high tolerance to alcohols in oxygen reduction reaction, Journal of Electroanalytical Chemistry 725 (2014) 19–24.
[130] Y. Ji, Y.I. Cho, Y. Jeon, C. Lee, D.H. Park, Y.G. Shul, Design of active Pt on TiO_2 based nanofibrous cathode for superior PEMFC performance and durability at high temperature, Applied Catalysis B-Environmental 204 (2017) 421–429.
[131] Y. Zhao, Y. Wang, J. Zang, J. Lu, X. Xu, A novel support of nano titania modified graphitized nanodiamond for Pt electrocatalyst in direct methanol fuel cell, International Journal of Hydrogen Energy 40(13) (2015) 4540–4547.
[132] S. Chung, M. Choun, B. Jeong, J.K. Lee, J. Lee, Atomic layer deposition of ultrathin layered TiO_2 on Pt/C cathode catalyst for extended durability in polymer electrolyte fuel cells, Journal of Energy Chemistry 25(2) (2016) 258–264.
[133] X. Sun, M. Xie, J.J. Travis, G.K. Wang, H.T. Sun, J. Lian, S.M. George, Pseudocapacitance of amorphous TiO_2 thin films anchored to graphene and carbon

nanotubes using atomic layer deposition, Journal of Physical Chemistry C 117(44) (2013) 22497–22508.
[134] S.R. Deng, S.W. Verbruggen, Z.B. He, D.J. Cott, P.M. Vereecken, J.A. Martens, S. Bals, S. Lenaerts, C. Detavernier, Atomic layer deposition-based synthesis of photoactive TiO_2 nanoparticle chains by using carbon nanotubes as sacrificial templates, RSC Advances 4(23) (2014) 11648–11653.
[135] L. Acauan, A.C. Dias, M.B. Pereira, F. Horowitz, C.P. Bergmann, Influence of different defects in vertically aligned carbon nanotubes on TiO_2 nanoparticle formation through atomic layer deposition, ACS Applied Materials & Interfaces 8(25) (2016) 16444–16450.
[136] R.A. Fisher, M.R. Watt, R. Konjeti, W.J. Ready, Atomic layer deposition of titanium oxide for pseudocapacitive functionalization of vertically-aligned carbon nanotube supercapacitor electrodes, ECS Journal of Solid State Science and Technology 4(2) (2015) M1-M5.
[137] C. Guerra-Nunez, Y.C. Zhang, M. Li, V. Chawla, R. Erni, J. Michler, H.G. Park, I. Utke, Morphology and crystallinity control of ultrathin TiO_2 layers deposited on carbon nanotubes by temperature-step atomic layer deposition, Nanoscale 7(24) (2015) 10622–10633.
[138] Y. Chen, J. Wang, X. Meng, Y. Zhong, R. Li, X. Sun, S. Ye, S. Knights, Atomic layer deposition assisted Pt-SnO_2 hybrid catalysts on nitrogen-doped CNTs with enhanced electrocatalytic activities for low temperature fuel cells, International Journal of Hydrogen Energy 36(17) (2011) 11085–11092.
[139] Y. Senoo, K. Taniguchi, K. Kakinuma, M. Uchida, H. Uchida, S. Deki, M. Watanabe, Cathodic performance and high potential durability of Ta-SnO_2–δ-supported Pt catalysts for PEFC cathodes, Electrochemistry Communications 51 (2015) 37–40.
[140] M. Yin, J. Xu, Q. Li, J.O. Jensen, Y. Huang, L.N. Cleemann, N.J. Bjerrum, W. Xing, Highly active and stable Pt electrocatalysts promoted by antimony-doped SnO_2 supports for oxygen reduction reactions, Applied Catalysis B: Environmental 144 (2014) 112–120.
[141] T. Daio, A. Staykov, L. Guo, J. Liu, M. Tanaka, S. Matthew Lyth, K. Sasaki, Lattice strain mapping of platinum nanoparticles on carbon and SnO_2 supports, Scientific Reports 5 (2015) 13126.
[142] R. Mohamed, T. Binninger, P.J. Kooyman, A. Hoell, E. Fabbri, A. Patru, A. Heinritz, T.J. Schmidt, P. Levecque, Facile deposition of Pt nanoparticles on Sb-doped SnO_2 support with outstanding active surface area for the oxygen reduction reaction, Catalysis Science & Technology 8(10) (2018) 2672–2685.
[143] A. Rabis, T. Binninger, E. Fabbri, T.J. Schmidt, Impact of Support Physico-chemical Properties on the CO oxidation and the oxygen reduction reaction activity of Pt/SnO_2 electrocatalysts, Journal of Physical Chemistry C 122(9) (2018) 4739–4746.
[144] T. Tsukatsune, Y. Takabatake, Z. Noda, T. Daio, A. Zaitsu, S.M. Lyth, A. Hayashi, K. Sasaki, Platinum-decorated tin oxide and niobium-doped tin oxide PEFC electrocatalysts: Oxygen reduction reaction activity, Journal of the Electrochemical Society 161(12) (2014) F1208-F1213.
[145] F. Labbé, T. Asset, M. Chatenet, Y. Ahmad, K. Guérin, R. Metkemeijer, S. Berthon-Fabry, Activity and durability of platinum-based electrocatalysts with tin oxide–coated carbon aerogel materials as catalyst supports, Electrocatalysis (2019).

[146] N. Zhang, S. Zhang, C.Y. Du, Z.B. Wang, Y.Y. Shao, F.D. Kong, Y.H. Lin, G.P. Yin, Pt/Tin oxide/carbon nanocomposites as promising oxygen reduction electrocatalyst with improved stability and activity, Electrochimica Acta 117 (2014) 413–419.
[147] M. Maicu, M.C. Hidalgo, G. Colon, J.A. Navio, Comparative study of the photodeposition of Pt, Au and Pd on pre-sulphated TiO_2 for the photocatalytic decomposition of phenol, Journal of Photochemistry and Photobiology A-Chemistry 217(2–3) (2011) 275–283.
[148] J.W. Ma, A. Habrioux, N. Alonso-Vante, Enhanced HER and ORR behavior on photodeposited Pt nanoparticles onto oxide-carbon composite, Journal of Solid State Electrochemistry 17(7) (2013) 1913–1921.
[149] K. Wenderich, G. Mul, Methods, mechanism, and applications of photodeposition in photocatalysis: A review, Chemical Reviews 116(23) (2016) 14587–14619.
[150] L. Timperman, A. Lewera, W. Vogel, N. Alonso-Vante, Nanostructured platinum becomes alloyed at oxide-composite substrate, Electrochemistry Communications 12(12) (2010) 1772–1775.
[151] I. Kruusenberg, N. Alexeyeva, K. Tammeveski, J. Kozlova, L. Matisen, V. Sammelselg, J. Solla-Gullon, J.M. Feliu, Effect of purification of carbon nanotubes on their electrocatalytic properties for oxygen reduction in acid solution, Carbon 49(12) (2011) 4031–4039.
[152] W.S. Hummers, R.E. Offeman, Preparation of graphitic oxide, Journal of the American Chemical Society 80(6) (1958) 1339–1339.
[153] D.C. Marcano, D.V. Kosynkin, J.M. Berlin, A. Sinitskii, Z.Z. Sun, A. Slesarev, L.B. Alemany, W. Lu, J.M. Tour, Improved synthesis of graphene oxide, ACS Nano 4(8) (2010) 4806–4814.
[154] A. Treshchalov, S. Tsarenko, T. Avarmaa, R. Saar, A. Lohmus, A. Vanetsev, I. Sildos, He/H_2 pulsed-discharge plasma as a tool for synthesis of surfactant-free colloidal silver nanoparticles in water, 6(1) (2016) 85–100.
[155] G. Sievers, A. Quade, A. Kruth, V. Brueser, Combined balanced magnetron sputtering and substrate-annealing synthesis for Pt and Pt/C oxygen reduction catalysts, Journal of the Electrochemical Society 163(5) (2016) F341-F346.
[156] M. Ristic, M. Ivanda, S. Popovic, S. Music, Dependence of nanocrystalline SnO_2 particle size on synthesis route, Journal of Non-Crystalline Solids 303(2) (2002) 270–280.
[157] C.A. Campos-Roldán, G. Ramos-Sánchez, R.G. Gonzalez-Huerta, J.R. Vargas García, P.B. Balbuena, N. Alonso-Vante, Influence of sp^3–sp^2 carbon nanodomains on metal/support interaction, catalyst durability, and catalytic activity for the oxygen reduction reaction, ACS Applied Materials & Interfaces 8(35) (2016) 23260–23269.
[158] S. Grazulis, D. Chateigner, R.T. Downs, A.F. Yokochi, M. Quiros, L. Lutterotti, E. Manakova, J. Butkus, P. Moeck, A. Le Bail, Crystallography open database - an open-access collection of crystal structures, J Appl Crystallogr 42(Pt 4) (2009) 726–729.
[159] L. Lutterotti, Total pattern fitting for the combined size–strain–stress–texture determination in thin film diffraction, Nuclear Instruments and Methods in Physics Research Section B: Beam Interactions with Materials and Atoms 268(3) (2010) 334–340.

[160] J. Solla-Gullon, V. Montiel, A. Aldaz, J. Clavilier, Electrochemical characterisation of platinum nanoparticles prepared by microemulsion: how to clean them without loss of crystalline surface structure, Journal of Electroanalytical Chemistry 491(1–2) (2000) 69–77.
[161] E.G. Ciapina, S.F. Santos, E.R. Gonzalez, Electrochemical CO stripping on nanosized Pt surfaces in acid media: A review on the issue of peak multiplicity, Journal of Electroanalytical Chemistry 815 (2018) 47–60.
[162] R. Sharma, K.K. Kar, Hierarchically structured catalyst layer for the oxygen reduction reaction fabricated by electrodeposition of platinum on carbon nanotube coated carbon fiber, RSC Advances 5(82) (2015) 66518–66527.
[163] C.P. Huang, C.B. Odetola, M. Rodgers, Nanoparticle seeded pulse electrodeposition for preparing high performance Pt/C electrocatalysts, Applied Catalysis A-General 499 (2015) 55–65.
[164] R.Q. Yu, L.W. Chen, Q.P. Liu, J.Y. Lin, K.L. Tan, S.C. Ng, H.S.O. Chan, G.Q. Xu, T.S.A. Hor, Platinum deposition on carbon nanotubes via chemical modification, Chemistry of Materials 10(3) (1998) 718–722.
[165] A. Afraz, A.A. Rafati, A. Hajian, M. Khoshnood, Electrodeposition of Pt nanoparticles on new porous graphitic carbon nanostructures prepared from biomass for fuel cell and methanol sensing applications, Electrocatalysis 6(2) (2015) 220–228.
[166] S. Woo, J. Lee, S.K. Park, H. Kim, T.D. Chung, Y.Z. Piao, Electrochemical codeposition of Pt/graphene catalyst for improved methanol oxidation, Current Applied Physics 15(3) (2015) 219–225.
[167] G.V. Fortunato, F. de Lima, G. Maia, Oxygen-reduction reaction strongly electrocatalyzed by Pt electrodeposited onto graphene or graphene nanoribbons, Journal of Power Sources 302 (2016) 247–258.
[168] W.Y. Zhang, Z.X. Wang, Y. Shen, M.Y. Xi, X. Chu, C.Y. Xi, Graphene supported platinum nanoparticles as catalyst for oxygen reduction reaction, Chemical Research in Chinese Universities 31(6) (2015) 1007–1011.
[169] J. Solla-Gullon, E. Lafuente, A. Aldaz, M.T. Martinez, J.M. Feliu, Electrochemical characterization and reactivity of Pt nanoparticles supported on single-walled carbon nanotubes, Electrochimica Acta 52(18) (2007) 5582–5590.
[170] A. Lopez-Cudero, J. Solla-Gullon, E. Herrero, A. Aldaz, J.M. Feliu, CO electrooxidation on carbon supported platinum nanoparticles: Effect of aggregation, Journal of Electroanalytical Chemistry 644(2) (2010) 117–126.
[171] A. Cuesta, A. Couto, A. Rincon, M.C. Perez, A. Lopez-Cudero, C. Gutierrez, Potential dependence of the saturation CO coverage of Pt electrodes: The origin of the pre-peak in CO-stripping voltammograms. Part 3: Pt(poly), Journal of Electroanalytical Chemistry 586(2) (2006) 184–195.
[172] N.P. Lebedeva, M.T.M. Koper, E. Herrero, J.M. Feliu, R.A. van Santen, CO oxidation on stepped Pt n(111) x (111) electrodes, Journal of Electroanalytical Chemistry 487(1) (2000) 37–44.
[173] N.P. Lebedeva, M.T.M. Koper, J.M. Feliu, R.A. van Santen, Role of crystalline defects in electrocatalysis: Mechanism and kinetics of CO adlayer oxidation on stepped platinum electrodes, Journal of Physical Chemistry B 106(50) (2002) 12938–12947.
[174] J. Solla-Gullon, F.J. Vidal-Iglesias, E. Herrero, J.M. Feliu, A. Aldaz, CO monolayer oxidation on semi-spherical and preferentially oriented (100) and (111) platinum nanoparticles, Electrochemistry Communications 8(1) (2006) 189–194.

[175] J.H. Kim, J.Y. Cheon, T.J. Shin, J.Y. Park, S.H. Joo, Effect of surface oxygen functionalization of carbon support on the activity and durability of Pt/C catalysts for the oxygen reduction reaction, Carbon 101 (2016) 449–457.
[176] J. Solla-Gullon, A. Rodes, V. Montiel, A. Aldaz, J. Clavilier, Electrochemical characterisation of platinum-palladium nanoparticles prepared in a water-in-oil microemulsion, Journal of Electroanalytical Chemistry 554 (2003) 273–284.
[177] R.R. Adžić, J. Wang, B.M. Ocko, Structure of metal adlayers during the course of electrocatalytic reactions: O_2 reduction on Au(111) with Tl adlayers in acid solutions, Electrochimica Acta 40(1) (1995) 83–89.
[178] D.R. Lide, CRC handbook of chemistry and physics, CRC Press, Boca Raton, 2001.
[179] A. Damjanovic, V. Brusic, Electrode kinetics of oxygen reduction on oxide-free platinum electrodes, Electrochimica Acta 12(6) (1967) 615–628.
[180] H.A. Gasteiger, S.S. Kocha, B. Sompalli, F.T. Wagner, Activity benchmarks and requirements for Pt, Pt-alloy, and non-Pt oxygen reduction catalysts for PEMFCs, Applied Catalysis B-Environmental 56(1–2) (2005) 9–35.
[181] R. Gomez, J.M. Orts, B. Alvarez-Ruiz, J.M. Feliu, Effect of temperature on hydrogen adsorption on Pt(111), Pt(110), and Pt(100) electrodes in 0.1 M $HClO_4$, Journal of Physical Chemistry B 108(1) (2004) 228–238.
[182] R.E. Davis, G.L. Horvath, C.W. Tobias, The solubility and diffusion coefficient of oxygen in potassium hydroxide solutions, Electrochimica Acta 12(3) (1967) 287–297.
[183] K. Jukk, N. Kongi, P. Rauwel, L. Matisen, K. Tammeveski, Platinum nanoparticles supported on nitrogen-doped graphene nanosheets as electrocatalysts for oxygen reduction reaction, Electrocatalysis 7(5) (2016) 428–440.
[184] Y. Qin, L. Chao, J. Yuan, Y. Liu, F.Q. Chu, Y. Kong, Y.X. Tao, M.L. Liu, Ultrafine Pt nanoparticle-decorated robust 3D N-doped porous graphene as an enhanced electrocatalyst for methanol oxidation, Chemical Communications 52(2) (2016) 382–385.
[185] C.T. Pan, L.H. Qiu, Y.J. Peng, F. Yan, Facile synthesis of nitrogen-doped carbon-Pt nanoparticle hybrids via carbonization of poly ([Bvim][Br] co-acrylonitrile) for electrocatalytic oxidation of methanol, Journal of Materials Chemistry 22(27) (2012) 13578–13584.
[186] N. Seselj, C. Engelbrekt, J.D. Zhang, Graphene-supported platinum catalysts for fuel cells, Science Bulletin 60(9) (2015) 864–876.
[187] Y. Liu, Y.X. Xia, H.Y. Yang, Y.S. Zhang, M.J. Zhao, G.T. Pan, Facile preparation of high-quality Pt/reduced graphene oxide nanoscrolls for methanol oxidation, Nanotechnology 24(23) (2013).
[188] H. Kim, K. Lee, S.I. Woo, Y. Jung, On the mechanism of enhanced oxygen reduction reaction in nitrogen-doped graphene nanoribbons, Physical Chemistry Chemical Physics 13(39) (2011) 17505–17510.
[189] K.S. Han, Y.-S. Moon, O.H. Han, K.J. Hwang, I. Kim, H. Kim, Heat treatment and potential cycling effects on surface morphology, particle size, and catalytic activity of Pt/C catalysts studied by C-13 NMR, TEM, XRD and CV, Electrochemistry Communications 9(2) (2007) 317–324.
[190] E. Antolini, Formation, microstructural characteristics and stability of carbon supported platinum catalysts for low temperature fuel cells, Journal of Materials Science 38(14) (2003) 2995–3005.

[191] A.H. Alexopoulos, A.I. Roussos, C. Kiparissides, Part I: Dynamic evolution of the particle size distribution in particulate processes undergoing combined particle growth and aggregation, Chemical Engineering Science 59(24) (2004) 5751–5769.
[192] D.Y. Chung, Y.-H. Chung, N. Jung, K.-H. Choi, Y.-E. Sung, Correlation between platinum nanoparticle surface rearrangement induced by heat treatment and activity for an oxygen reduction reaction, Physical Chemistry Chemical Physics 15(32) (2013) 13658–13663.
[193] X. Jiang, T. Shen, H. Li, L. Wang, Q. Yue, J. Liu, Effects of heat treatment temperature and atmosphere on electrocatalytic properties of platinum nanocrystals, Journal of Electroanalytical Chemistry 729 (2014) 53–60.
[194] F. Maillard, M. Eikerling, O.V. Cherstiouk, S. Schreier, E. Savinova, U. Stimming, Size effects on reactivity of Pt nanoparticles in CO monolayer oxidation: The role of surface mobility, Faraday Discussions 125 (2004) 357–377.
[195] Y. Zhang, H. Liu, H. Wu, Z. Sun, L. Qian, Facile synthesis of Pt nanoparticles loaded porous graphene towards oxygen reduction reaction, Materials & Design 96 (2016) 323–328.
[196] N.M. Markovic, H.A. Gasteiger, N. Philip, Oxygen reduction on platinum low-index single-crystal surfaces in alkaline solution: Rotating ring disk(Pt(hkl)) studies, Journal of Physical Chemistry 100(16) (1996) 6715–6721.
[197] Y.R. Wang, J. Clancey, G.X. Lu, J.R. Liu, L.L. Liu, J. Chaudhuri, S. George, M. Xie, S.Y. Wei, Z.H. Guo, Enhanced methanol oxidation with annealed atomic layer deposited platinum nanoparticles on carbon nanotubes, Journal of the Electrochemical Society 163(2) (2016) F1-F10.
[198] Y. Su, M. Feng, C. Zhang, Z. Yan, H. Liu, J. Tang, H. Du, Platinum nanowires: Structural and catalytic evolution upon annealing temperature, Electrochimica Acta 164 (2015) 182–186.
[199] E. Antolini, Structural parameters of supported fuel cell catalysts: The effect of particle size, inter-particle distance and metal loading on catalytic activity and fuel cell performance, Applied Catalysis B-Environmental 181 (2016) 298–313.
[200] C.W.B. Bezerra, L. Zhang, H. Liu, K. Lee, A.L.B. Marques, E.P. Marques, H. Wang, J. Zhang, A review of heat-treatment effects on activity and stability of PEM fuel cell catalysts for oxygen reduction reaction, Journal of Power Sources 173(2) (2007) 891–908.
[201] K. Kinoshita, Particle-size effects for oxygen reduction on highly dispersed platinum in acid electrolytes, Journal of the Electrochemical Society 137(3) (1990) 845–848.
[202] M.H. Shao, A. Peles, K. Shoemaker, Electrocatalysis on platinum nanoparticles: Particle size effect on oxygen reduction reaction activity, Nano Letters 11(9) (2011) 3714–3719.
[203] E. Antolini, F. Cardellini, E. Giacometti, G. Squadrito, Study on the formation of Pt/C catalysts by non-oxidized active carbon support and a sulfur-based reducing agent, Journal of Materials Science 37(1) (2002) 133–139.
[204] K. Shinozaki, Y. Morimoto, B.S. Pivovar, S.S. Kocha, Re-examination of the Pt particle size effect on the oxygen reduction reaction for ultrathin uniform Pt/C catalyst layers without influence from nafion, Electrochimica Acta 213(20) (2016) 783–790.

[205] M. Peuckert, T. Yoneda, R.A.D. Betta, M. Boudart, Oxygen reduction on small supported platinum particles, Journal of the Electrochemical Society 133(5) (1986) 944–947.
[206] M.L. Sattler, P.N. Ross, The surface-structure of Pt crystallites supported on carbon-black, Ultramicroscopy 20(1–2) (1986) 21–28.
[207] F.J. Perez-Alonso, D.N. McCarthy, A. Nierhoff, P. Hernandez-Fernandez, C. Strebel, I.E.L. Stephens, J.H. Nielsen, I. Chorkendorff, The effect of size on the oxygen electroreduction activity of mass-selected platinum nanoparticles, Angewandte Chemie-International Edition 51(19) (2012) 4641–4643.
[208] C. Zhang, H. Yu, Y. Li, L. Fu, Y. Gao, W. Song, Z. Shao, B. Yi, Simple synthesis of Pt/TiO_2 nanotube arrays with high activity and stability, Journal of Electroanalytical Chemistry 701 (2013) 14–19.
[209] K. Tammeveski, T. Tenno, A. Rosental, P. Talonen, L.S. Johansson, L. Niinisto, The reduction of oxygen on Pt-TiO_2 coated Ti electrodes in alkaline solution, Journal of the Electrochemical Society 146(2) (1999) 669–676.
[210] F. Maillard, E.R. Savinova, U. Stimming, CO monolayer oxidation on Pt nanoparticles: Further insights into the particle size effects, Journal of Electroanalytical Chemistry 599(2) (2007) 221–232.
[211] D.K. Huang, B.Y. Zhang, J. Bai, Y.B. Zhang, G. Wittstock, M.K. Wang, Y. Shen, Pt catalyst supported within TiO_2 mesoporous films for oxygen reduction reaction, Electrochimica Acta 130 (2014) 97–103.
[212] C.H. Yao, F. Li, X. Li, D.G. Xia, Fiber-like nanostructured Ti_4O_7 used as durable fuel cell catalyst support in oxygen reduction catalysis, Journal of Materials Chemistry 22(32) (2012) 16560–16565.
[213] R. Alipour Moghadam Esfahani, A.H.A. Monteverde Videla, S. Vankova, S. Specchia, Stable and methanol tolerant Pt/TiO_x-C electrocatalysts for the oxygen reduction reaction, International Journal of Hydrogen Energy 40(42) (2015) 14529–14539.
[214] A.L. Ong, K.K. Inglis, D.K. Whelligan, S. Murphy, J.R. Varcoe, Effect of cationic molecules on the oxygen reduction reaction on fuel cell grade Pt/C (20 wt%) catalyst in potassium hydroxide (aq, 1 mol dm^{-3}), Physical Chemistry Chemical Physics 17(18) (2015) 12135–12145.
[215] T.T.H. Van, C.J. Pan, J. Rick, W.N. Su, B.J. Hwang, Nanostructured $Ti_{0.7}Mo_{0.3}O_2$ support enhances electron transfer to Pt: High-performance catalyst for oxygen reduction reaction, Journal of the American Chemical Society 133(30) (2011) 11716–11724.
[216] N.R. Elezovic, B.M. Babic, V.R. Radmilovic, L.M. Vracar, N.V. Krstajic, Nb–TiO_2 supported platinum nanocatalyst for oxygen reduction reaction in alkaline solutions, Electrochimica Acta 56(25) (2011) 9020–9026.
[217] K. Tammeveski, T. Tenno, J. Claret, C. Ferrater, Electrochemical reduction of oxygen on thin-film Pt electrodes in 0.1 M KOH, Electrochimica Acta 42(5) (1997) 893–897.
[218] J. Tymoczko, F. Calle-Vallejo, W. Schuhmann, A.S. Bandarenka, Making the hydrogen evolution reaction in polymer electrolyte membrane electrolysers even faster, Nature Communications 7 (2016).
[219] A. Ganassin, V. Colic, J. Tymoczko, A.S. Bandarenka, W. Schuhmann, Non-covalent interactions in water electrolysis: influence on the activity of Pt(111) and iridium oxide catalysts in acidic media, Physical Chemistry Chemical Physics 17(13) (2015) 8349–8355.

[220] N.S. Veizaga, V.I. Rodriguez, T.A. Rocha, M. Bruno, O.A. Scelza, S.R. de Miguel, E.R. Gonzalez, Promoting effect of tin in platinum electrocatalysts for direct methanol fuel cells (DMFC), Journal of the Electrochemical Society 162(3) (2015) F243-F249.
[221] I. Borbath, D. Guban, Z. Paszti, I.E. Sajo, E. Drotar, J.L.G. de la Fuente, T. Herranz, S. Rojas, A. Tompos, Controlled synthesis of Pt_3Sn/C electrocatalysts with exclusive Sn-Pt interaction designed for use in direct methanol fuel cells, Topics in Catalysis 56(11) (2013) 1033–1046.
[222] H.L. Huang, A.A.A. Nassr, V. Celorrio, S.F.R. Taylor, V.K. Puthiyapura, C. Hardacre, D.J.L. Brett, A.E. Russell, Effects of heat treatment atmosphere on the structure and activity of Pt_3Sn nanoparticle electrocatalysts: a characterisation case study, Faraday Discussions 208 (2018) 555–573.
[223] H.A. Gasteiger, N. Markovic, P.N. Ross, E.J. Cairns, Methanol electrooxidation on well-characterized Pt-Rn alloys, Journal of Physical Chemistry 97(46) (1993) 12020–12029.
[224] Y. Wang, G. Wang, G. Li, B. Huang, J. Pan, Q. Liu, J. Han, L. Xiao, J. Lu, L. Zhuang, Pt–Ru catalyzed hydrogen oxidation in alkaline media: Oxophilic effect or electronic effect?, Energy & Environmental Science 8(1) (2015) 177–181.
[225] L.A. Estudillo-Wong, Y. Luo, J.A. Díaz-Real, N. Alonso-Vante, Enhanced oxygen reduction reaction stability on platinum nanoparticles photo-deposited onto oxide-carbon composites, Applied Catalysis B: Environmental 187 (2016) 291–300.
[226] R. Rizo, M.J. Lazaro, E. Pastor, G. Garcia, Spectroelectrochemical study of carbon monoxide and ethanol oxidation on Pt/C, PtSn(3:1)/C and PtSn(1:1)/C catalysts, Molecules 21(9) (2016).
[227] L. Timperman, Y. Luo, N. Alonso-Vante, On the availability of active sites for the hydrogen peroxide and oxygen reduction reactions on highly dispersed platinum nanoparticles, ChemElectroChem 3(10) (2016) 1705–1712.
[228] Z.H. Zhang, J. Liu, J.J. Gu, L. Su, L.F. Cheng, An overview of metal oxide materials as electrocatalysts and supports for polymer electrolyte fuel cells, Energy & Environmental Science 7(8) (2014) 2535–2558.
[229] F.J. Perez-Alonso, C.F. Elkjaer, S.S. Shim, B.L. Abrams, I.E.L. Stephens, I. Chorkendorff, Identical locations transmission electron microscopy study of Pt/C electrocatalyst degradation during oxygen reduction reaction, Journal of Power Sources 196(15) (2011) 6085–6091.
[230] G. Ozouf, G. Cognard, F. Maillard, M. Chatenet, L. Guetaz, M. Heitzmann, P.A. Jacques, C. Beauger, Sb-Doped SnO_2 aerogels based catalysts for proton exchange membrane fuel cells: Pt deposition routes, electrocatalytic activity and durability, Journal of the Electrochemical Society 165(6) (2018) F3036–F3044.

9. SUMMARY IN ESTONIAN

Hapniku elektrokeemiline redutseerumine Pt katalüsaatoritel

Käesolevas doktoritöös uuriti hapniku elektrokeemilist redutseerumist erinevatel süsinikmaterjalidel ja metallioksiidide-süsinikmaterjalide komposiitidel põhinevatel plaatinakatalüsaatoritel happelises ja aluselises lahuses kasutades pöörleva ketaselektroodi meetodit. Plaatina sadestamiseks alusmaterjalile kasutati erinevaid meetodeid, näiteks elektrosadestus, etüleenglükooli meetod, He/H_2 plasma, magnetrontolmustamine, CO meetod ja fotokeemiline sadestus. Metalloksiid-süsinik materjali komposiidid valmistati aatomkihtsadestuse ja sool-geel meetoditega.

Töö esimeses osas uuriti hapniku redutseerumist süsiniknanotorudele elektrokeemiliselt sadestatud Pt nanoosakestel 0,05 M H_2SO_4 lahuses. Pt elektrosadestamiseks kasutati kahte erinevat potentsiaali ja erinevat arvu potentsiaali impulsse (100–1500). Sellisel viisil valmistatud katalüsaatorid näitasid kõrgemat eriaktiivsust kui kommertsiaalne 20% Pt/C. Koutecky-Levichi analüüs näitas, et üleminevate elektronide arv hapniku molekuli kohta oli 4. Tafeli analüüs näitas, et esimese elektroni ülekanne hapniku molekulile on kiirust limiteerivaks staadiumiks neil katalüsaatoritel.

Teises osas uuriti elektrokatalüütilist aktiivsust ja pikaaegset stabiilsust 0,1 M KOH lahuses Pt nanoosakestel, mis olid sadestatud nitrobenseeniga modifitseeritud grafeenile. Valmistatud katalüsaatorid näitasid suurt aktiivsust O_2 redutseerumisel, kusjuures poollainepotentsiaal ja eriaktiivsus olid sarnased kommertsiaalsele 20% Pt/C katalüsaatorile. Stabiilsustest näitas, et uuritud materjal oli pikas perspektiivis stabiilne.

Seejärel uuriti ka hapniku redutseerumist plasmatöötlusega valmistatud Pt nanoosakestel, mis olid kantud redutseeritud grafeenoksiidile ja lämmastikuga dopeeritud redutseeritud grafeenile. Mõlemad katalüsaatorid näitasid märkimisväärset elektrokatalüütilist aktiivsust hapniku elektrokeemilisel redutseerumisel nii aluselises kui ka happelises lahuses.

Doktoritöö ühe osana uuriti termotöötluse mõju süsiniknanotorudele magnetrontolmustatud plaatina nanoosakeste elektrokeemilisele aktiivsusele 0,05 M H_2SO_4 ja 0,1 M KOH lahustes. Termotöötlus teostati N_2 voolus 30 minutit erinevatel temperatuuridel vahemikus 300 kuni 700 °C. Füsikokeemilised ja elektrokeemilised uuringud näitasid, et termotöötlus muudab pinnamorfoloogiat ja kõige optimaalsemaks töötlustemperatuuriks sobis 300 °C kuna sellel temperatuuril töödeldud katalüsaator näitas kõige suuremat elektrokatalüütilist aktiivsust.

Järgmises etapis uuriti TiO_2-ga modifitseeritud süsiniknanotorudele mangetrontolmustatud Pt nanoosakeste elektrokeemilisi omadusi väävelhappe ja kaaliumhüdroksiidi lahustes. Varieeriti nii Pt kui ka TiO_2 sisaldust katalüsaatoris. Elektrokeemilised testimised näitasid valmistatud komposiitkatalüsaatoril suuremat aktiivsust ja stabiilsust hapniku redutseerumisel kui kommertsiaalne

Pt/C, lisaks kinnitas Koutecky-Levichi analüüs, et hapniku redutseerumisreaktsioon kulgeb nelja elektroni ülekandmisel.

Doktoritöö viimases osas uuriti katalüsaatoreid, mis valmistati Pt fotokeemilise sadestamisega sool-geel meetodiga valmistatud SnO_2-C alusmaterjalile, saadud tulemusi võrreldi CO meetodil valmistatud Pt/C katalüsaatoriga. Kasutati kindlat SnO_2 kogust, et uurida katalüsaatorikandja mõju nii elektrokeemilisele aktiivsusele kui ka stabiilsusele 0,1 M $HClO_4$ lahuses. Selles töö osas selgus, et Pt/SnO_2-C katalüsaator omab kõrget aktiivsust ja stabiilsust just tugeva metalli-katalüsaatorikandja vastastikmõju tõttu.

10. ACKNOWLEDGEMENTS

I am thankful to my supervisors, Assoc. Prof. Kaido Tammeveski, Dr. Nadežda Kongi and Dr. Heiki Erikson for their proper guidance, support and encouragement.

I would like to thank my co-authors from the Institute of Physics at University of Tartu, Prof. Väino Sammelselg and Mr. Maido Merisalu for SEM measurements, and Dr. Mihkel Rähn for TEM measurements, Dr. Leonard Matisen and Dr. Mati Kook for XPS measurements, Mr. Aivar Tarre for ALD experiments, Mr. Peeter Ritslaid for magnetron sputtering experiments, Dr. Aleksei Treštšalov for plasma-assisted synthesis of the catalysts. I am also thankful to Dr. Jaan Aruväli from the Department of Geology, University of Tartu, for XRD analysis and Dr. Päärn Paiste, from the Department of Geology, University of Tartu, for the ICP-MS measurements.

I am very grateful to Prof. Nicolas Alonso-Vante from University of Poitiers, France for providing me the opportunity to work in his laboratory under his kind supervision and Dr. Luis Alberto Estudillo-Wong from Instituto Politecnico Nacional, Mexico for the XRD data analysis. I am also thankful to Prof. Gilberto Maia from Universidade Federal de Mato Grosso do Sul, Brazil for his valuable suggestions.

This work was financially supported by institutional research funding of the Estonian Ministry of Education and Research (IUT20-16), Estonian Research Council (Grant No. 9323), Graduate School of Functional materials and technologies receiving funding from the European Regional Development Fund, Centre of Excellence (TK141 “Advanced materials and high-technology devices for energy recuperation systems”) and Dora Plus Ph.D. student mobility (T1.2).

11. PUBLICATIONS

12. CURRICULUM VITAE

Name: Sajid Hussain
Born: March 1, 1985
Citizenship: Pakistani
Address: Ravila 14a, 50411 Tartu, Estonia
Phone: +372 5462 7429
E-mail: sajid.hussain@ut.ee, sajid_husin@yahoo.com

Haridus:

2015–	Tartu Ülikool, Loodus- ja täppisteaduste valdkond, doktoriõppe üliõpilane
2011–2014	Malakandi Ülikool, Chakdara, Pakistan, M.Phil. (füüsikaline keemia) 2014
2007–2010)	Urdu Riiklik Kunsti, Teaduse ja Tehnoloogia Ülikool, Karachi, Pakistan, M.Sc. (anorgaaniline keemia) 2010
2003–2007	Malakandi Ülikool, Chakdara, Pakistan, B.Sc. (loodusteadused) 2007

Major scientific publications:

1. M. Sadiq, Razia, S. Hussain, G. Zamin, Efficiency of Iron Supported on Porous Material (Prepared from Peanut Shell) for Liquid Phase Aerobic Oxidation of Alcohols, *Modern research in catalysis*, 3, (2014) 35–48.
2. S. Hussain, H. Erikson, N. Kongi, M. Merisalu, M. Rähn, V. Sammelselg, G. Maia, K. Tammeveski, Platinum particles electrochemically deposited on multi-walled carbon nanotubes for oxygen reduction reaction, *Journal of The Electrochemical Society,* 164 (2017) F1014-F1021.
3. S. Hussain, N. Kongi, L. Matisen, J. Kozlova, V. Sammelselg, K. Tammeveski, Platinum nanoparticles supported on nitrobenzene-functionalised graphene nanosheets as electrocatalysts for oxygen reduction reaction in alkaline media, *Electrochemistry Communications,* 81 (2017) 79–83.
4. S. Hussain, H. Erikson, N. Kongi, M. Merisalu, P. Ritslaid, V. Sammelselg, K. Tammeveski, Heat-treatment effects on the ORR activity of Pt nanoparticles deposited on multi-walled carbon nanotubes using magnetron sputtering technique, *International Journal of Hydrogen Energy,* 42 (9) (2017) 5958–5970.
5. S. Hussain, H. Erikson, N. Kongi, A. Treshchalov, M. Rähn, M. Kook, M. Merisalu, L. Matisen, V. Sammelselg, K. Tammeveski. Oxygen electroreduction on Pt nanoparticles deposited on reduced graphene oxide and N-doped reduced graphene oxide prepared by plasma-assisted synthesis in aqueous solution, *ChemElectroChem*, 5 (19) (2018) 2902–2911.
6. S. Hussain, H. Erikson, N. Kongi, A. Tarre, P. Ritslaid, M. Rähn, L. Matisen, M. Merisalu, V. Sammelselg, K. Tammeveski. Pt nanoparticles sputter-deposited on TiO_2/MWCNT composites prepared by atomic layer deposi-

tion: Improved electrocatalytic activity towards the oxygen reduction reaction and durability in acid media, *International Journal of Hydrogen Energy*, 43 (2018) 4967–4977.
7. S. Hussain, H. Erikson, N. Kongi, A. Tarre, P. Ritslaid, M. Rähn, M. Merisalu, V. Sammelselg, K. Tammeveski. Improved ORR activity and long-term durability of Pt nanoparticles sputter-deposited on TiO_2/MWCNT composite prepared by atomic layer deposition, (käsikiri esitatud).
8. S. Hussain, H. Erikson, N. Kongi, M. Rähn, L. Matisen, M. Merisalu, P. Paiste, J. Aruväli, V. Sammelselg, L.A. Estudillo-Wong, K. Tammeveski, N. Alonso-Vante, Platinum nanoparticles photo-deposited on SnO_2-C composites; an active and durable electrocatalyst for the oxygen reduction reaction, *Electrochimica Acta* 316 (2019) 162–172.
9. A. Sarapuu, S. Hussain, A. Kasikov, B. G. Pollet, K. Tammeveski, Electroreduction of oxygen on Nafion®-coated thin platinum films in acid media, (käsikiri esitatud).

13. ELULOOKIRJELDUS

Nimi: Sajid Hussain
Sünniaeg: 1. märts 1985
Kodakondsus: Pakistani
Aadress: Ravila 14a, 50411 Tartu, Estonia
Telefon: +372 5462 7429
E-post: sajid.hussain@ut.ee, sajid_husin@yahoo.com

Haridus:

2015–	Tartu Ülikool, Loodus- ja täppisteaduste valdkond, doktoriõppe üliõpilane
2011–2014	Malakandi Ülikool, Chakdara, Pakistan, M.Phil. (füüsikaline keemia) 2014
2007–2010)	Urdu Riiklik Kunsti, Teaduse ja Tehnoloogia Ülikool, Karachi, Pakistan, M.Sc. (anorgaaniline keemia) 2010
2003–2007	Malakandi Ülikool, Chakdara, Pakistan, B.Sc. (loodusteadused) 2007

Olulisemad publikatsioonid:

1. M. Sadiq, Razia, S. Hussain, G. Zamin, Efficiency of Iron Supported on Porous Material (Prepared from Peanut Shell) for Liquid Phase Aerobic Oxidation of Alcohols, *Modern research in catalysis*, 3, (2014) 35–48.
2. S. Hussain, H. Erikson, N. Kongi, M. Merisalu, M. Rähn, V. Sammelselg, G. Maia, K. Tammeveski, Platinum particles electrochemically deposited on multi-walled carbon nanotubes for oxygen reduction reaction, *Journal of The Electrochemical Society,* 164 (2017) F1014–F1021.
3. S. Hussain, N. Kongi, L. Matisen, J. Kozlova, V. Sammelselg, K. Tammeveski, Platinum nanoparticles supported on nitrobenzene-functionalised graphene nanosheets as electrocatalysts for oxygen reduction reaction in alkaline media, *Electrochemistry Communications,* 81 (2017) 79–83.
4. S. Hussain, H. Erikson, N. Kongi, M. Merisalu, P. Ritslaid, V. Sammelselg, K. Tammeveski, Heat-treatment effects on the ORR activity of Pt nanoparticles deposited on multi-walled carbon nanotubes using magnetron sputtering technique, *International Journal of Hydrogen Energy,* 42 (9) (2017) 5958–5970.
5. S. Hussain, H. Erikson, N. Kongi, A. Treshchalov, M. Rähn, M. Kook, M. Merisalu, L. Matisen, V. Sammelselg, K. Tammeveski. Oxygen electroreduction on Pt nanoparticles deposited on reduced graphene oxide and N-doped reduced graphene oxide prepared by plasma-assisted synthesis in aqueous solution, *ChemElectroChem*, 5 (19) (2018) 2902–2911.
6. S. Hussain, H. Erikson, N. Kongi, A. Tarre, P. Ritslaid, M. Rähn, L. Matisen, M. Merisalu, V. Sammelselg, K. Tammeveski. Pt nanoparticles sputter-deposited on TiO_2/MWCNT composites prepared by atomic layer deposi-

tion: Improved electrocatalytic activity towards the oxygen reduction reaction and durability in acid media, *International Journal of Hydrogen Energy*, 43 (2018) 4967–4977.
7. S. Hussain, H. Erikson, N. Kongi, A. Tarre, P. Ritslaid, M. Rähn, M. Merisalu, V. Sammelselg, K. Tammeveski. Improved ORR activity and long-term durability of Pt nanoparticles sputter-deposited on TiO_2/MWCNT composite prepared by atomic layer deposition, (käsikiri esitatud).
8. S. Hussain, H. Erikson, N. Kongi, M. Rähn, L. Matisen, M. Merisalu, P. Paiste, J. Aruväli, V. Sammelselg, L.A. Estudillo-Wong, K. Tammeveski, N. Alonso-Vante, Platinum nanoparticles photo-deposited on SnO_2-C composites; an active and durable electrocatalyst for the oxygen reduction reaction, *Electrochimica Acta* 316 (2019) 162–172.
9. A. Sarapuu, S. Hussain, A. Kasikov, B. G. Pollet, K. Tammeveski, Electroreduction of oxygen on Nafion®-coated thin platinum films in acid media, (käsikiri esitatud).

DISSERTATIONES CHIMICAE UNIVERSITATIS TARTUENSIS

1. **Toomas Tamm.** Quantum-chemical simulation of solvent effects. Tartu, 1993, 110 p.
2. **Peeter Burk.** Theoretical study of gas-phase acid-base equilibria. Tartu, 1994, 96 p.
3. **Victor Lobanov.** Quantitative structure-property relationships in large descriptor spaces. Tartu, 1995, 135 p.
4. **Vahur Mäemets.** The ^{17}O and ^{1}H nuclear magnetic resonance study of H_2O in individual solvents and its charged clusters in aqueous solutions of electrolytes. Tartu, 1997, 140 p.
5. **Andrus Metsala.** Microcanonical rate constant in nonequilibrium distribution of vibrational energy and in restricted intramolecular vibrational energy redistribution on the basis of slater's theory of unimolecular reactions. Tartu, 1997, 150 p.
6. **Uko Maran.** Quantum-mechanical study of potential energy surfaces in different environments. Tartu, 1997, 137 p.
7. **Alar Jänes.** Adsorption of organic compounds on antimony, bismuth and cadmium electrodes. Tartu, 1998, 219 p.
8. **Kaido Tammeveski.** Oxygen electroreduction on thin platinum films and the electrochemical detection of superoxide anion. Tartu, 1998, 139 p.
9. **Ivo Leito.** Studies of Brønsted acid-base equilibria in water and non-aqueous media. Tartu, 1998, 101 p.
10. **Jaan Leis.** Conformational dynamics and equilibria in amides. Tartu, 1998, 131 p.
11. **Toonika Rinken.** The modelling of amperometric biosensors based on oxidoreductases. Tartu, 2000, 108 p.
12. **Dmitri Panov.** Partially solvated Grignard reagents. Tartu, 2000, 64 p.
13. **Kaja Orupõld.** Treatment and analysis of phenolic wastewater with microorganisms. Tartu, 2000, 123 p.
14. **Jüri Ivask.** Ion Chromatographic determination of major anions and cations in polar ice core. Tartu, 2000, 85 p.
15. **Lauri Vares.** Stereoselective Synthesis of Tetrahydrofuran and Tetrahydropyran Derivatives by Use of Asymmetric Horner-Wadsworth-Emmons and Ring Closure Reactions. Tartu, 2000, 184 p.
16. **Martin Lepiku.** Kinetic aspects of dopamine D_2 receptor interactions with specific ligands. Tartu, 2000, 81 p.
17. **Katrin Sak.** Some aspects of ligand specificity of P2Y receptors. Tartu, 2000, 106 p.
18. **Vello Pällin.** The role of solvation in the formation of iotsitch complexes. Tartu, 2001, 95 p.
19. **Katrin Kollist.** Interactions between polycyclic aromatic compounds and humic substances. Tartu, 2001, 93 p.

20. **Ivar Koppel.** Quantum chemical study of acidity of strong and superstrong Brønsted acids. Tartu, 2001, 104 p.
21. **Viljar Pihl.** The study of the substituent and solvent effects on the acidity of OH and CH acids. Tartu, 2001, 132 p.
22. **Natalia Palm.** Specification of the minimum, sufficient and significant set of descriptors for general description of solvent effects. Tartu, 2001, 134 p.
23. **Sulev Sild.** QSPR/QSAR approaches for complex molecular systems. Tartu, 2001, 134 p.
24. **Ruslan Petrukhin.** Industrial applications of the quantitative structure-property relationships. Tartu, 2001, 162 p.
25. **Boris V. Rogovoy.** Synthesis of (benzotriazolyl)carboximidamides and their application in relations with *N*- and *S*-nucleophyles. Tartu, 2002, 84 p.
26. **Koit Herodes.** Solvent effects on UV-vis absorption spectra of some solvatochromic substances in binary solvent mixtures: the preferential solvation model. Tartu, 2002, 102 p.
27. **Anti Perkson.** Synthesis and characterisation of nanostructured carbon. Tartu, 2002, 152 p.
28. **Ivari Kaljurand.** Self-consistent acidity scales of neutral and cationic Brønsted acids in acetonitrile and tetrahydrofuran. Tartu, 2003, 108 p.
29. **Karmen Lust.** Adsorption of anions on bismuth single crystal electrodes. Tartu, 2003, 128 p.
30. **Mare Piirsalu.** Substituent, temperature and solvent effects on the alkaline hydrolysis of substituted phenyl and alkyl esters of benzoic acid. Tartu, 2003, 156 p.
31. **Meeri Sassian.** Reactions of partially solvated Grignard reagents. Tartu, 2003, 78 p.
32. **Tarmo Tamm.** Quantum chemical modelling of polypyrrole. Tartu, 2003. 100 p.
33. **Erik Teinemaa.** The environmental fate of the particulate matter and organic pollutants from an oil shale power plant. Tartu, 2003. 102 p.
34. **Jaana Tammiku-Taul.** Quantum chemical study of the properties of Grignard reagents. Tartu, 2003. 120 p.
35. **Andre Lomaka.** Biomedical applications of predictive computational chemistry. Tartu, 2003. 132 p.
36. **Kostyantyn Kirichenko.** Benzotriazole – Mediated Carbon–Carbon Bond Formation. Tartu, 2003. 132 p.
37. **Gunnar Nurk.** Adsorption kinetics of some organic compounds on bismuth single crystal electrodes. Tartu, 2003, 170 p.
38. **Mati Arulepp.** Electrochemical characteristics of porous carbon materials and electrical double layer capacitors. Tartu, 2003, 196 p.
39. **Dan Cornel Fara.** QSPR modeling of complexation and distribution of organic compounds. Tartu, 2004, 126 p.
40. **Riina Mahlapuu.** Signalling of galanin and amyloid precursor protein through adenylate cyclase. Tartu, 2004, 124 p.

41. **Mihkel Kerikmäe.** Some luminescent materials for dosimetric applications and physical research. Tartu, 2004, 143 p.
42. **Jaanus Kruusma.** Determination of some important trace metal ions in human blood. Tartu, 2004, 115 p.
43. **Urmas Johanson.** Investigations of the electrochemical properties of polypyrrole modified electrodes. Tartu, 2004, 91 p.
44. **Kaido Sillar.** Computational study of the acid sites in zeolite ZSM-5. Tartu, 2004, 80 p.
45. **Aldo Oras.** Kinetic aspects of dATPαS interaction with $P2Y_1$ receptor. Tartu, 2004, 75 p.
46. **Erik Mölder.** Measurement of the oxygen mass transfer through the air-water interface. Tartu, 2005, 73 p.
47. **Thomas Thomberg.** The kinetics of electroreduction of peroxodisulfate anion on cadmium (0001) single crystal electrode. Tartu, 2005, 95 p.
48. **Olavi Loog.** Aspects of condensations of carbonyl compounds and their imine analogues. Tartu, 2005, 83 p.
49. **Siim Salmar.** Effect of ultrasound on ester hydrolysis in aqueous ethanol. Tartu, 2006, 73 p.
50. **Ain Uustare.** Modulation of signal transduction of heptahelical receptors by other receptors and G proteins. Tartu, 2006, 121 p.
51. **Sergei Yurchenko.** Determination of some carcinogenic contaminants in food. Tartu, 2006, 143 p.
52. **Kaido Tämm.** QSPR modeling of some properties of organic compounds. Tartu, 2006, 67 p.
53. **Olga Tšubrik.** New methods in the synthesis of multisubstituted hydrazines. Tartu. 2006, 183 p.
54. **Lilli Sooväli.** Spectrophotometric measurements and their uncertainty in chemical analysis and dissociation constant measurements. Tartu, 2006, 125 p.
55. **Eve Koort.** Uncertainty estimation of potentiometrically measured ph and pK_a values. Tartu, 2006, 139 p.
56. **Sergei Kopanchuk.** Regulation of ligand binding to melanocortin receptor subtypes. Tartu, 2006, 119 p.
57. **Silvar Kallip.** Surface structure of some bismuth and antimony single crystal electrodes. Tartu, 2006, 107 p.
58. **Kristjan Saal.** Surface silanization and its application in biomolecule coupling. Tartu, 2006, 77 p.
59. **Tanel Tätte.** High viscosity $Sn(OBu)_4$ oligomeric concentrates and their applications in technology. Tartu, 2006, 91 p.
60. **Dimitar Atanasov Dobchev**. Robust QSAR methods for the prediction of properties from molecular structure. Tartu, 2006, 118 p.
61. **Hannes Hagu**. Impact of ultrasound on hydrophobic interactions in solutions. Tartu, 2007, 81 p.
62. **Rutha Jäger.** Electroreduction of peroxodisulfate anion on bismuth electrodes. Tartu, 2007, 142 p.

63. **Kaido Viht.** Immobilizable bisubstrate-analogue inhibitors of basophilic protein kinases: development and application in biosensors. Tartu, 2007, 88 p.
64. **Eva-Ingrid Rõõm.** Acid-base equilibria in nonpolar media. Tartu, 2007, 156 p.
65. **Sven Tamp.** DFT study of the cesium cation containing complexes relevant to the cesium cation binding by the humic acids. Tartu, 2007, 102 p.
66. **Jaak Nerut.** Electroreduction of hexacyanoferrate(III) anion on Cadmium (0001) single crystal electrode. Tartu, 2007, 180 p.
67. **Lauri Jalukse.** Measurement uncertainty estimation in amperometric dissolved oxygen concentration measurement. Tartu, 2007, 112 p.
68. **Aime Lust.** Charge state of dopants and ordered clusters formation in CaF_2:Mn and CaF_2:Eu luminophors. Tartu, 2007, 100 p.
69. **Iiris Kahn**. Quantitative Structure-Activity Relationships of environmentally relevant properties. Tartu, 2007, 98 p.
70. **Mari Reinik.** Nitrates, nitrites, N-nitrosamines and polycyclic aromatic hydrocarbons in food: analytical methods, occurrence and dietary intake. Tartu, 2007, 172 p.
71. **Heili Kasuk.** Thermodynamic parameters and adsorption kinetics of organic compounds forming the compact adsorption layer at Bi single crystal electrodes. Tartu, 2007, 212 p.
72. **Erki Enkvist.** Synthesis of adenosine-peptide conjugates for biological applications. Tartu, 2007, 114 p.
73. **Svetoslav Hristov Slavov**. Biomedical applications of the QSAR approach. Tartu, 2007, 146 p.
74. **Eneli Härk.** Electroreduction of complex cations on electrochemically polished Bi(*hkl*) single crystal electrodes. Tartu, 2008, 158 p.
75. **Priit Möller.** Electrochemical characteristics of some cathodes for medium temperature solid oxide fuel cells, synthesized by solid state reaction technique. Tartu, 2008, 90 p.
76. **Signe Viggor.** Impact of biochemical parameters of genetically different pseudomonads at the degradation of phenolic compounds. Tartu, 2008, 122 p.
77. **Ave Sarapuu.** Electrochemical reduction of oxygen on quinone-modified carbon electrodes and on thin films of platinum and gold. Tartu, 2008, 134 p.
78. **Agnes Kütt.** Studies of acid-base equilibria in non-aqueous media. Tartu, 2008, 198 p.
79. **Rouvim Kadis.** Evaluation of measurement uncertainty in analytical chemistry: related concepts and some points of misinterpretation. Tartu, 2008, 118 p.
80. **Valter Reedo.** Elaboration of IVB group metal oxide structures and their possible applications. Tartu, 2008, 98 p.
81. **Aleksei Kuznetsov.** Allosteric effects in reactions catalyzed by the cAMP-dependent protein kinase catalytic subunit. Tartu, 2009, 133 p.

82. **Aleksei Bredihhin.** Use of mono- and polyanions in the synthesis of multisubstituted hydrazine derivatives. Tartu, 2009, 105 p.
83. **Anu Ploom.** Quantitative structure-reactivity analysis in organosilicon chemistry. Tartu, 2009, 99 p.
84. **Argo Vonk.** Determination of adenosine A_{2A}- and dopamine D_1 receptor-specific modulation of adenylate cyclase activity in rat striatum. Tartu, 2009, 129 p.
85. **Indrek Kivi.** Synthesis and electrochemical characterization of porous cathode materials for intermediate temperature solid oxide fuel cells. Tartu, 2009, 177 p.
86. **Jaanus Eskusson.** Synthesis and characterisation of diamond-like carbon thin films prepared by pulsed laser deposition method. Tartu, 2009, 117 p.
87. **Marko Lätt.** Carbide derived microporous carbon and electrical double layer capacitors. Tartu, 2009, 107 p.
88. **Vladimir Stepanov.** Slow conformational changes in dopamine transporter interaction with its ligands. Tartu, 2009, 103 p.
89. **Aleksander Trummal.** Computational Study of Structural and Solvent Effects on Acidities of Some Brønsted Acids. Tartu, 2009, 103 p.
90. **Eerold Vellemäe.** Applications of mischmetal in organic synthesis. Tartu, 2009, 93 p.
91. **Sven Parkel.** Ligand binding to 5-HT_{1A} receptors and its regulation by Mg^{2+} and Mn^{2+}. Tartu, 2010, 99 p.
92. **Signe Vahur.** Expanding the possibilities of ATR-FT-IR spectroscopy in determination of inorganic pigments. Tartu, 2010, 184 p.
93. **Tavo Romann**. Preparation and surface modification of bismuth thin film, porous, and microelectrodes. Tartu, 2010, 155 p.
94. **Nadežda Aleksejeva.** Electrocatalytic reduction of oxygen on carbon nanotube-based nanocomposite materials. Tartu, 2010, 147 p.
95. **Marko Kullapere.** Electrochemical properties of glassy carbon, nickel and gold electrodes modified with aryl groups. Tartu, 2010, 233 p.
96. **Liis Siinor.** Adsorption kinetics of ions at Bi single crystal planes from aqueous electrolyte solutions and room-temperature ionic liquids. Tartu, 2010, 101 p.
97. **Angela Vaasa.** Development of fluorescence-based kinetic and binding assays for characterization of protein kinases and their inhibitors. Tartu 2010, 101 p.
98. **Indrek Tulp.** Multivariate analysis of chemical and biological properties. Tartu 2010, 105 p.
99. **Aare Selberg.** Evaluation of environmental quality in Northern Estonia by the analysis of leachate. Tartu 2010, 117 p.
100. **Darja Lavõgina.** Development of protein kinase inhibitors based on adenosine analogue-oligoarginine conjugates. Tartu 2010, 248 p.
101. **Laura Herm.** Biochemistry of dopamine D_2 receptors and its association with motivated behaviour. Tartu 2010, 156 p.

102. **Terje Raudsepp.** Influence of dopant anions on the electrochemical properties of polypyrrole films. Tartu 2010, 112 p.
103. **Margus Marandi.** Electroformation of Polypyrrole Films: *In-situ* AFM and STM Study. Tartu 2011, 116 p.
104. **Kairi Kivirand.** Diamine oxidase-based biosensors: construction and working principles. Tartu, 2011, 140 p.
105. **Anneli Kruve.** Matrix effects in liquid-chromatography electrospray mass-spectrometry. Tartu, 2011, 156 p.
106. **Gary Urb.** Assessment of environmental impact of oil shale fly ash from PF and CFB combustion. Tartu, 2011, 108 p.
107. **Nikita Oskolkov.** A novel strategy for peptide-mediated cellular delivery and induction of endosomal escape. Tartu, 2011, 106 p.
108. **Dana Martin.** The QSPR/QSAR approach for the prediction of properties of fullerene derivatives. Tartu, 2011, 98 p.
109. **Säde Viirlaid.** Novel glutathione analogues and their antioxidant activity. Tartu, 2011, 106 p.
110. **Ülis Sõukand.** Simultaneous adsorption of Cd^{2+}, Ni^{2+}, and Pb^{2+} on peat. Tartu, 2011, 124 p.
111. **Lauri Lipping.** The acidity of strong and superstrong Brønsted acids, an outreach for the "limits of growth": a quantum chemical study. Tartu, 2011, 124 p.
112. **Heisi Kurig.** Electrical double-layer capacitors based on ionic liquids as electrolytes. Tartu, 2011, 146 p.
113. **Marje Kasari.** Bisubstrate luminescent probes, optical sensors and affinity adsorbents for measurement of active protein kinases in biological samples. Tartu, 2012, 126 p.
114. **Kalev Takkis.** Virtual screening of chemical databases for bioactive molecules. Tartu, 2012, 122 p.
115. **Ksenija Kisseljova**. Synthesis of aza-β^3-amino acid containing peptides and kinetic study of their phosphorylation by protein kinase A. Tartu, 2012, 104 p.
116. **Riin Rebane.** Advanced method development strategy for derivatization LC/ESI/MS. Tartu, 2012, 184 p.
117. **Vladislav Ivaništšev.** Double layer structure and adsorption kinetics of ions at metal electrodes in room temperature ionic liquids. Tartu, 2012, 128 p.
118. **Irja Helm.** High accuracy gravimetric Winkler method for determination of dissolved oxygen. Tartu, 2012, 139 p.
119. **Karin Kipper.** Fluoroalcohols as Components of LC-ESI-MS Eluents: Usage and Applications. Tartu, 2012, 164 p.
120. **Arno Ratas.** Energy storage and transfer in dosimetric luminescent materials. Tartu, 2012, 163 p.
121. **Reet Reinart-Okugbeni**. Assay systems for characterisation of subtype-selective binding and functional activity of ligands on dopamine receptors. Tartu, 2012, 159 p.

122. **Lauri Sikk.** Computational study of the Sonogashira cross-coupling reaction. Tartu, 2012, 81 p.
123. **Karita Raudkivi.** Neurochemical studies on inter-individual differences in affect-related behaviour of the laboratory rat. Tartu, 2012, 161 p.
124. **Indrek Saar.** Design of GalR2 subtype specific ligands: their role in depression-like behavior and feeding regulation. Tartu, 2013, 126 p.
125. **Ann Laheäär.** Electrochemical characterization of alkali metal salt based non-aqueous electrolytes for supercapacitors. Tartu, 2013, 127 p.
126. **Kerli Tõnurist.** Influence of electrospun separator materials properties on electrochemical performance of electrical double-layer capacitors. Tartu, 2013, 147 p.
127. **Kaija Põhako-Esko.** Novel organic and inorganic ionogels: preparation and characterization. Tartu, 2013, 124 p.
128. **Ivar Kruusenberg.** Electroreduction of oxygen on carbon nanomaterial-based catalysts. Tartu, 2013, 191 p.
129. **Sander Piiskop.** Kinetic effects of ultrasound in aqueous acetonitrile solutions. Tartu, 2013, 95 p.
130. **Ilona Faustova**. Regulatory role of L-type pyruvate kinase N-terminal domain. Tartu, 2013, 109 p.
131. **Kadi Tamm.** Synthesis and characterization of the micro-mesoporous anode materials and testing of the medium temperature solid oxide fuel cell single cells. Tartu, 2013, 138 p.
132. **Iva Bozhidarova Stoyanova-Slavova.** Validation of QSAR/QSPR for regulatory purposes. Tartu, 2013, 109 p.
133. **Vitali Grozovski**. Adsorption of organic molecules at single crystal electrodes studied by *in situ* STM method. Tartu, 2014, 146 p.
134. **Santa Veikšina**. Development of assay systems for characterisation of ligand binding properties to melanocortin 4 receptors. Tartu, 2014, 151 p.
135. **Jüri Liiv.** PVDF (polyvinylidene difluoride) as material for active element of twisting-ball displays. Tartu, 2014, 111 p.
136. **Kersti Vaarmets.** Electrochemical and physical characterization of pristine and activated molybdenum carbide-derived carbon electrodes for the oxygen electroreduction reaction. Tartu, 2014, 131 p.
137. **Lauri Tõntson**. Regulation of G-protein subtypes by receptors, guanine nucleotides and Mn^{2+}. Tartu, 2014, 105 p.
138. **Aiko Adamson.** Properties of amine-boranes and phosphorus analogues in the gas phase. Tartu, 2014, 78 p.
139. **Elo Kibena**. Electrochemical grafting of glassy carbon, gold, highly oriented pyrolytic graphite and chemical vapour deposition-grown graphene electrodes by diazonium reduction method. Tartu, 2014, 184 p.
140. **Teemu Näykki.** Novel Tools for Water Quality Monitoring – From Field to Laboratory. Tartu, 2014, 202 p.
141. **Karl Kaupmees.** Acidity and basicity in non-aqueous media: importance of solvent properties and purity. Tartu, 2014, 128 p.

142. **Oleg Lebedev**. Hydrazine polyanions: different strategies in the synthesis of heterocycles. Tartu, 2015, 118 p.
143. **Geven Piir.** Environmental risk assessment of chemicals using QSAR methods. Tartu, 2015, 123 p.
144. **Olga Mazina.** Development and application of the biosensor assay for measurements of cyclic adenosine monophosphate in studies of G protein-coupled receptor signalinga. Tartu, 2015, 116 p.
145. **Sandip Ashokrao Kadam.** Anion receptors: synthesis and accurate binding measurements. Tartu, 2015, 116 p.
146. **Indrek Tallo.** Synthesis and characterization of new micro-mesoporous carbide derived carbon materials for high energy and power density electrical double layer capacitors. Tartu, 2015, 148 p.
147. **Heiki Erikson.** Electrochemical reduction of oxygen on nanostructured palladium and gold catalysts. Tartu, 2015, 204 p.
148. **Erik Anderson.** *In situ* Scanning Tunnelling Microscopy studies of the interfacial structure between Bi(111) electrode and a room temperature ionic liquid. Tartu, 2015, 118 p.
149. **Girinath G. Pillai.** Computational Modelling of Diverse Chemical, Biochemical and Biomedical Properties. Tartu, 2015, 140 p.
150. **Piret Pikma.** Interfacial structure and adsorption of organic compounds at Cd(0001) and Sb(111) electrodes from ionic liquid and aqueous electrolytes: an *in situ* STM study. Tartu, 2015, 126 p.
151. **Ganesh babu Manoharan.** Combining chemical and genetic approaches for photoluminescence assays of protein kinases. Tartu, 2016, 126 p.
152. **Carolin Siimenson**. Electrochemical characterization of halide ion adsorption from liquid mixtures at Bi(111) and pyrolytic graphite electrode surface. Tartu, 2016, 110 p.
153. **Asko Laaniste.** Comparison and optimisation of novel mass spectrometry ionisation sources. Tartu, 2016, 156 p.
154. **Hanno Evard.** Estimating limit of detection for mass spectrometric analysis methods. Tartu, 2016, 224 p.
155. **Kadri Ligi.** Characterization and application of protein kinase-responsive organic probes with triplet-singlet energy transfer. Tartu, 2016, 122 p.
156. **Margarita Kagan.** Biosensing penicillins' residues in milk flows. Tartu, 2016, 130 p.
157. **Marie Kriisa.** Development of protein kinase-responsive photoluminescent probes and cellular regulators of protein phosphorylation. Tartu, 2016, 106 p.
158. **Mihkel Vestli.** Ultrasonic spray pyrolysis deposited electrolyte layers for intermediate temperature solid oxide fuel cells. Tartu, 2016, 156 p.
159. **Silver Sepp**. Influence of porosity of the carbide-derived carbon on the properties of the composite electrocatalysts and characteristics of polymer electrolyte fuel cells. Tartu, 2016, 137 p.
160. **Kristjan Haav**. Quantitative relative equilibrium constant measurements in supramolecular chemistry. Tartu, 2017, 158 p.

161. **Anu Teearu**. Development of MALDI-FT-ICR-MS methodology for the analysis of resinous materials. Tartu, 2017, 205 p.
162. **Taavi Ivan**. Bifunctional inhibitors and photoluminescent probes for studies on protein complexes. Tartu, 2017, 140 p.
163. **Maarja-Liisa Oldekop**. Characterization of amino acid derivatization reagents for LC-MS analysis. Tartu, 2017, 147 p.
164. **Kristel Jukk**. Electrochemical reduction of oxygen on platinum- and palladium-based nanocatalysts. Tartu, 2017, 250 p.
165. **Siim Kukk**. Kinetic aspects of interaction between dopamine transporter and *N*-substituted nortropane derivatives. Tartu, 2017, 107 p.
166. **Birgit Viira**. Design and modelling in early drug development in targeting HIV-1 reverse transcriptase and Malaria. Tartu, 2017, 172 p.
167. **Rait Kivi**. Allostery in cAMP dependent protein kinase catalytic subunit. Tartu, 2017, 115 p.
168. **Agnes Heering**. Experimental realization and applications of the unified acidity scale. Tartu, 2017, 123 p.
169. **Delia Juronen**. Biosensing system for the rapid multiplex detection of mastitis-causing pathogens in milk. Tartu, 2018, 85 p.
170. **Hedi Rahnel.** ARC-inhibitors: from reliable biochemical assays to regulators of physiology of cells. Tartu, 2018, 176 p.
171. **Anton Ruzanov.** Computational investigation of the electrical double layer at metal–aqueous solution and metal–ionic liquid interfaces. Tartu, 2018, 129 p.
172. **Katrin Kestav.** Crystal Structure-Guided Development of Bisubstrate-Analogue Inhibitors of Mitotic Protein Kinase Haspin. Tartu, 2018, 166 p.
173. **Mihkel Ilisson.** Synthesis of novel heterocyclic hydrazine derivatives and their conjugates. Tartu, 2018, 101 p.
174. **Anni Allikalt.** Development of assay systems for studying ligand binding to dopamine receptors. Tartu, 2018, 160 p.
175. **Ove Oll.** Electrical double layer structure and energy storage characteristics of ionic liquid based capacitors. Tartu, 2018, 187 p.
176. **Rasmus Palm.** Carbon materials for energy storage applications. Tartu, 2018, 114 p.
177. **Jörgen Metsik.** Preparation and stability of poly(3,4-ethylenedioxythiophene) thin films for transparent electrode applications. Tartu, 2018, 111 p.
178. **Sofja Tšepelevitš.** Experimental studies and modeling of solute-solvent interactions. Tartu, 2018, 109 p.
179. **Märt Lõkov.** Basicity of some nitrogen, phosphorus and carbon bases in acetonitrile. Tartu, 2018, 104 p.
180. **Anton Mastitski**. Preparation of α-aza-amino acid precursors and related compounds by novel methods of reductive one-pot alkylation and direct alkylation. Tartu, 2018, 155 p.
181. **Jürgen Vahter**. Development of bisubstrate inhibitors for protein kinase CK2. Tartu, 2019, 186 p.

182. **Piia Liigand.** Expanding and improving methodology and applications of ionization efficiency measurements. Tartu, 2019, 189 p.
183. **Sigrid Selberg.** Synthesis and properties of lipophilic phosphazene-based indicator molecules. Tartu, 2019, 74 p.
184. **Jaanus Liigand.** Standard substance free quantification for LC/ESI/MS analysis based on the predicted ionization efficiencies. Tartu, 2019, 254 p.
185. **Marek Mooste.** Surface and electrochemical characterisation of aryl film and nanocomposite material modified carbon and metal-based electrodes. Tartu, 2019, 304 p.
186. **Mare Oja.** Experimental investigation and modelling of pH profiles for effective membrane permeability of drug substances. Tartu, 2019, 306 p.